ABSTRACT

Title of Dissertation:	DEEP CONVECTIVE TRANSPORT AND WET SCAVENGING IN DIFFERENT CONVECTIVE REGIMES DURING THE DC3 FIELD CAMPAIGN
	Yunyao Li, Doctor of Philosophy, 2018
Dissertation directed by:	Research Professor Kenneth E. Pickering Department of Atmospheric and Oceanic Science

Deep convective transport of surface moisture and pollution from the planetary boundary layer to the upper troposphere and lower stratosphere affects the radiation budget and climate. Firstly, I analyzed the deep convective transport through cloud-resolved simulations of three different convective regimes from the 2012 Deep Convective Clouds and Chemistry (DC3) field campaign: an airmass thunderstorm, a supercell storm, and a mesoscale convective system (MCS). Analysis of vertical flux divergence shows that deep convective transport in the supercell case is the strongest per unit area, while transport of boundary layer insoluble trace gases is relatively weak in the MCS due to the injection of clean air into the mid-troposphere by a strong rear

inflow jet. Additionally, forward and backward trajectories are used to determine the source of the upper-level detrained air.

My second focus is using of cloud parameterized Weather Research and Forecasting model coupled with chemistry (WRF-Chem) simulations to analyze the subgrid deep convective transport in the supercell case and MCS case. Based on the precipitation results, the best WRF simulation of these storms was obtained with use of the Grell-Freitas (GF) convective scheme. The default subgrid convective transport scheme was replaced with a scheme to compute convective transport within the GF subgrid cumulus parameterization, which resulted in improved transport simulations. The results demonstrate the importance of having subgrid convective transport consistent with the convective parameterization in regional models. Moreover, the subgrid scale convective transport played a more significant role in the supercell case than the MCS case.

I evaluated the model-simulated subgrid wet scavenging of soluble trace gases (such as HNO_3, CH_2O, CH_3OOH, H_2O_2, and SO_2) in the supercell case, and improved subgrid wet scavenging by determining appropriate ice retention factors, and by adjusting the conversion rate of cloud water to rain water. The introduction of the ice retention factors greatly improved the model simulation of less soluble species (e.g. decreased the CH_2O simulation error by 12 % and decreased the CH_3OOH simulation error by 63%). Finally, I conducted a > 24-hour long simulation to examine downwind ozone production and its sensitivity to the ice retention factors.

DEEP CONVECTIVE TRANSPORT AND WET SCAVENGING IN DIFFERENT CONVECTIVE REGIMES DURING THE DC3 FIELD CAMPAIGN

by

Yunyao Li

Dissertation submitted to the Faculty of the Graduate School of the
University of Maryland, College Park, in partial fulfillment
of the requirements for the degree of
Doctor of Philosophy
2018

Advisory Committee:
Research Professor Kenneth Pickering, Chair/Advisor
Professor Russell Dickerson
Professor Da-Lin Zhang
Associate Research Scientist Dale Allen
Associate Professor Sujay Kaushal, Dean's Representative

Dedication

To my mother, father, paternal grandparents, and maternal grandparents.

Acknowledgements

First of all, I would like to give thanks to my advisor, Dr. Kenneth Pickering. During these six years, through countless individual and group meetings as well as email communications, he provided specific guidance and valuable advice toward my research, experiments, writings, and presentations. Also, I would like to express my thanks to the other collaborators on the work in this Dissertation: Dr. Dale Allen, Dr. Kristin Cummings, Dr. Megan Bela, Dr. Mary Barth, Dr. Alex Fierro, Dr. Gretchen Mullendore, Dr. Georg Grell, Dr. Cameron Homeyer, Dr. Retha Mecikalski, and Dr. Lawrence Carey. Special thanks go to Dr. Dale Allen who helped me revise drafts of my various papers.

For my research project, I was funded by the NSF grant AGS-1522551. Without this financial support, I would not have been able to devote myself fully on the project. Furthermore, I would like to acknowledge high-performance computing support from Yellowstone (ark:/85065/d7wd3xhc) and Cheyenne (doi:10.5065/D6RX99HX) provided by NCAR's Computational and Information Systems Laboratory, sponsored by the National Science Foundation. Without the high-performance computing support, I might have taken10 more years to achieve this degree.

Moreover, I would like to express my appreciation to those who taught me in AOSC classes: Dr. Da-Lin Zhang (AOSC 610), Dr. Russell Dickerson (AOSC 620), Dr. Antonio Busalacchi (AOSC 680), Dr. James Carton (AOSC 611), Dr. Xin-Zhong Liang (AOSC 621), Dr. Sumant Nigam (AOSC 617), Dr. Vernon Kousky (AOSC 600),

Dr. Eugenia Kalnay (AOSC 614 & 630), Dr. Ross Salawitch (AOSC 633), and Dr. Scott Rudlosky (AOSC 602). Thank you for helping me build a solid academic background, which is very important to my research career.

Finally, I would like to thank my husband, Shunjie Tu, for his complete support and sacrifice for my research, especially for the last two months when I was busy with my dissertation. He cooked for me, took care of the kid, and did all the housework, without any complaint or expecting anything in return.

Table of Contents

List of Tables

List of Figures

List of Abbreviations

3D	three-dimensional
ABLE	Amazon Boundary Layer Experiment
ARMOR	Advanced Radar for Meteorological and Operational Research
ARW	Advanced Research WRF
AS	Arakawa and Schubert closure in Grell-Freitas cumulus scheme
BC	boundary conditions
BMJ	Betts-Miller-Janjic
CAPE	convective available potential energy
CBMF	cloud base mass flux
CH_2O	formaldehyde
CH_3OOH	methyl hydroperoxide
CI	convection initiation
CMAQ	The Community Multiscale Air Quality Modeling System
CO	carbon monoxide
CRM	cloud-resolving model
DC3	Deep Convective Clouds and Chemistry field campaign
ENTLN	Earth Networks Total Lightning Network
FINN	Fire Inventory of NCAR
F-TUV	Fast-Tropospheric Ultraviolet-Visible photolysis scheme
G3D	Grell-3D cumulus parameterization
GCE	Goddard Cumulus Ensemble
GD	Grell-Devenyi cumulus parameterization
GEOS	Goddard Earth Observing System model
GF	Grell-Freitas cumulus parameterization
GFS	Global Forecast System
GPS	Global Positioning System
GV	Gulfstream-V
H_2O_2	hydrogen peroxide
HNO_3	nitric acid
HO	hydroxyl radical
HO_2	hydroperoxy radical
HO_x	hydrogen oxides
hPa	hectoPascals
IC	initial conditions
IF	inflow
IPCC	Intergovernmental Panel on Climate Change
KF	Kain-Fritsch cumulus parameterization

KLZK	Little Rock 88-D radar site
KSGF	Springfield, MO 88-D radar site
LCL	lifting condensation level
LDA	Lightning data assimilation
LIS	Lightning Imaging Sensor
LMA	Lightning Mapping Array
LMD	level of maximum detrainment
LNO_x	lightning nitrogen oxides
LS	lower stratosphere
MC	moisture convergence
MCC	mesoscale convective complex
MCS	mesoscale convective system
MEGAN	Model of Emissions of Gases and Aerosols from Nature
MOZART-4	Model for Ozone and Related chemical Tracers, version 4
MOZCART	Model for Ozone and Related chemical Tracers gas phase chemistry and Goddard Chemistry Aerosol Radiation and Transport aerosols
MYJ	Mellor-Yamada-Janjic
NALMA	North Alabama Lightning Mapping Array
NAM-ANL	North American Mesoscale Analysis
NASA	National Aeronautics and Space Administration
NCAR	National Center for Atmospheric Research
NCEP	National Centers for Environmental Prediction
NEI	National Emissions Inventory
NEXRAD	Next Generation Weather Radar
NO	nitric oxide
NO_2	nitrogen dioxide
NO_x	nitrogen oxides
NOXP	National Oceanic and Atmospheric Administration Xband dual-POLarized mobile radars
NSF	National Science Foundation
NSSL	National Severe Storms Laboratory
NWS	National Weather Service
O_3	ozone
OF	outflow
OH	hydroxyl radical
OKLMA	Oklahoma Lightning Mapping Array
OTD	optical transient detector
PAN	peroxyacetyl nitrate
PBL	planetary boundary layer

PEM	Pacific Exploratory Mission
PRESTORM	Preliminary Regional Experiment for Stormscale Operational Meteorology Program-Central Phase
QISC	quasi-isolated strong convection
QNSE	Quasi-Normal Scale Elimination PBL scheme
RAOB	radiosonde observations
RHS	Right hand side
RO_2	organic peroxy radicals
RRTMG	Rapid Radiative Transfer Model for General Circulation Models
SC	subgrid contribution
SCM	single column model
SE	scavenging efficiencies
SMART	Shared Mobile Atmospheric Research and Teaching
SO_2	sulfur dioxide
SPCZ	South Pacific Convergence Zone
STERAO	Stratospheric-Tropospheric Experiment: Radiation, Aerosols, and Ozone
TRACE-A	Transport and Atmospheric Chemistry Near the Equator-Atlantic
UAH	University of Alabama in Huntsville
UT	upper troposphere
UTC	Coordinated Universal Time
UTLS	upper troposphere and lower stratosphere
VAPOR	Visualization and Analysis Platform for Ocean, Atmosphere, and Solar Researchers
VFD	vertical flux divergence
VHF	very high frequency
WRF	Weather Research and Forecasting model
WRF-Chem	Weather Research and Forecasting model coupled with Chemistry
WSM6	WRF Single-Moment 6-class scheme
WSR-88D	Weather Surveillance Radar-1988 Doppler
YSU	Yonsei University PBL scheme

Chapter 1 : Introduction

1.1 Deep Convective Transport

Deep convection is an important mechanism for the transport of planetary boundary layer (PBL) air into the upper troposphere (UT) and lower stratosphere (LS, UTLS) (Chatfield and Crutzen, 1984; Dickerson et al., 1987). It only takes a few minutes to about an hour to transport an air parcel from the surface to the UT (Skamarock et al., 2000). Measurements from field campaigns (Dickerson et al., 1987; Pickering et al., 1988; 1996; 2001; Scala et al., 1990; Thompson et al., 1994; Stenchikov et al., 1996; Wang et al., 1996; Jung et al., 2005; Bertram et al., 2007; Homeyer et al., 2014; Apel et al., 2015) and satellites (Setvak and Doswell III, 1990; Levizzani and Setvak, 1996; Halland et al., 2009; Jensen et al., 2015; Livesey et al., 2013) have demonstrated that deep convective transport affects the moisture and the chemical composition of the UTLS.

Deep convective transport of moist and polluted PBL air into the UTLS has a significant impact on climate. The transport of local air pollutants from PBL to the free troposphere may transform local air pollution into regional or global atmospheric chemistry issues (Kong & Qin, 1993, 1994a; Lyons et al., 1986). The vertical transport of ozone (O_3) precursor gases substantially increases the production rate of O_3 in cloud outflow (Pickering et al., 1990; 1992a, 1992b) that occurs in the upper troposphere where winds are stronger and O_3 has a longer lifetime and, thus, an expanded range of influence than in the PBL. As reported in Intergovernmental Panel on Climate Change

(IPCC, 2013), tropospheric O_3 is the third most important greenhouse gas in terms of radiative forcing of climate. Additionally, the injection of PBL moisture into the stratosphere enhances the concentration of water vapor in the LS (Homeyer et al., 2014), which is one of the leading causes for LS water vapor variability. According to Solomon et al. (2010), stratospheric water vapor is a key driver for decadal global surface climate change. In addition, recent studies (Mishra and Shibata, 2012; Park and Allen, 2015) argue that deep convective transport affects the aerosol vertical distribution, an important component of aerosol radiative forcing.

The mechanism of deep convective transport is complex. The amount of PBL trace gases transported to the UTLS through deep convection depends on various meteorological and chemical factors. During the Preliminary Regional Experiment for Stormscale Operational Meteorology Program-Central Phase (PRESTORM) project, increased carbon monoxide (CO) concentrations in the UT due to convective transport from the PBL were documented in the 13 June and 15 June storms (Dickerson et al., 1987; Pickering et al., 1989). Conversely, in the 17 June case, the CO mixing ratio in the UT outflow was similar to levels found in background air. This was hypothesized to possibly arise from the passage of a cold front, which prevented direct entry of PBL air into the cloud causing cloud inflow to be dominated by air from above the PBL (Pickering et al., 1988). Hence, large-scale conditions play an important role in deep convective transport.

Besides large scale factors, PBL conditions and storm dynamics also affect deep convective transport. A model simulation of deep convective transport in a mesoscale convective complex (MCC) observed during the North Dakota Thunderstorm Project in 1989 showed that a moister PBL produced stronger transport of CO from the PBL to the anvil region (Stenchikov et al., 1996). Several additional case studies have shown that deep convective transport is closely related to storm vertical velocity as well as storm propagation speed (Pickering et al., 1992a; Wang et al., 1996). Kong and Qin (1994b) demonstrated that storm types played an important role in the transport. A recent study by Bigelbach et al. (2014) simulated the mass transport during the 2007 convective season in the U.S. Southern Great Plains. The results demonstrated that quasi-isolated strong convection (QISC) exhibited stronger and deeper flux than mesoscale convective systems (MCSs), which indicated that the deep convective transport varied with different types of convective regimes.

The inflow structure also influences deep convective transport. Scala et al. (1990) used a two-dimensional moist cloud model to determine the transport pathways within a wet season continental tropical squall line observed during the National Aeronautics and Space Administration (NASA) Amazon Boundary Layer Experiment (ABLE) 2B field campaign. Parcel trajectory analysis illustrated that more than 50% of the air transported to the anvil region originated in the mid-troposphere (at or above 6 km) rather than the PBL. More than 50% of PBL air entering the core updrafts terminated below 5 km and became involved in a rotor circulation at 4.5 km. Only about 15% of the PBL air was transported directly to the cloud top near 12 km. On the

other hand, during the Amazon dry season, convective events over Brazilian biomass burning regions show substantial vertical transport of O_3 precursors to the UT leading to large enhancements of O_3 production in the upper troposphere (Pickering et al., 1991, 1992a, 1992b, 1992c; 1996). The substantial difference in the vertical structure of the equivalent potential temperature profile between the wet and dry seasons leads to the difference in convective transport characteristics. Mid-latitude studies have shown that most of the mass transport into the UTLS originated in the PBL (Skamarock et al., 2000; Mullendore et al., 2005) in the storm cases considered.

Model simulations at both cloud parameterized and cloud resolved resolutions are often used in deep convective transport studies. A reliable simulation of deep convective transport of trace gases remains challenging as it requires the model to faithfully reproduce large-scale conditions, PBL structure, storm evolution status, inflow structure, as well as the surrounding chemical composition. The Weather Research and Forecasting (WRF) model is a three-dimensional (3D) compressible nonhydrostatic atmospheric modeling system designed for both meteorological research and numerical weather prediction. WRF-Chem (Grell et al., 2005) is WRF coupled with atmospheric chemistry and simulates the emission, transport, mixing, and chemical transformation of trace gases and aerosols simultaneously with the meteorology. Barth et al. (2012) utilized the Weather Research and Forecasting model coupled with Chemistry (WRF-Chem) (Fast et al., 2006; Grell et al., 2005; Peckham et al., 2011) to study the convective transport and chemistry associated with the early stages of the North American Monsoon, which was the first time WRF-Chem was

applied at high resolution (4 km) over the entire continental United States. After that several studies also applied WRF and WRF-Chem to simulate convective transport from the PBL to the anvil region for particular events (e.g. Siu et al., 2015; Bela et al., 2016a; Li et al., 2017).

Subgrid scale convective transport of trace gases is an important component of cloud parameterized simulations. Wang et al. (1996) evaluated the subgrid scale and grid scale convective transport in a tropical MCS during the Transport and Atmospheric Chemistry Near the Equator-Atlantic (TRACE-A) experiment and a mid-latitude squall line during the PRESTORM at 90 and 30 km model resolution (two nested domains) for the MCS and 75 and 25 km for the squall line case. They found that substantial subgrid transport occurred in the updraft (~ 41% of total upward transport in the MCS case and ~ 64% in the squall line case). Ott et al. (2009) compared vertical profiles of trace gases from simulations of storms during three field campaigns with a cloud-resolving model (CRM) and a single column model (SCM) implementation of version 5 of the Goddard Earth Observing System (GEOS) that utilized the relaxed Arakawa-Schubert cumulus parameterization. They found that the SCM simulations underpredicted convective mass flux and trace gas mixing ratios in the upper troposphere relative to the CRM simulations. Also, they investigated the sensitivity of convective transport in the SCM to the values of parameters contained in the moist physics schemes. By tuning the most significant parameters influencing convective transport, the SCM simulation of trace gas mixing ratio was improved. Freitas et al. (2000) presented a parameterization of subgrid scale convective transport of trace gases

associated with deep moist convective systems for low-resolution atmospheric models. Grell and Freitas (2014) described a subgrid convective parameterization, tracer transport, and wet scavenging calculation method which could be used in high resolution non-hydrostatic mesoscale models.

1.2 Wet Scavenging

The amount of O_3 and aerosol formed in the UT depends on the net convective transport of gases that are soluble and reactive in the aqueous and/or ice phase. In the UT, O_3 formation requires nitrogen oxides (NO_x, the sum of nitric oxide (NO) and nitrogen dioxide (NO_2)) and hydrogen oxides (HO_x, the sum of hydroxyl (HO) and hydroperoxy (HO_2) radicals). The mechanism involves oxidation of NO by HO_2 and organic peroxy radicals (RO_2), followed by NO_2 photolysis and the combination of a resulting excited state O atom with an O_2 molecule. However, due to the short lifetime of HO_x, the amount of HO_x in the UT is determined by the abundance of longer-lived HO_x precursors such as hydrogen peroxide (H_2O_2), methyl hydroperoxide (CH_3OOH), and formaldehyde (CH_2O) (Chatfield and Crutzen, 1984; Prather and Jacob, 1997), which are soluble and have aqueous phase chemical sources and sinks (Barth et al., 2007a; Carlton et al., 2007). H_2O_2 is formed by the reaction of HO_2 radical with itself. CH_2O and CH_3OOH come from oxidation of methane and other hydrocarbons. NO_x is produced in the UT by lightning. The amount of NO_x in the UT is also affected by the convective transport of NOx from the PBL, as well as transport of the NO_x reservoir species nitric acid (HNO_3) (Grassian, 2005), which is readily scavenged by cloud water and ice particles (Neu and Prather, 2012). Furthermore, the formation of aerosols in the

UT is affected by the deep convective transport of sulfur dioxide (SO_2) which is an important source of sulfate aerosol in the UT.

Pickering et al. (2001) conducted an analysis of chemical transport during the 1999 Pacific Exploratory Mission (PEM) Tropics B mission to study the role of the South Pacific Convergence Zone (SPCZ) in redistributing ozone and other trace gases in the southwestern tropical Pacific. They used a two-dimensional cloud-resolving model to simulate the convective transport, lightning NO_x and wet scavenging process. Comparing the model with aircraft observations in the storm anvil, they found that at least 90% of the HNO_3 and H_2O_2 had been removed during the vertical transport through the cloud. The scavenging efficiency of less soluble species such as CH_3OOH was lower than 50%. Barth et al. (2007b) compared the trace gas mixing ratio results of from eight cloud-resolving model simulations of an isolated storm observed during the 1996 STERAO (Stratospheric-Tropospheric Experiment: Radiation, Aerosols, and Ozone) field campaign. Substantial uncertainties existed in the scavenging efficiencies of O_3 precursors that were soluble and/or reactive in cloud droplets (i.e. H_2O_2, CH_2O, and HNO_3) in convective outflow due to differing microphysics and assumptions about retention of chemical species during cloud drop freezing.

A number of physical processes within the convective core and anvil affect the net transport of soluble species by deep convective clouds, including dissolution in cloud water, removal by precipitation and evaporation and release of dissolved gases. When droplets freeze part of the dissolved gases may be released and part retained in

ice. Collectively, these processes are referred to as wet scavenging. The fraction of trace gas that dissolves in cloud water is governed by Henry's Law. The Henry's Law coefficients vary greatly between species, with HNO_3 being extremely soluble and CH_3OOH being the least soluble among the species mentioned above.

Observed ice retention fractions from field experiments and laboratory studies are highly variable. For example, Iribarne and Pyshnov (1990) estimated the retention fraction for H_2O_2 to be around 1, Snider and Huang (1998) found that the retention fraction for H_2O_2 should be 0.05, and von Blohn et al. (2011) found this value to be 0.64±.011. Nevertheless, since highly soluble gases nearly completely dissociate in the liquid phase, they tend to be more highly retained in ice than less soluble species. For example, HNO_3 has been found to be completely retained (Iribarne and Pyshnov, 1990; von Blohn et al., 2011), while a value of 0.62 has been observed for SO_2 (Iribarne et al., 1990), which is less soluble than HNO_3.

Bela et al. (2016a, 2018) conducted high-resolution simulations with the WRF-Chem to examine wet scavenging of soluble trace gases including H_2O_2, CH_3OOH, CH_2O, HNO_3, and SO_2, in storms observed during the Deep Convective Clouds and Chemistry (DC3) field campaign. They found that the simulated scavenging efficiencies (SEs) of all species except HNO_3 are highly sensitive to the values specified for the fractions retained in ice when cloud water freezes. Their suggested ice retention fractions are 1.0 for CH_3OOH, 0-0.5 for CH_2O, and 0-0.25 for H_2O_2. Significant differences in SEs among storms and species were found in the simulated

HNO_3 and SO_2, which preclude them from constraining the ice retention fractions for these two species.

1.3 Lightning NOx Production

Production of NO by lightning (LNOx) is an important part of the summertime NO_x budget over the United States (e.g., Allen et al., 2012). Lightning produces NO_x primarily in the middle and upper troposphere where NO_x is longer lived and can be more efficient at producing ozone than in the boundary layer.

Great uncertainty (a factor of four globally) exists in the estimate of the LNO_x source, which is due to both an uncertainty in the total number of flashes and the amount of NO_x generated per flash. Uncertainty in the number of flashes has been reduced through satellite observations (Optical Transient Detector, OTD, and Lightning Imaging Sensor, LIS), leaving the production of NO_x per flash as the major uncertainty. Previous studies estimated the NO production per flash based on theoretical analyses, model studies, in situ aircraft measurements during aircraft campaigns, and satellite observations. Based on the satellite observations, the LNO_x production rate is 32-246 mol/flash (Beirle et al., 2006; 2010; Bucsela et al., 2010; Pickering et al., 2016). The LNO_x production rate concluded from the aircraft measurements is 55-385 mol/flash (Huntrieser et al., 2008; 2009; 2011; Ridley et al. 2004). Results from cloud-resolving models constrained by aircraft observations (DeCaria et al., 2000; 2005: Ott et al., 2007, 2010) suggest a higher LNO_x production rate from 345 mol/flash to 700 mol/flash. The theoretical and laboratory results show

LNO_x production rates of 604-1100 mol/flash for cloud-to-ground flashes and 38-110 mol/flash for intra-cloud flashes (Price et al., 1997; Wang et al. 1998; Allen et al., 2012; Koshak, 2014). There remains uncertainty concerning whether on average an intra-cloud flash produces less LNO_x per flash than does a cloud-to-ground flash. Nault et al. (2016) indicates that some of these estimates may be biased low because they assume an upper tropospheric lifetime of NO_x of a few days while the actual lifetime (based on DC3 observations) during the first six hours of daytime NO_x transport from lightning flash locations may be only on the order of 3 hours.

There are also some uncertainties in the vertical distribution of LNO_x. Pickering et al. (1998) estimated the vertical profiles of LNO_x based on the results from a 2-D cloud-scale tracer transport model using variables computed in the two-dimensional cloud-resolving Goddard Cumulus Ensemble (GCE) model. Average profiles of LNO_x mass computed for the mid-latitude continental, tropical continental, and tropical marine regimes showed a C-shaped vertical distribution of LNO_x mass. The maximum in the LNO_x mass profile located in the UT, usually within 2-4 km of the tropopause, which resulted from a combination of upward transport of cloud-to-ground flash emissions in storm updrafts and production from intracloud flashes in the upper portion of the cloud. Another peak was near the surface, which was caused by the downdraft. And for all three regimes, the minima appear typically in the 2-5 km layer. Ott et al. (2010) used a 3-D cloud-scale chemical transport model including a parameterized source of LNO_x to simulate six mid-latitude and subtropical thunderstorms. Their results suggested that a large percentage of LNO_x remains in the middle and upper

troposphere where it originated, and only a small percentage was found near the surface. The vertical profile of LNO_x was more like a backward C-shaped profile.

1.4 Effects of Deep Convection on Upper Tropospheric Ozone

Lightning generated NO_x and vertical transport of ozone precursors play an important role in increasing the ozone-forming potential in the UT convective outflow region, where ozone production is more efficient than in the lower troposphere (Pickering et al. 1990, 1993, 1996; Ott et al. 2007). Pickering et al. (1990) used photochemical modeling results and analysis of field data to evaluate the effects of convective clouds on tropospheric ozone production potential following convective events. They found that outflow from deep convection led to enhanced O_3 production in the upper troposphere hundreds of kilometers downstream from the clouds. Compared to the regions with no convection, the rate of O_3 production in air processed by convection is up to 3-4 times greater. The enhancement rate of the downwind ozone production varies from case to case. Pickering et al. (1992 b) simulated the convective transport of an urban plume during the ABLE 2B field campaign, and found a factor of 35 enhancement in downwind O_3 production. The reason for the variation of the O_3 enhancement came from the differences in the intensity of the cloud vertical motion, initial PBL ozone precursor concentrations and the initial condition of the UT NO_x. Other studies found a maximum O_3 increase of 7-14 ppb/day downwind of active convection (Pickering et al., 1992c; Pickering et al., 1996; DeCaria et al., 2000; DeCaria et al., 2005; Apel et al., 2015).

Allen et al. (2010, 2012) estimate that globally 35-45% of upper tropospheric O_3 has a lightning source, and 15–35% of upper tropospheric O_3 over the United States during June, July, and August comes from lightning NO_x based on the NASA Global Modeling Initiative model results. Martini et al. (2013) analyzed the contribution of North American lightning and anthropogenic emissions to ozone concentrations, and radiative forcing during summers 2002 and 2004 using the global University of Maryland Chemical Transport Model driven by GEOS-4 reanalysis. They found that instantaneous radiative forcing due to ozone produced from anthropogenic emissions ranged from 0.15 to 0.30 W m^{-2}, while that due to ozone produced from lightning NO emissions ranged from 0.20 to 0.50 W m^{-2} in summer 2004, with a 30% increase compared to the results in summer 2002. Liaskos et al. (2015) used the GEOS-5 global model to investigate the sensitivity of tropical tropospheric composition (i.e. NO_x, O3, OH, HNO_3, and PAN) to the LNOx source strength. They found that increasing the LNO_x production rate by a factor of 4 (from 123 to 492 mol /flash) led to enhancements of greater than 100% in tropical UT NO_x, hydroxyl radical (OH), HNO_3, and peroxyacetyl nitrate (PAN), as well as the enhancement of O_3 of up to 60%, which subsequently led to a factor-of-three increase in the mean net radiative flux due to ozone at the tropopause.

1.5 Objectives of This Research

In order to assess the effects of deep convective transport of trace gases and aerosols on climate, the simulation of the convective transport, wet scavenging, and LNO_x production need to be accurate in global and regional chemistry and climate

models. My work aims to fill in the gaps on the current knowledge of deep convective transport and wet scavenging and to improve regional model simulations for these processes and use the improved model to compute UT ozone production downwind of a major convective system.

Specifically, my work focuses on analyzing and simulating the deep convective transport and wet scavenging of trace gases in storms that occurred during the 2012 DC3 field experiment (Barth et al., 2015) with the following overarching goals:

(i) Analyze differences in deep convective transport characteristics among three convective regimes: an air mass thunderstorm, a multi-supercell case, and an MCS case.

(ii) Evaluate the cloud parameterized subgrid deep convective transport in a supercell and MCS case.

(iii) Evaluate the wet scavenging of the DC3 storms at cloud parameterized resolution.

(iv) Estimate UT ozone production downwind of a DC3 multi-supercell storm.

To achieve these goals, the following methods are used:

(i) For the analysis of the deep convective transport characteristics from three convective regimes, WRF-Chem simulations are conducted at cloud resolved resolution (0.6 km, 1 km, and 3 km) for all three convective cases with atmospheric chemistry and emissions.

   a. Lightning data assimilation is utilized to improve the simulations of storm location, vertical structure and chemical fields.

b. Analyze the vertical flux divergence and level of maximum detrainment layer of each case study to explore the differences in the convective transport characteristics among the three convective regimes.

c. Forward and backward trajectories are used to determine the source of the upper-level detrained air.

d. Tracer experiments are used to evaluate the influence of the rear flow jet on the convective transport within the MCS.

(ii) For cloud parameterized deep convective transport analysis, WRF-Chem simulations of the multi-supercell and MCS storms are conducted at cloud parameterized resolution (12 km and 36 km) with the tracer transport chemistry option.

a. Five different cumulus schemes are tested to determine the best simulation of the storm.

b. The convective closures in the Grell-Freitas (GF) scheme are tuned to improve the simulation of the precipitation.

c. New subgrid convective transport code is included in the GF scheme to conduct trace gas convective transport within the convective cloud parameterization.

d. The model simulated sub-grid convective transport and redistribution of the trace gases are evaluated by comparing them with the aircraft measurement and cloud resolved simulations.

e. Examine the CO tendencies due to subgrid and grid scale convective transport.

f. Calculate the contribution percentage of subgrid convective transport of CO.

(iii) For cloud parameterized wet scavenging, WRF-Chem simulations of the multi-supercell storm are conducted at cloud parameterized resolution (12 km and 36 km) with atmospheric chemistry and emissions.

a. Simulate wet scavenging with no ice retention factor

b. Add the retention of some species on frozen hydrometeors to improve model simulation of the soluble species.

c. Test different ice retention efficiencies for each soluble species to improve model simulation.

d. Adjusting the conversion rate of cloud water to rain water.

(iv) Using WRF-Chem with lightning and improved convective transport and wet scavenging parameterizations, compute ozone production downwind of the multi-supercell storm.

a. Predict lightning flash rates.

b. Estimate LNO_x production per flash based on in-cloud NO_x observations and Earth Networks Total Lightning Network (ENTLN) flashes.

c. Simulate transport of convective outflow from Oklahoma to the Southern Appalachian Mountain region.

d. Compare ozone production during downwind transport with aircraft observations in the Appalachian region on the day following the storm.

An overview of the DC3 field experiment and the descriptions of the case study storms are provided in Chapter 2. Chapter 3 analyze differences in deep convective transport characteristics among three convective regimes at cloud resolved resolution. This work has been published as Li et al. (2017). Chapter 4 evaluate the cloud parameterized subgrid deep convective transport (Li et al., 2018a). The cloud parameterized wet scavenging results are shown in chapter 5 (Li et al., 2018b). Some concluding remarks and recommendations for future work are given in the final chapter.

Chapter 2 : DC3 Field Campaign and Case Study Storms

2.1 DC3 Field Campaign

The Deep Convective Clouds and Chemistry (DC3) field campaign was conducted from 15 May through 30 June 2012 and sampled storms in three locations: (1) northeastern Colorado, (2) central Oklahoma to west Texas, and (3) northern Alabama. Barth et al. (2015) describe the full field experiment. The overarching purpose of the DC3 project was to examine the influence of midlatitude continental deep convective clouds on UT composition and chemistry. The field campaign made use of various types of measurements to characterize the dynamical, physical, chemical, and lightning processes during and after active convection.

2.2 Observations

2.2.1 Aircraft Measurements

Three extensively instrumented aircraft platforms were utilized to gather in situ observations in the inflow and outflow regions of the convective storms: (1) the National Science Foundation (NSF)/National Center for Atmospheric Research (NCAR) Gulfstream-V (GV) aircraft, (2) the NASA DC-8 aircraft, and (3) the Deutsches Zentrum fur Luft- und Raumfahrt Falcon aircraft. As the Falcon did not measure the 21 May airmass case and the 11 June MCS case, and lacking the NOx data for the 29 May supercell case, only the GV and DC-8 aircraft data are used in this study (Chen et al., 2014a, 2014b, 2016a, and 2016b). Both aircraft measured a variety of gas phase species, aerosols, radiation, cloud particle characteristics, and meteorological

properties. See Tables 2 and 3 in Barth et al. (2015) for the full GV and DC-8 payload, respectively. In this research, we used 1-minute and 1-second merged data provided from the NASA Langley DC3 Merged Aircraft Dataset Archive (http://www-air.larc.nasa.gov/cgi-bin/ArcView/dc3-seac4rs).

2.2.2 Doppler Radar Data

The radar data used in this study are from the Next Generation Weather Radar (NEXRAD)-Weather Surveillance Radar-1988 Doppler (WSR-88D), with a horizontal resolution of 0.02° latitude and longitude, a vertical resolution of 1 km, and a temporal resolution of 5 min (Homeyer et al., 2014). Vertical velocity data for the 21 May Alabama case were derived from the WSR-88D and Advanced Radar for Meteorological and Operational Research (ARMOR) operated by the University of Alabama in Huntsville (UAH) (Petersen et al., 2005; Mecikalski et al., 2015). For the Oklahoma case, Shared Mobile Atmospheric Research and Teaching (SMART) radar (Biggerstaff et al., 2005; Hill et al., 2013) and National Severe Storms Laboratory (NSSL) National Oceanic and Atmospheric Administration Xband dual-POLarized (NOXP) mobile radars were used to analyze storm vertical velocity.

2.2.3 Upper Air Data

The upper air data for the Alabama region are from UAH Mobile Radiosonde Observation Data (RAOB) and were provided by the University of Alabama-Huntsville (http://data.eol.ucar.edu/datafile/nph-

get/353.100/Readme_DC3_UAH_Mobile_soundings.html). It contained 22 high vertical resolution (1-sec) soundings in locations around northern Alabama and southern Tennessee from 15 May to 15 June 2012. The upper air data for the Oklahoma region are from the NSSL, which deployed a Mobile Global Positioning System (GPS) Advanced Upper-Air Sounding System. It took a total of 39 quality-controlled soundings from 19 May to 21 June 2012 (http://data.eol.ucar.edu/codiac/dss/id=353.105). Routine upper air observations from the National Weather Service (NWS) are also used to provide information on the prestorm environment, as well as atmospheric conditions outside of mobile sounding regions (http://data.eol.ucar.edu/codiac/dss/id=353.040).

2.2.4 Lightning Data

Lightning data are used to improve model simulations and examine the ability of the model to predict lightning flash rates. The data come from two sources: (1) the Earth Networks Total Lightning Network (ENTLN) and (2) Lightning Mapping Array (LMA) in the North Alabama (NALMA) and Oklahoma (OKLMA) regions. Both ENTLN and LMA detect radio emissions (sferics) from cloud-to-ground and intracloud flashes. ENTLN uses low frequency and very low frequency signals, and the LMAs use VHF signals.

2.3 Case Study Storms

For this research, we focus on the analysis of deep convective transport in convective systems of three different convective regimes from the DC3 campaign: (1) an air mass thunderstorm that occurred in northern Alabama on 21 May (Mecikalski et al., 2015), (2) a supercellular storm system that initiated in Oklahoma on 29 May (Bela et al., 2016a), and (3) a linear MCS that took place in the central United States (over Missouri, Arkansas, and Illinois) on 11 June. There is a large degree of uncertainty concerning the relative frequency of each of these types of convection. Doswell III (2001) indicated that linear organization is the most common form of deep moist convective organization and that supercells are relatively rare events with the ratio of supercells to nonsupercells perhaps ~0.1.

2.3.1 21 May Alabama Air Mass Thunderstorm

On 21 May, several deep moist convective storms developed in south central Tennessee and northern central Alabama well ahead of a weak cold front (Mecikalski et al., 2015). Our storm of interest (updraft A in Figure 2.1a) started around 1930 UTC (Coordinated Universal Time) in south central Tennessee. Later, at about 2000 UTC, another updraft (B) formed to the southeast of updraft A. Two distinct maxima in the NEXRAD radar composite reflectivity fields were observed (Figure 2.1). Meanwhile, an isolated cell (updraft/cell C in Figure 2.1a) developed to the south of the main cell near the Tennessee-Alabama border at approximately 1950 UTC. The two northern updrafts (A and B) merged around 2015 UTC, which produced an intensified updraft region (D) (Figure 2.1b) with a maximum upward vertical velocity of ~12 m s^{-1} by

2030 UTC. After 2030 UTC, weak environmental wind shear and a relatively strong cold pool caused an outflow boundary to propagate ahead of the main line of convection. Thus, the vertical motion in the northern cell weakened rapidly, and the storm started to decay. At ~2050 UTC, cell D merged with cell C to form a convective ring (Figure 2.1c). Finally, at the end of the sampling period, widespread multicell convection associated with the gust front organized along a broken line (Figure 2.2) and moved at ~5 m s^{-1} toward the southeast.

The DC-8 and GV aircraft took off at 1600 UTC. Both aircraft approached the study region before convection initiation (CI, i.e., before the composite radar reflectivity of the storm exceeded 20 dBZ). The two aircraft began conducting a trapezoid pattern over the Alabama ground radar and LMA coverage region to measure the chemistry composition at various altitudes in the prestorm environment. The GV flew clockwise above 10.5 km, while the DC-8 flew counterclockwise at 5 km, 3 km, and 1 km (Figure 2.2). At 1940 UTC, the GV moved toward the storm and sampled at several levels above 8 km. At 2040 UTC, the GV flew out of the storm to take measurements at ~10 km in the outflow region to the north of storm and then descended to 1 km. Meanwhile, the DC-8 flew from northwest to southeast of the convection in the inflow region at altitudes of 1 km, 3 km, and 5 km. Then the DC-8 spiraled up and passed across the top of the storm before returning to base. Four sounding balloons were launched during this mission. Two were released before CI at 1528 UTC and 1751 UTC, while the other two were launched after cells were formed at 2037 UTC (Mecikalski et al., 2015, Figure 4) and 2215 UTC. The convective available potential

energy (CAPE) (785 J kg^{-1}) was relatively modest, which hampered the development of appreciable vertical velocities. The ARMOR Doppler velocity data indicated that the maximum vertical velocity over the entire system was only 13.9 m s^{-1}, which was much smaller than the two other storm cases described below.

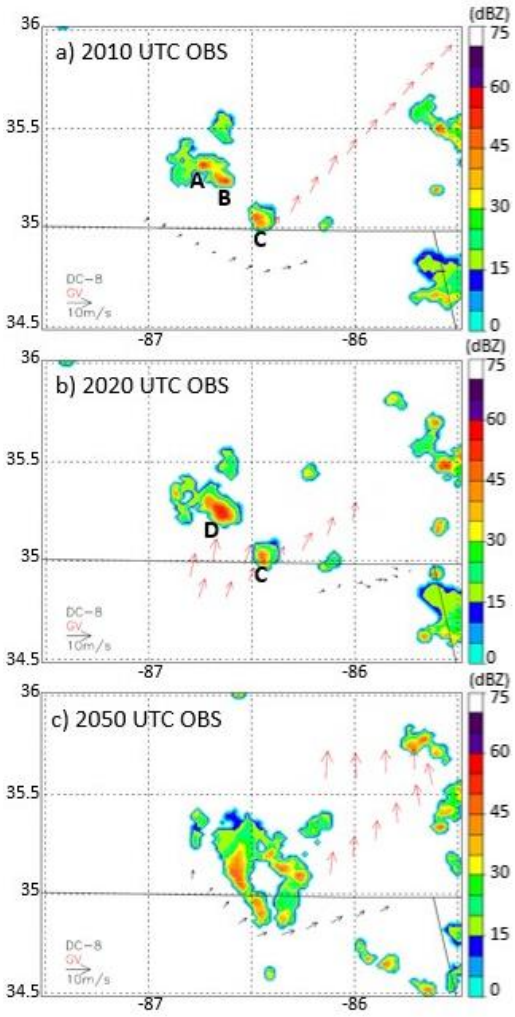

Figure 2.1 NEXRAD observed composite reflectivity (contours) with DC-8 (black arrows) and GV (red arrows) aircraft measured winds (storm motion removed) for the 21 May Alabama air mass storm case at (a) 2010 UTC, (b) 2020 UTC, and (c) 2050 UTC. Length of arrows corresponding to a 10 m s^{-1} wind is shown in the bottom left of each panel. The uppercase letters A–D refer to cells that are specifically discussed in the text.

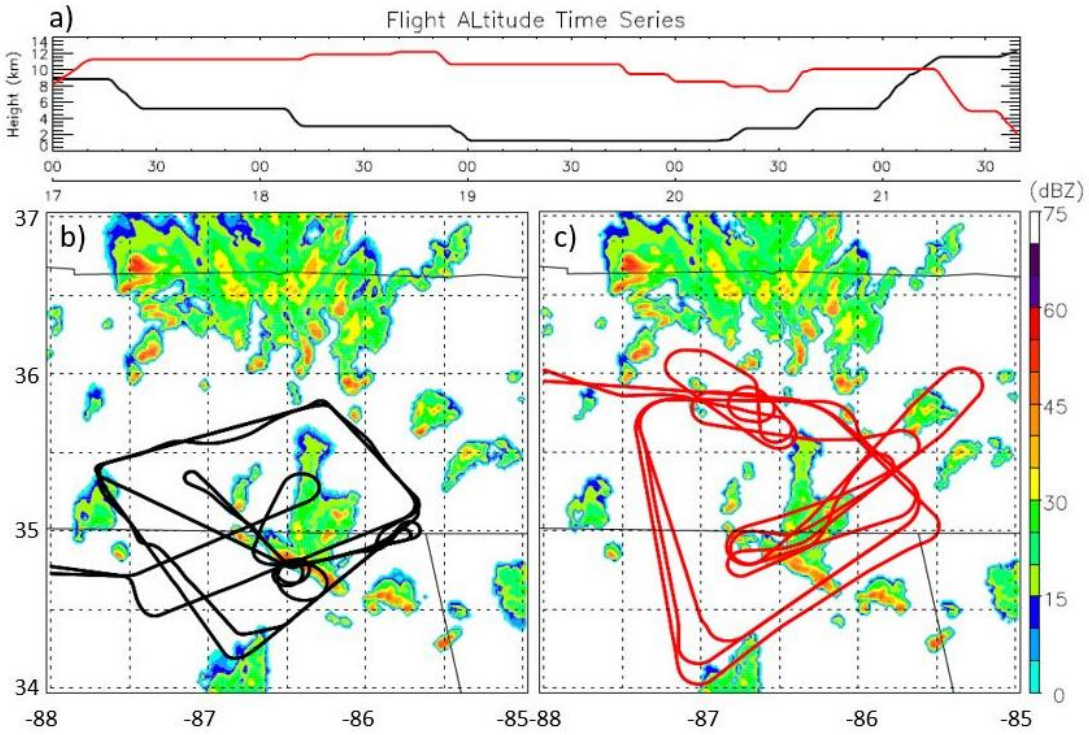

Figure 2.2 (a) 21 May Alabama air mass case DC-8 (black) and GV (red) flight altitude time series from 1700 to 2140 UTC. 21 May Alabama air mass case (b) DC-8 and (c) GV flight tracks superimposed on NEXRAD reflectivity at 2140 UTC.

2.2.2 29 May Oklahoma Supercell Storm System

On 29 May, a thunderstorm system developed on the Oklahoma/Kansas border, around 2110 UTC, to the south of a quasi-stationary front near the Oklahoma and Kansas border. Two isolated cells initiated in the region of interest over northern Oklahoma. Both cells developed several updraft cores. At 2150 UTC, the northern cell was stronger than the southern cell with maximum reflectivity exceeding 60 dBZ (Figure 2.3a). Ten minutes later, both storms had midlevel mesocyclones (DiGangi et al., 2016), marking the beginning of their supercellular stage. Around 2220 UTC, the southern cell split with the left mover merging into new convection to the north (Figure

2.3c). After the merger, the cells continued to strengthen, eventually producing a line of four supercells by 2300 UTC. Additional cells developed both west and east of the line of supercells, with the eastern cells forming a multicell band underneath the anvil of the southern supercell. The supercell complex intercepted a left-moving supercell from the south, which caused the southern supercell in the line to weaken. New supercells developed to the southwest of that merger. By 0300 UTC, the cloud system had evolved into a mostly multicell mesoscale convective system which propagated through central Oklahoma by 0400 on 30 May.

The SMART and NOXP radars sampled the two southernmost supercells in the line from about 2350 UTC on 29 May to 0000 UTC on 30 May. During the sampling time period, the Doppler-derived vertical motion in the southern supercell was sustained at greater than 35 m s^{-1} with several updraft pulses greater than 45 m s^{-1}. The strongest updraft, of about 65 m s^{-1}, was observed at 2330 UTC (DiGangi et al., 2016, Figure 11). The movement of the storm system was approximately 8.5 m s^{-1} toward the southeast.

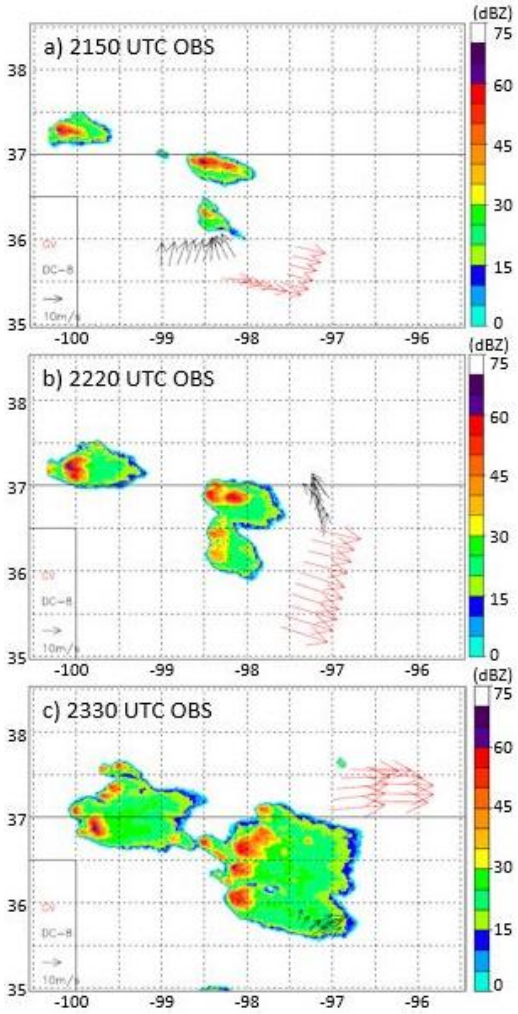

Figure 2.3 Similar to Figure 2.1 but for the 29 May Oklahoma supercell case at (a) 2150 UTC, (b) 2220 UTC, and (c) 2330 UTC.

Prior to the CI, the DC-8 flew down to an altitude of 1 km south of an area of cloud development to take inflow measurements and the GV flew at the same altitude in the western portion of this cloudy region. After convection initiated, the GV ramped up and set up a high-altitude wall to the east of the outflow. The convection and outflow moved toward the GV. Meanwhile, the DC-8 focused on gathering data in the low-level inflow region at altitudes of 1 km, 3 km, and 4.2 km to the east and southeast of the two convective cells. At ~2330 UTC, the DC-8 spiraled up and joined the GV to

sample the outflow on the eastern edge of the storm (Figure 2.4). Three NSSL soundings were launched in the storm region. One was launched before storm initiation at 2029 UTC (CAPE was 3114 J kg^{-1}) (Bela et al., 2016a). The other two were launched after the storm developed at 2255 UTC on 29 May and 0020 UTC on 30 May. The mixed-layer CAPE values at these two times were both quite large: 2562 J kg^{-1} and 3154 J kg^{-1} (DiGangi et al., 2016). The 0–6 km shear was about 24 m s^{-1}.

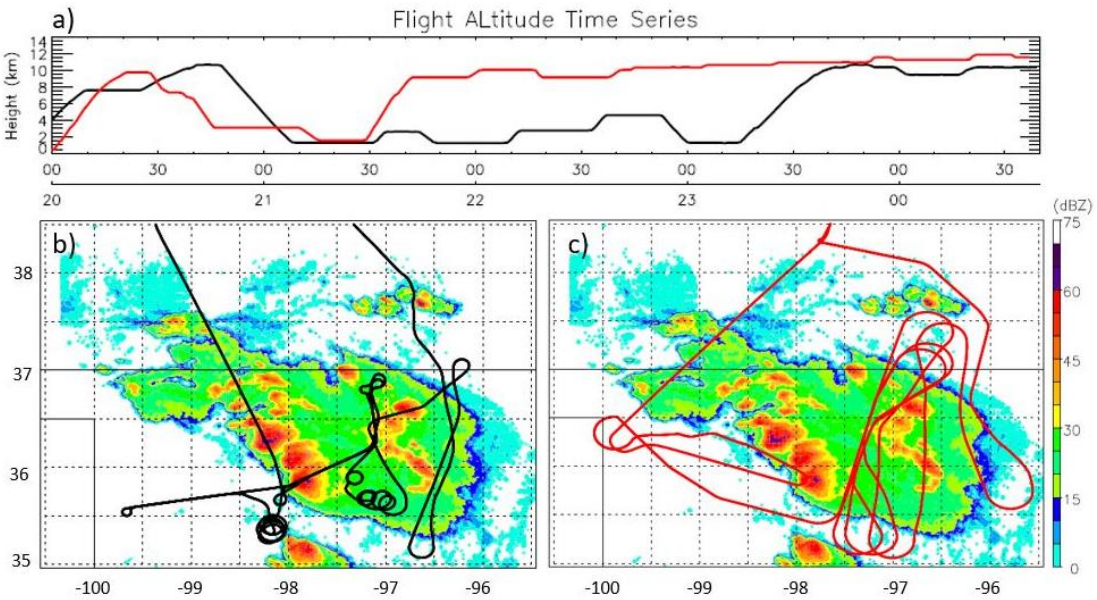

Figure 2.4 (a) 29 May Oklahoma supercell case DC-8 (black) and GV (red) flight altitude time series from 2000 to 0040 UTC. The 29 May Oklahoma supercell case (b) DC-8 and (c) GV flight tracks superimposed on NEXRAD reflectivity at 0040 UTC.

2.2.3 11 June Central United States Mesoscale Convection System

This convective system initiated around 1900 UTC on 10 June. Several strong to severe thunderstorms developed along a line ahead of a sharp cold front that swept across Minnesota, North Dakota, South Dakota, and Nebraska. The main line of storms

moved slowly to the east. At around 0530 UTC on 11 June, the main convective line broke into two parts. The northern storm system began to decay, while the southern part that extended from Wisconsin across Iowa to Kansas gained more strength and started to move southeastward. This MCS was located in the Illinois-Missouri-Arkansas region when sampling started at 1600 UTC (Figure 2.5) and moved southeast at a speed of 16 m s^{-1} reaching the Kentucky and Tennessee region by 2300 UTC. During the aircraft sampling, the MCS maintained its strength and formed a bow echo structure. This was the largest convective system considered in this analysis. The 1200 UTC surface CAPE reached 1147 J kg^{-1} at the Springfield, MO 88-D radar site (KSGF), and 2980 J kg^{-1} at the Little Rock, AR 88-D radar site (KLZK).

The GV took off at 1600 UTC (Figure 2.6) and flew behind the line of convection to measure the outflow produced by the MCS. After 1800 UTC, the GV flew south to Alabama to perform additional sampling there. At 2120 UTC, the GV returned to the northern side of the still active MCS and sampled the outflow region before returning to base. The DC-8 took off at 1557 UTC and reached the MCS at 1700 UTC. The DC-8 flew around the south of the MCS and left for the Alabama region at 1800 UTC. After finishing sampling in the Alabama region, the DC-8 returned to the southern edge of the MCS at 2200 UTC. It made a rapid descent to 0.6 km to take measurements in the inflow region of the MCS.

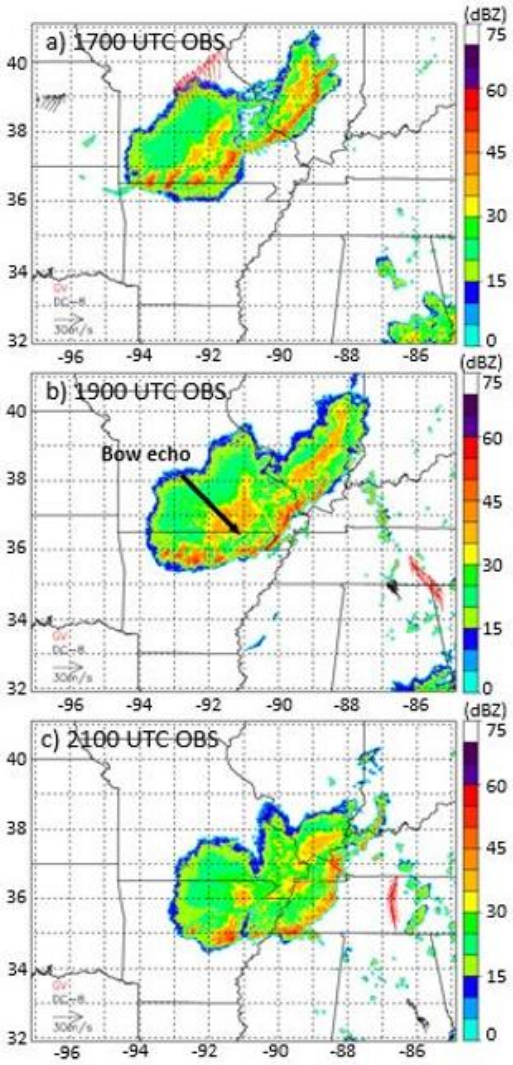

Figure 2.5 Similar to Figure 2.1 but for the 11 June central U.S. MCS case at (a) 1700 UTC, (b) 1900 UTC, and (c) 2100 UTC.

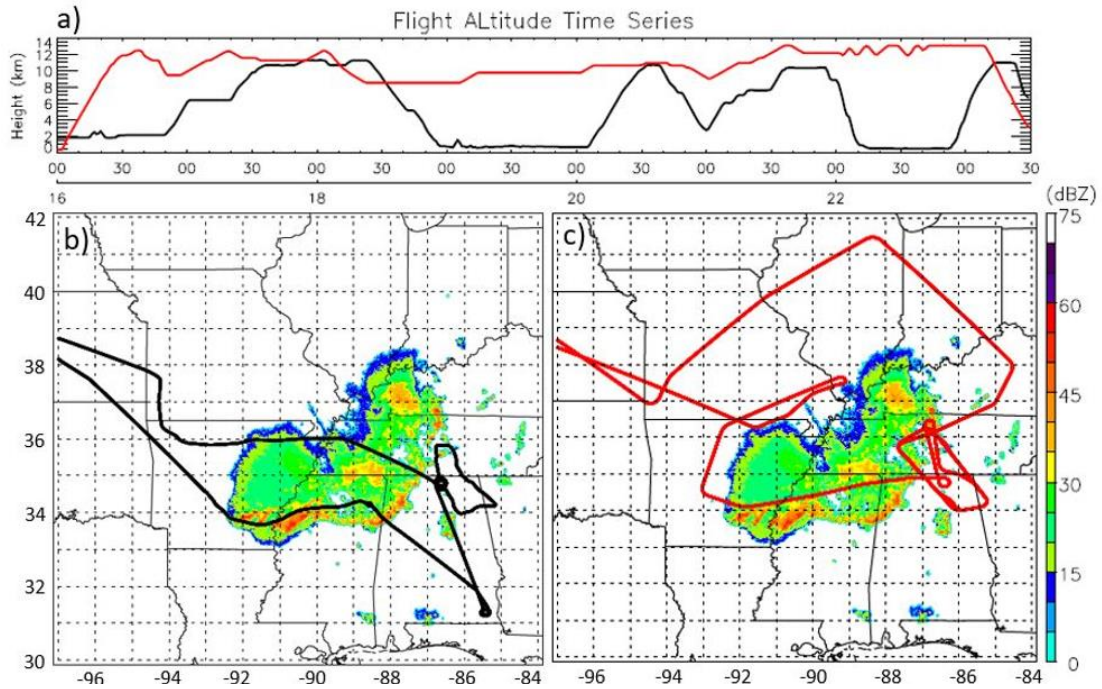

Figure 2.6 (a) 11 June central U.S. MCS case DC-8 (black) and GV (red) flight altitude time series from 1600 to 2230 UTC. 11 June central U.S. MCS case (b) DC-8 and (c) GV flight tracks superimposed on NEXRAD reflectivity at 2230 UTC.

Chapter 3 : Deep Convective Transport Characteristics from Different Convective Regimes

The purpose of this chapter is to examine the underlying causes behind the differences in deep convective transport of trace gases among different scale storms as a function of storm stage, reflectivity, and region (i.e., updraft or downdraft region) through the use of two passive gas tracers and an examination of mesoscale dynamics. WRF-Chem is employed at cloud resolved resolution (0.6 km, 1 km, and 3 km) to simulate three different convective regimes that occurred during the DC3 field campaign: an air mass thunderstorm, a severe supercell thunderstorm, and an MCS case. Lightning data assimilation is utilized to improve the simulation of storm location, vertical structure, and chemical fields. These cloud-resolved simulations will be used in evaluating cloud parameterized simulations in Chapter 4.

3.1 Model Setup

In this research, WRF-Chem with the Advanced Research WRF dynamical core (ARW) (Skamarock and Klemp, 2008) was utilized to simulate the aforementioned three case studies. Lightning data assimilation (LDA) is used to improve the representation of the observed storms in terms of timing of CI. Model output at 10 min intervals was used for the analysis. Sections 3.1.1 and 3.1.2 depict the model meteorology and chemistry setup for the three cases discussed above. Section 3.1.3 describes the method of LDA.

3.1.1 Meteorological Setup

For the 21 May Alabama air mass thunderstorm, the simulations (Table 3.1) were initialized on 21 May 2012 at 1500 UTC using meteorological initial conditions (IC) and boundary conditions (BC) derived from Global Forecast System (GFS) analysis with a 3 hourly time resolution. The WRF-Chem model simulation was conducted on three domains at cloud-parameterizing scale (15 km horizontal grid) and cloud-resolving scales (3 km and 0.6 km horizontal grids). There were 40 vertical levels with a 70 hPa model top. The time steps for each domain were 75 s, 15 s, and 3 s, respectively. The main physics choices were the WRF Single-Moment 6-class scheme (WSM6) (Hong and Lim, 2006) for microphysical processes, the Grell 3D cumulus parameterization (Grell, 1993; Grell and Devenyi, 2002) with shallow convection activated for the outermost domain, the Rapid Radiative Transfer Model for General Circulation Models (RRTMG) scheme (Iacono et al., 2008) for longwave radiation and shortwave radiation, the Noah scheme (Koren et al., 1999;Tewari et al., 2004) for land surface processes, and the Yonsei University scheme (YSU) (Hong et al., 2006) for PBL mixing.

For the 29 May Oklahoma severe supercell case, the simulations of Bela et al. (2016a) were analyzed. Their simulation of the storm was initialized on 29 May at 1800 UTC with meteorological IC and BC obtained from the 6 hourly 12 km North American Mesoscale Analysis (NAM-ANL). The WRF model simulations were conducted on a 1 km resolution domain with a time step of 3 s and 89 vertical levels. The main physics choices were the two-moment Morrison microphysics (Morrison et al., 2009), the

RRTMG scheme for longwave and shortwave radiation, the Noah scheme for land surface, and YSU for PBL mixing.

Table 3.1 WRF-Chem-LDA model configuration and physics and chemistry options for all the three cases analyzed in this study, which are listed on the top row.

	21 May Airmass	**29 May Supercell**	**11 June MCS**
Meteorology Initial/Boundary Conditions	*GFS 15 UTC*	*NAM 18 UTC*	*NAM ANL 12 UTC*
Chemistry Initial/Boundary Conditions	*DC-8 measurement to generate I.C. & B.C.*	*DC-8 measurement to generate I.C. & B.C.*	*MOZART*
Lightning Data Assimilation	*NALMA*	*ENTLN*	*ENTLN*
Grid Resolution	*15 km, 3 km, 0.6 km*	*1 km*	*3 km*
Vertical Levels	*40*	*89*	*40*
Time step	*75 s, 15 s, 3 s*	*3s*	*15 s*
Cumulus Parameterization	*Grell 3D (in 15km domain only)*	*no*	*no*
Microphysics	*WSM6*	*Morrison*	*WSM6*
PBL	*YSU*	*YSU*	*QNSE*
Longwave Radiation	*RRTMG Scheme for all cases*		
Shortwave Radiation	*RRTMG Scheme for all cases*		
Lightning Schemes	*Price and Rind [1992; PR92] lightning flash rate scheme based on maximum vertical velocity for all cases*		
LNOx Scheme	*DeCaria et al. [2005] NO_x production as implemented by Barth et al. [2012] for all cases*		
Fire Emissions	*FINN for all cases*		
Anthropogenic Emissions	*NEI for all cases*		
Biogenic Emissions	*MEGAN v2.04 for all cases*		
Chemistry Option	*MOZCART for all cases*		

For the 11 June central U.S. MCS case (Table 3.1), the model initiation time was on 11 June 2012 at 1200 UTC. Meteorological IC and BC were derived from the 3 hourly 12 km NAM-ANL. The model simulation was conducted on a 3 km resolution

domain with 40 vertical levels and a model top of 70 hPa. The time step for this domain was 15 s. The main physics choices were WSM6 for microphysics, RRTMG for longwave and shortwave radiation, Noah scheme for land surface processes, and the Quasi-Normal Scale Elimination (QNSE) scheme (Sukoriansky et al., 2005) for PBL mixing.

We tried numerous different combinations of IC/BC conditions, WRF-Chem starting time, PBL schemes, and microphysics schemes in order to obtain the best possible simulation of the inflow, outflow, and vertical transport for each storm. The model setups listed above produced the best representation of each storm. When using NAM-ANL analyses to create the IC/BC, the simulation for the 21 May case resulted in too much precipitation. Thus, for this case, we use GFS to create the IC/BC instead. When evaluating different microphysics schemes coupled with Lighting Data Assimilation (LDA, more details about LDA are shown in section 3.1.3), it was found that employing the LDA together with the Morrison scheme generated a bounded weak echo region which is suitable for the supercell case but not for the other cases. Using different setups for each of the three cases aids in improving the simulations of the different convective regimes and thus allows us to better discuss and document the differences in the transport of insoluble trace gases among the different cases.

3.1.2 Chemistry Setup

For the 21 May air mass and 29 May supercell cases, the DC-8 and GV measured trace gas mixing ratios before convection initiated. Thus, we used these

aircraft measurements to generate the chemical IC and BC within the aircraft sampling altitude range. Above the aircraft sampling altitude range, output from the Model for Ozone and Related chemical Tracers, version 4 (MOZART-4) was used to generate the IC and BC. Below the aircraft sampling range, a constant value of the lowest aircraft observation was used down to the surface. For the 11 June MCS case, no observations were available prior to CI over the region of interest. Therefore, we used MOZART-4 to create the entire chemical IC and BC (Table 3.1). Fire emissions were calculated from the Fire Inventory of NCAR (FINN) data (Wiedinmyer et al., 2011). The 2011 National Emissions Inventory (NEI) data were used to create anthropogenic emissions, and we used the Model of Emissions of Gases and Aerosols from Nature v2.04 (MEGAN) (Guenther et al., 2006; Sakulyanontvittaya et al., 2008) to generate biogenic emissions. Aircraft emission data were obtained from Baughcum et al. (1999).

The chemistry option selected for this work was the MOZART gas phase chemistry (Emmons et al., 2010) and Goddard Chemistry Aerosol Radiation and Transport aerosols (Chin et al., 2002) (MOZCART) using the Kinetic Pre-Processor library. Photolysis rates were calculated using the Madronich Fast-Tropospheric Ultraviolet-Visible photolysis scheme (F-TUV, Tie et al., 2003). In addition, lightning flash rate and lightning NO_x (LNO_x) parameterizations were activated (see Table 3.1).

3.1.3 Lightning Data Assimilation

A lightning data assimilation (LDA) technique was employed to improve the WRF meteorological simulations. Based on Fierro et al. (2012, 2014, 2015), the following

nudging equation was applied at observed lightning locations (i.e., grid columns) to locally increase the water vapor mass mixing ratio to near or above its saturation value (with respect to liquid) in a confined layer within these columns:

$$Q_v = AQ_{sat} + BQ_{sat}\tanh(CX)\left[1 - \tanh\left(DQ_g^{\alpha}\right)\right] \quad (3.1)$$

where Q_v is water vapor mixing ratio, Q_{sat} is water vapor saturation mixing ratio, X is total flashes, and Q_g is graupel mixing ratio. A, B, C, D, and α are LDA coefficients.

The injection of water vapor (Qv) increases the local perturbation virtual potential temperature, which increases the buoyancy accelerations and, ultimately, leads to the development of convection. In the simulations of the 21 May and 11 June cases, the values of the LDA coefficients were set to A = 0.93, B = 0.2, D = 0.25, and α = 2.2. Some modifications were made to the Fierro et al. (2012) LDA scheme to improve the representation of the convective three-dimensional kinematical structure. First, the coefficient A = 0.81 in Fierro et al. (2012) was increased to 0.93 similar to Fierro et al. (2014, 2015) to increase the grid volume where Qv is adjusted. In the Fierro et al. studies the Qv increase was confined to midlevels within the graupel-rich, mixed phase region between 253 K and 273 K. In this study, however, Qv was increased over a slightly deeper layer rooted at lower levels, namely, between 285 K and 261 K. These isotherms correspond, respectively, to the lifted condensation level and the level of maximum vertical velocity. This change was motivated by the findings of Marchand and Fuelberg (2014) and Fierro et al. (2016), which suggest that increasing Qv in the lower troposphere (below 700 hPa) instead of the mixed-phase region allows convection to become more quickly rooted in the PBL and, in turn, better represents

weakly forced moist convection. The value of C is based on the gridded number of flashes. In the original nudging equation, the product of C and total flashes controls the shape of the hyperbolic tangent function. We chose a different value of C for the 21 May case, because a different lightning data source was used for that case study. For the 21 May Alabama case, the NALMA VHF source data were employed, because of its ability to better depict the location of the storms cores. By virtue of their different range of frequency detection, the number of NALMA source data are, by design, larger than the number of ENTLN stroke data at a given point. Thus, the value of C had to be scaled accordingly. The 11 June case did not have VHF measurements; therefore, the ENTLN data were used instead.

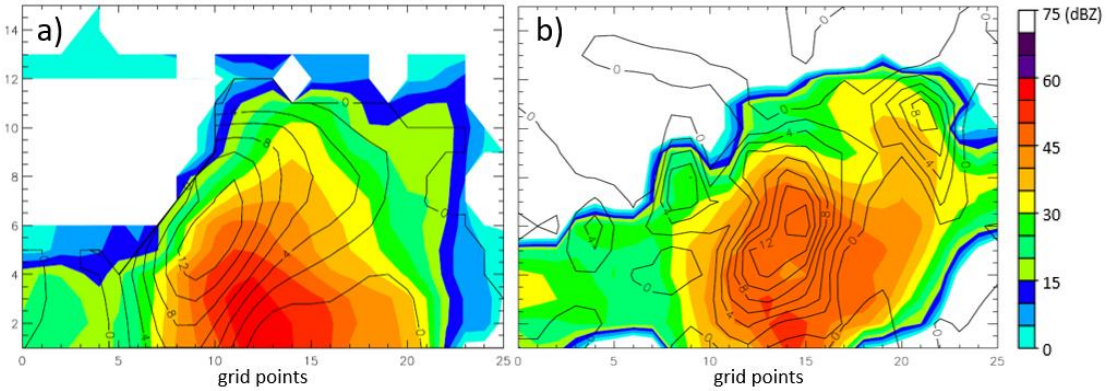

Figure 3.1 21 May 2030 UTC (a) ARMOR observed and (b) WRF-Chem-LDA simulated vertical cross-sections in the x-z plane along the black solid line highlighted in Figure 1f. The shadings represent the reflectivity fields in dBZ, and the black contours show the vertical motion. The distance between two grid points is 1 km.

The aforelisted changes in the coefficients of the LDA scheme of Fierro et al. (2012) helped WRF-Chem reproduce a better vertical velocity structure (Figure 3.1). For the 21 May case, a damping option was also added in the LDA scheme to suppress peripheral spurious convection. Specifically, during the 3 h period prior to CI, the

relative humidity was reduced to 75% throughout the domain within the layer that extended from the lifting condensation level (LCL) to 6 km altitude.

3.2 Model Simulation Results

3.2.1 Meteorology Results

NEXRAD composite reflectivity fields for the 21 May storms are evaluated against the WRF simulations with and without LDA in Figure 3.2. The model failed to simulate the storm without the help of LDA. Figure 3.3 shows the evolution of the 21 May storm in WRF-Chem with LDA. For the 29 May case, the storm location, size, and structure (intensity, anvil height, and extent) are well represented by the model with LDA compared to NEXRAD (Figure 3.4), but CI in the model occurs approximately 40 min later than was observed (Bela et al., 2016a). Figure 3.5 compares NEXRAD composite reflectivity with the WRF-Chem LDA simulation for 11 June. Without LDA, the MCS begins to dissipate during the aircraft measurement time period. With the aid of LDA, the simulated MCS develops along the observed storm track and maintains its strength.

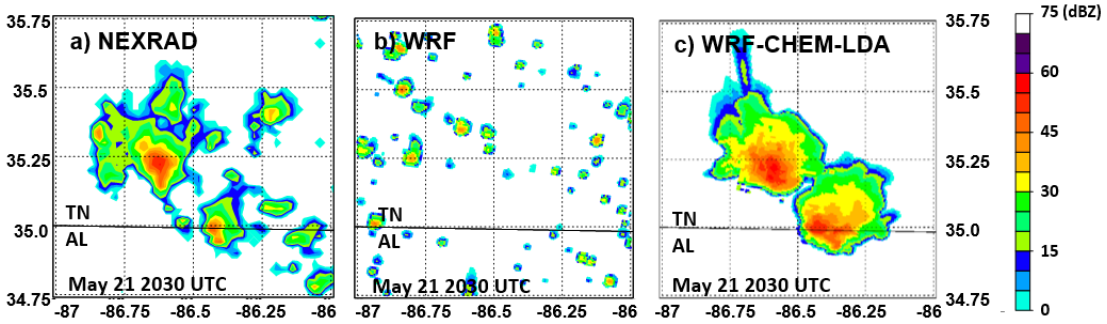

Figure 3.2 Composite reflectivity at 2030 UTC on 21 May from (a) NEXRAD, (b) WRF simulation without lightning data assimilation, and (c) WRF-Chem simulation with lightning data assimilation.

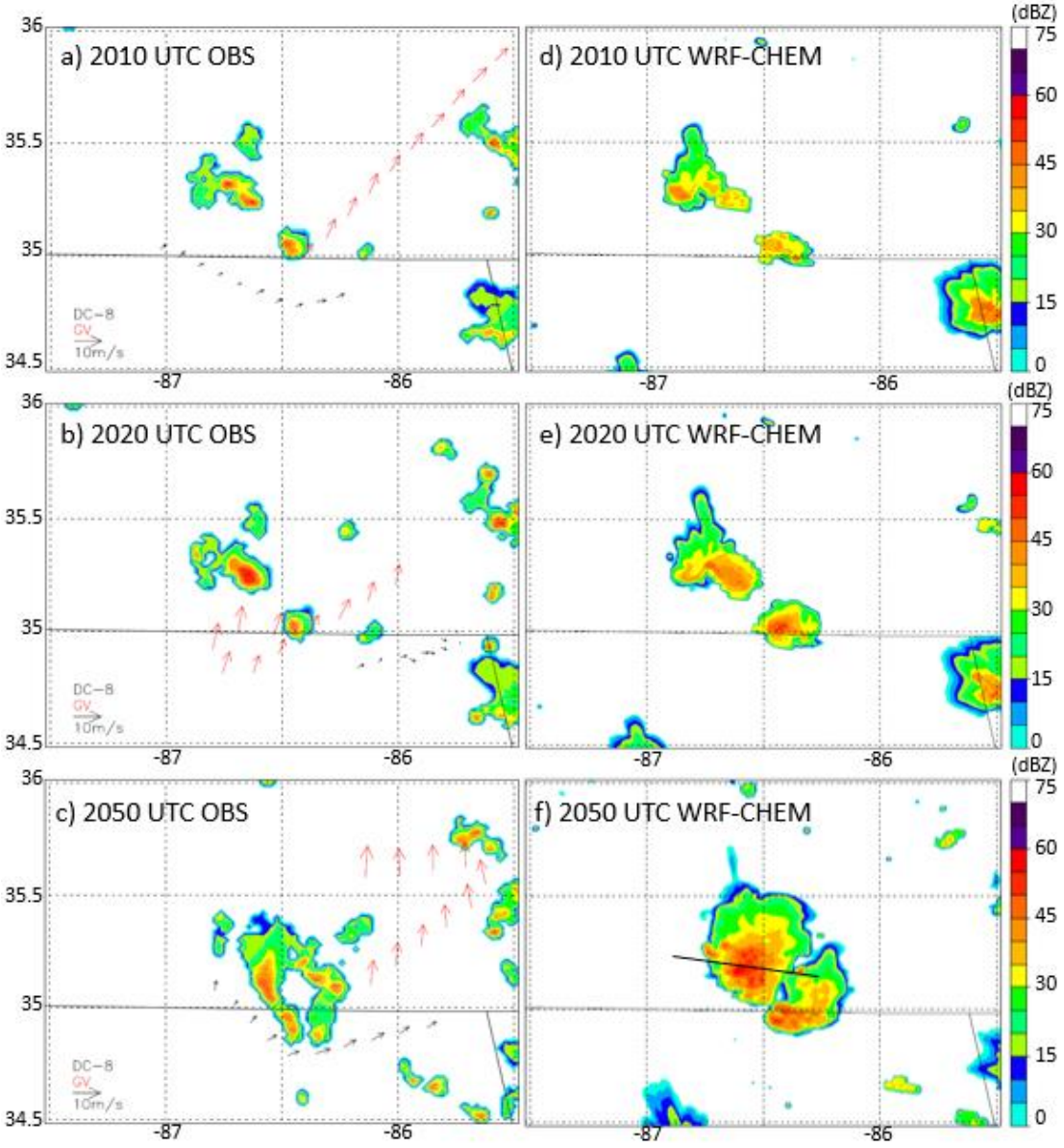

Figure 3.3 WRF-Chem simulated composite reflectivity (d-f) compared with NEXRAD observed composite reflectivity (a-c) at the observation times: (a, d) 2010 UTC, (b, e) 2020 UTC, and (c, f) 2050 UTC. The black solid line in Figure 3.3f is the cross-section line for Figures 3.1 and 3.10.

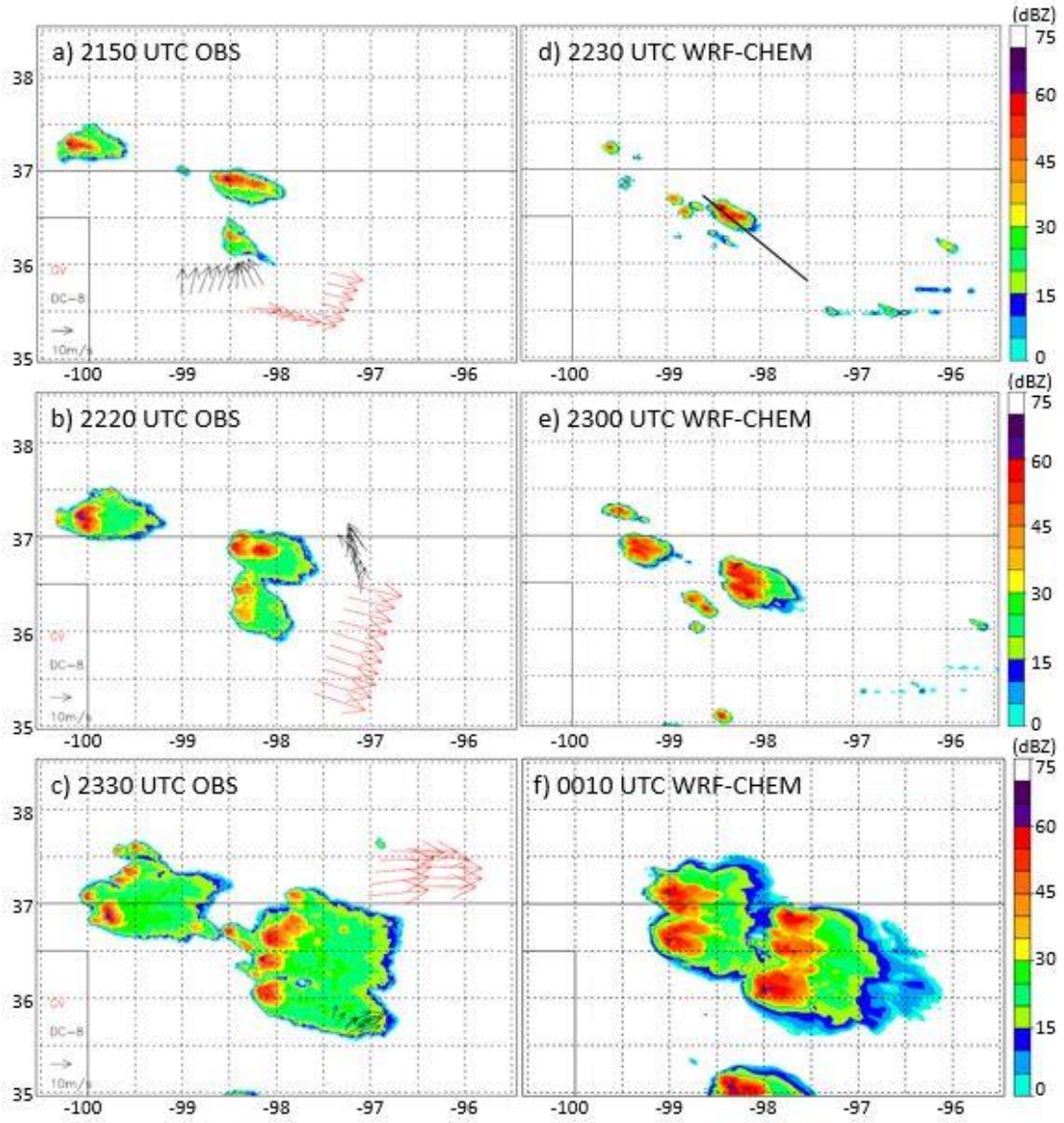

Figure 3.4 Similar to Figure 1 but for the 29 May Oklahoma supercell case at observation times: (a) 2150 UTC, (b) 2220 UTC, and (c) 2330 UTC; model times: (d) 2230 UTC, (e) 2300 UTC, (f) 0010 UTC. The black solid line in Figure 3.4d is the cross-section line for Figure 3.11.

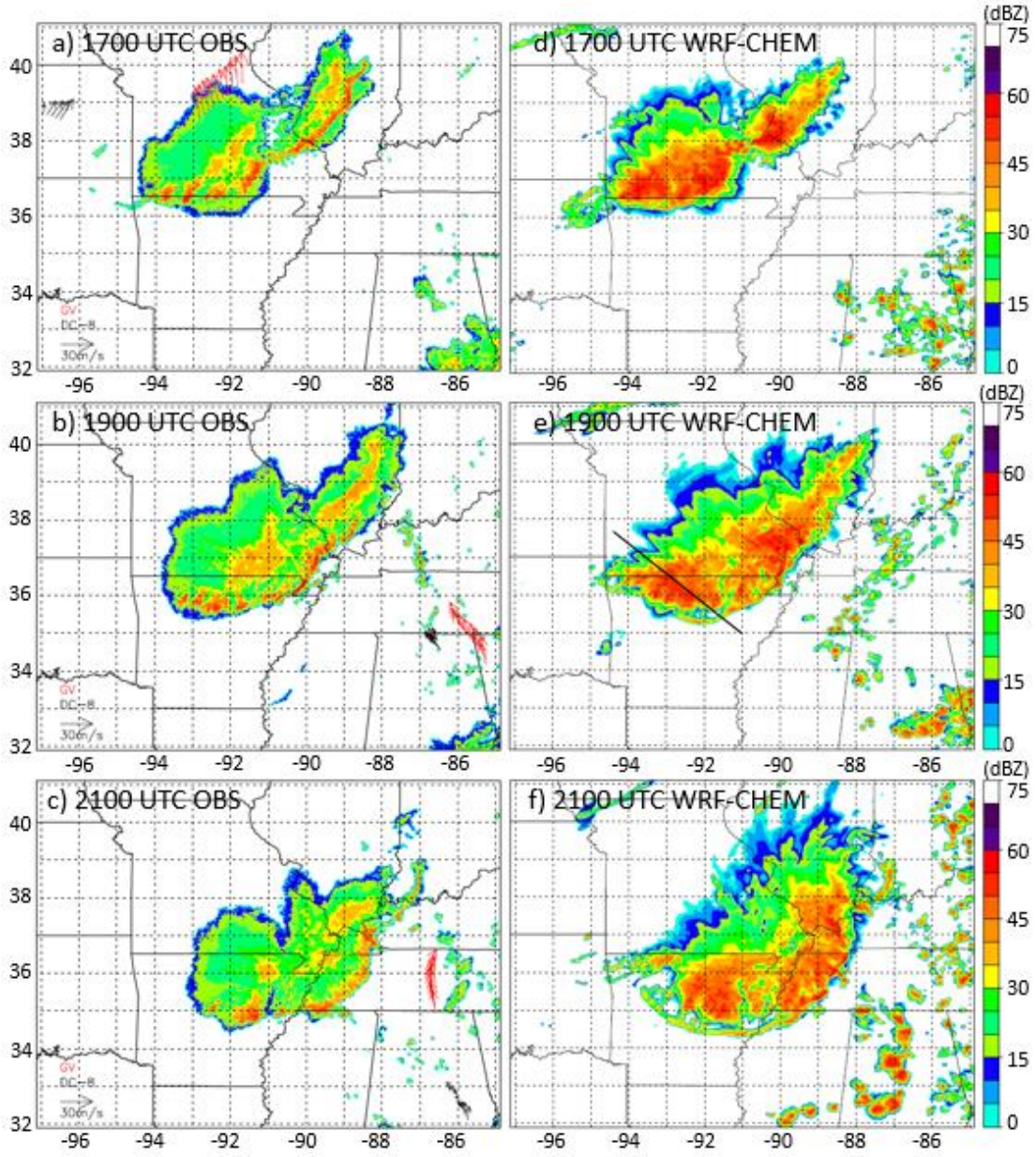

Figure 3.5 Similar to Figure 3.3 but for the 11 June central U.S. MCS case at (a and d) 1700 UTC, (b and e) 1900 UTC, and (c and f) 2100 UTC. The black solid line in Figure 3.5e is the cross-section line for Figure 3.12.

3.2.2 Chemistry Results

The simulated chemistry fields are reasonably consistent with observations for the three cases. In this study, CO was chosen as an example tracer to study the vertical transport because its source is primarily in the PBL. The WRF Chem-LDA-simulated

low-level inflow and high-level outflow CO and O_3 mixing ratios are evaluated against aircraft measurements for each case (Table 3.2). Model simulated CO mixing ratio in low-level inflow was within 5% of the aircraft measurements in all three cases. Simulated CO in the outflow region of the 29 May and 11 June cases were remarkably well reproduced by the model. For 21 May, however, the model underestimated CO by ~6%. The error for ozone in the storm outflow ranged from -9% to +6% over the three cases. The time periods of aircraft inflow and outflow measurements are shown in Table 3.3 which is based on Fried et al. (2016). Moreover, the difference between the upper-level CO mixing ratio in the storm affected region (polluted air) and unaffected region (background clean air) is frequently used to evaluate the overall strength of a storm. Therefore, the good comparison of observed and simulated CO mixing ratio (Table 3.2) provides compelling evidence that the transport in our simulations is reliable.

Table 3.2 Mean CO and O_3 mixing ratios (ppbv) from aircraft measurements and WRF-Chem-LDA simulations

		Low-level inflow		Upper-levels			
				Affected by storm outflow		Unaffected by storm outflow	
		CO	O_3	CO	O_3	CO	O_3
21 May	Aircraft	150.5 (±9.6)	71.4 (±3.0)	100.2 (±4.5)	143.4 (±25.2)	75.1 (±3.4)	214.3 (±7.6)
	WRF-Chem	152.5 (±2.2)	61.8 (±2.3)	94.2 (±6.7)	147.3 (±25.2)	79.7 (±0.4)	213.0 (±14.3)
29 May	Aircraft	132.3 (±3.1)	32.6 (±0.4)	123.1 (±3.6)	80.0 (±4.8)	104.4 (±5.4)	82.2 (±7.0)
	WRF-Chem	136.3 (±0.3)	44.1 (±3.6)	123.2 (±14.2)	84.7 (±12.9)	96.3 (±3.4)	97.1 (±6.4)
11 June	Aircraft	117.5 (±4.3)	33.9 (±3.5)	107.9 (±5.0)	111.1 (±16.0)	72.6 (±3.1)	155.3 (±20.2)
	WRF-Chem	112.0 (±7.8)	45.9 (±4.2)	108.8 (±2.1)	101.4 (±14.4)	69.8 (±0.7)	161.8 (±6.1)

Table 3.3 Boundary layer inflow (IF) and upper tropospheric outflow (OF) times and altitudes

Date	21 May	29 May	11 June
DC-8 IF Times	19:30:43 to 19:38:00	23:10:21 to 23:15:53	22:29:30 to 22:57:30
DC-8 OF Times	-	23:48:30 to 23:58:30	-
DC-8 IF/OF Altitudes (km)	1.23/	1.3/10.9±0.2	0.6±0.3/
GV OF Times	20:50:30 to 21:14:30	23:59:30 to 24:23:30	21:59:30 to 22:37:30
GV OF Altitudes (km)	10.4±0	11.8±0.1	12.9±0.3

3.3 Deep Convection Vertical Transport Calculation

3.3.1 Vertical Flux Divergence

Deep convective transport was computed following Skamarock et al. (2000). The conservation equation for a passive tracer species can be expressed as:

$$\frac{\partial(\bar{\rho}\phi)}{\partial t} = -\frac{\partial(\bar{\rho}u\phi)}{\partial x} - \frac{\partial(\bar{\rho}v\phi)}{\partial y} - \frac{\partial(\bar{\rho}w\phi)}{\partial z} \tag{3.2}$$

where ϕ is the mixing ratio of the tracer, $\bar{\rho}$ is the mean air density, u and v are horizontal velocities, and w is vertical velocity. Integrating this equation in the horizontal over the domain yields:

$$\frac{\partial}{\partial t}\int_{\Omega} (\bar{\rho}\phi)\partial\Omega = -\int_{\Omega} \frac{\partial(\bar{\rho}w\phi)}{\partial z}\partial\Omega - \int_{\Gamma} (\bar{\rho}u_n\phi)\partial\Gamma \tag{3.3}$$

where z is height, Ω is horizontal domain, Γ is spatial boundaries, and u_n is the boundary-normal velocity. The last term on the right is the net flux through the boundaries, which is smaller than the other two terms during deep convection. Thus, during deep convection, the local rate of change of tracer mass is approximately equal

and opposite in sign to the vertical flux divergence (VFD) of the tracer mass (the first term on the right), which following the Skamarock et al. (2000) formula, is defined as:

$$VFD = \sum \frac{\partial \rho w C_{gas} \frac{M_{gas}}{M_{air}}}{\partial z} dxdy \quad \left(Unit: \frac{\frac{kg}{m^3} \cdot \frac{m}{s}}{m} m^2 = kgm^{-1}s^{-1} \right) \qquad (3.4)$$

where C_{gas} is the volume mixing ratio of the trace gas, M_{gas} is the molar mass of trace gas, and M_{air} is the molar mass of air.

Besides the strength of vertical transport, another aspect that remains critical in the study of deep convective transport is the depth of vertical transport, which informs us of the altitude range affected by PBL pollution due to deep convective transport. Mullendore et al. (2009) used the level of maximum detrainment (LMD) to represent the depth of vertical transport. LMD is the point at which the vertical flux divergence is most negative and horizontal detrainment is at a maximum. The altitude range where vertical divergence is negative is defined as the "detrainment envelope", which is the vertical region of horizontal detrainment.

3.3.2 Upward Vertical Transport at Different Storm Stages

Based on the VFD analysis (section 3.3.1), the LMD and the detrainment envelope were calculated every 10 minutes for each case during the aircraft sampling period (Figure 3.6). During this period, the intensity of the 11 June MCS remained at steady state with a nearly constant altitude for the LMD (Figure 3.6 bottom). For the 21 May airmass case and the 29 May supercell case, CI, development and mature stage

were simulated during the model analysis period. The results illustrate that, in the developing stage, the storm LMD increased in altitude and the depth of the detrainment envelope increased. After the storm matured, the LMD gradually became stable. The mature stage LMD is 11 km for 21 May airmass storm, 12 km for 29 May supercell case, and 13 km for 11 June MCS case.

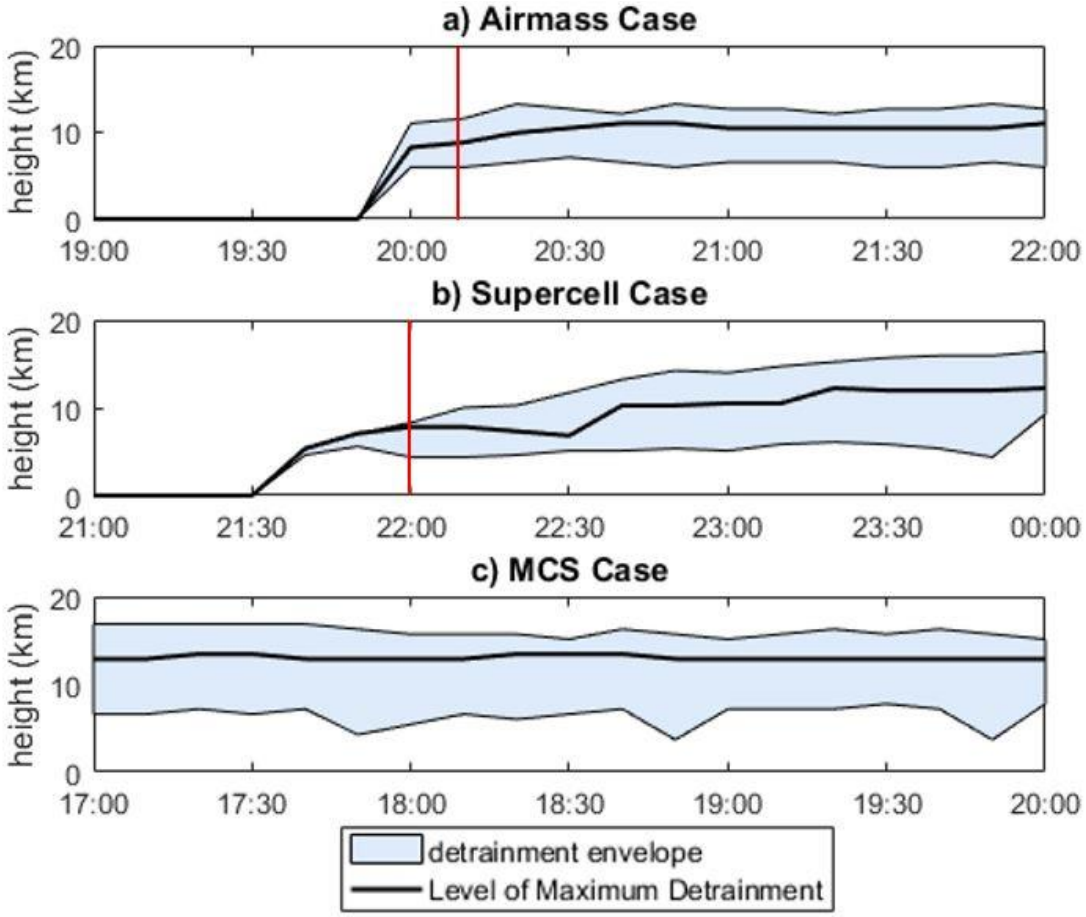

Figure 3.6 Time series showing WRF-Chem-LDA simulated level of maximum detrainment and detrainment envelope for (a) 21 May air mass storm case, (b) 29 May supercell severe storm case, and (c) 11 June MCS case. The red lines in Figures 9a and 9b represent the time of anvil formation.

3.3.3 Upward Vertical Transport at Storm Mature Stage

Using equation 3.4, the upward mass vertical flux divergence (VFD) was estimated every 10 minutes over the whole storm region where composite reflectivity is greater than 0 dBZ. Comparing the VFD for the three cases during the mature stage of each storm (Figure 3.7 top left), it was found that the total upward transport is strongest for the 11 June MCS case and weakest for the 21 May airmass storm. This is because the storm area of the 11 June MCS is much larger than the other two cases, and it transports more air over the entire storm region from the lower levels to upper-levels.

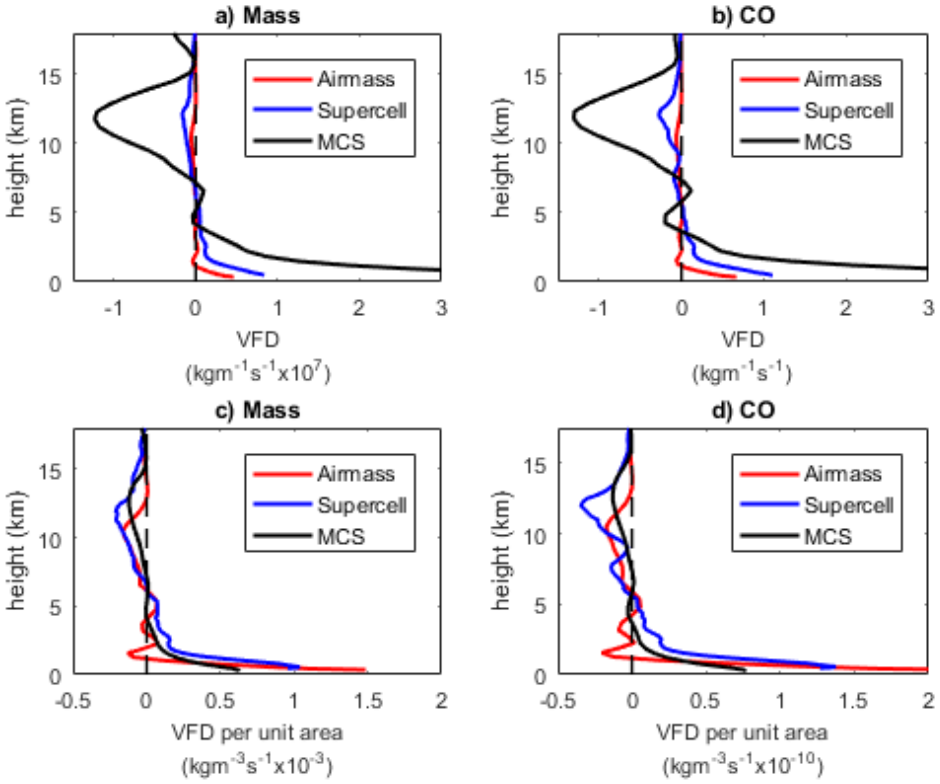

Figure 3.7 Upward VFD of (a) mass and (b) CO for 21 May air mass storm (red), 29 May supercell storm (blue), and 11 June MCS (black); vertical flux divergence per unit area of (c) mass and (d) CO for the three cases.

Overall, the MCS case has the greatest ability to transport trace gases and aerosols from the PBL to the upper troposphere due to its larger size and longer duration. The transport of CO to the UT (above 8 km) for the first hour after the storm becomes mature is 7.2×10^5 kg/hr for the airmass case, 4.57×10^6 kg/hr for the supercell case, and 1.95×10^7 kg/hr for the MCS case. Considering the duration of the system (3 hrs for the airmass case, 6.5 hrs for the supercell case, and 23 hrs for the MCS case), the transport of CO in the MCS case may be ~200 times more than the airmass case, and 15 times more than the supercell case.

Considering the differences in storm size among the three convective cases, we divided the calculated VFD by the area of the region where there was positive vertical velocity, and obtained upward VFD per unit area for each case:

$$VFD\ per\ unit\ area = \frac{\overline{\partial \rho w C_{gas} \frac{M_{gas}}{M_{air}}}}{\partial z} = \overline{\frac{M_{gas}}{M_{air}} \left(\rho w \frac{\partial C_{gas}}{\partial z} + C_{gas} \frac{\partial \rho w}{\partial z} \right)} \qquad (3.5)$$

$$(Unit: = kgm^{-3}s^{-1})$$

The upward transport per unit area is strongest for the 29 May case and slightly less for the 11 June MCS and 21 May airmass cases (Figure 3.7, bottom left). In the lower atmosphere, the inflow layer (i.e., the layer with positive vertical flux divergence and, hence, horizontal convergence) extends from the surface to ~6 km altitude, with the most positive values and largest inflow from the surface to 1 km altitude in all three cases. For the 29 May supercell case, the low-level horizontal convergence (positive VFD) layer extends from the surface to ~6 km, which is 1 km deeper than for the 11 June MCS case. Compared to the other cases, the low-level horizontal convergence

appears more complex in the 21 May airmass case. The latter exhibits low-level horizontal divergence regions (negative VFD) near 1 km and 3.5 km.

Forward and backward trajectories provide a more in-depth depiction of the inflow and outflow structure. 3D renderings of the 3-hour trajectories were calculated and plotted by Visualization and Analysis Platform for Ocean, Atmosphere, and Solar Researchers (VAPOR, Clyne and Rast, 2005; Clyne et al., 2007) using the modeled 3D wind fields (Figure 3.8). The horizontal spacing of the trajectories is 3 km for all three cases. The forward trajectories start from 500 m (top row), 1.5 km (second row), and 2.5 km (third row). The initiation times of the forward trajectories are 1900 UTC for the airmass case, 2100 UTC for the supercell case, and 1700 UTC for the MCS case. The backward trajectories (fourth row) start from the altitude of the LMD (11 km for the 21 May airmass case, 12 km for the 29 May supercell case, and 13 km for the 11 June MCS case). The initiation time of the backward trajectories are 2200 UTC for the airmass case, 0000 UTC for the supercell case, and 2100 UTC for the MCS case. For the 21 May airmass case, the trajectories indicate that most of the high-level air within the LMD started from above 1.5 km (Figure 3.8g), while nearly all of the air that originated at 1.5 km or lower (Figures 3.8a and d) remained below 5 km at the end of the 3-h. On the other hand, in the 29 May supercell case (Figures 3.8b, e, and h) and the 11 June MCS case (Figures 3.8c, f, and i), considerable low-level air was transported to the LMD. Given that the length of the arrows is proportional to the distance traveled in 10 minutes, air in the supercell and MCS cases can be transported from near the surface to the LMD in less than 30 minutes.

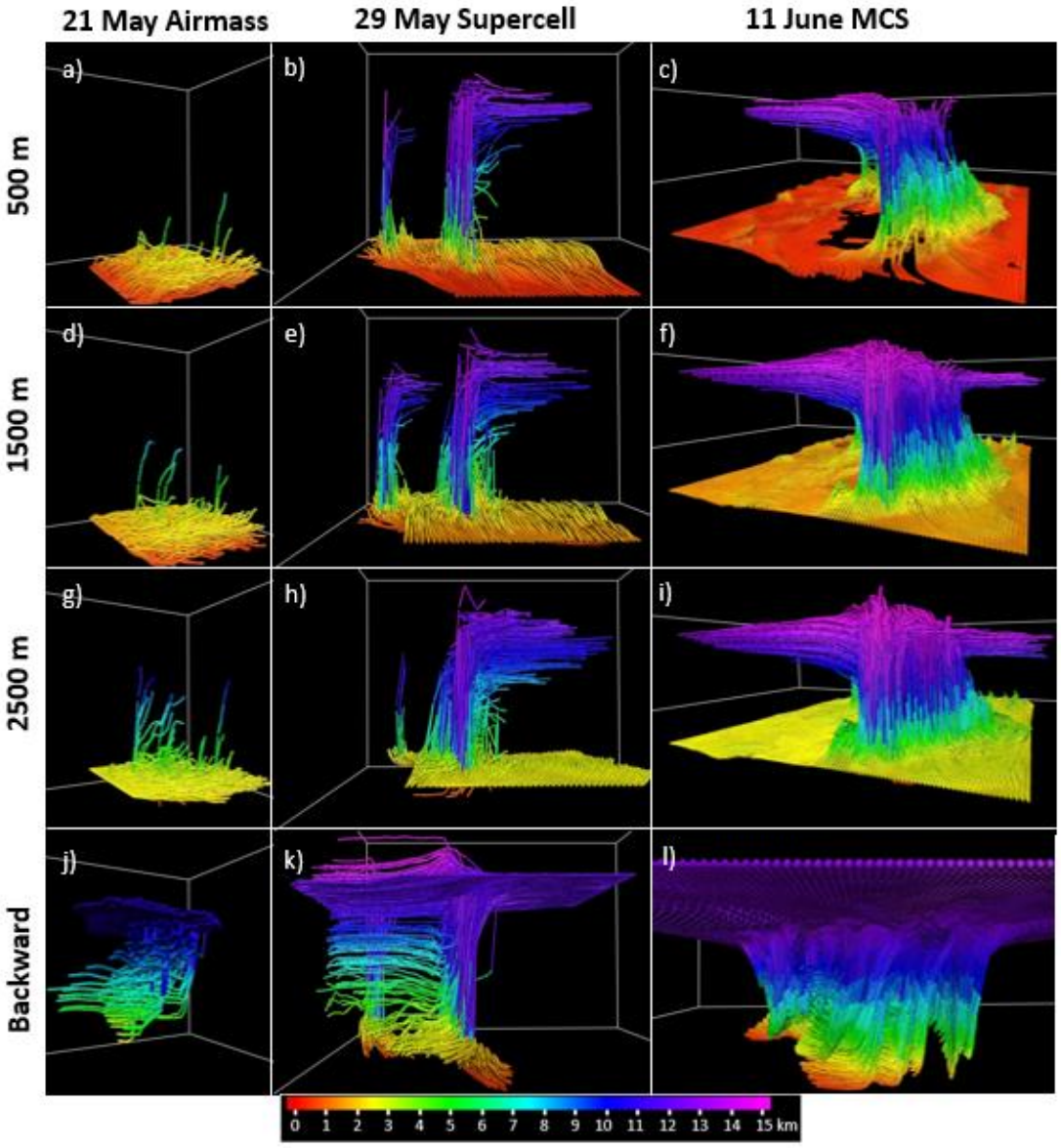

Figure 3.8 Three-dimensional renderings of 3 h forward trajectories from (a–c) 500 m, (d–f) 1.5 km, (g–i) 2.5 km of the 21 May air mass case (Figures 11a, 11d, and 11g), the 29 May supercell case (Figures 11b, 11e, and 11h), and the 11 June MCS case (Figures 11c, 11f, and 11i), and (j–l) backward trajectories from the LMD of the three cases. Each trajectory line consists of 18 arrows with each arrow representing 10 min air trajectory. The color of the arrows represents the ending height of the trajectories. The horizontal resolution of the trajectory seeds is 5 km for all three cases.

Following Mullendore et al. (2009), we use CO as a tracer to calculate the VFD of trace gas. Results (Figure 3.7 lower right) show that the upward transport per unit

area of CO is the strongest for the 29 May case. Comparing the result of the 29 May supercell case with the Skamarock et al. (2000) supercell case, we found that the 3-hour time integrated VFD at LMD for the 29 May case is 11 times larger than the supercell case of Skamarock et al. (2000), while the size of the 29 May storm system is about 10 times greater. Thus, the VFD per unit area of our supercell case is similar to the results of Skamarock et al. (2000).

In order to determine why the vertical flux divergence differs among the three cases, vertical profiles of averaged mass flux density (ρw) and trace gas mixing ratio over the storm region were constructed at the mature stages of each storm and are shown in Figure 3.9 (see also equation 3.5). The mass flux density is largest for the 29 May case. Its large vertical velocity peak reported earlier (~65 m s^{-1}) contributes to relatively large mass flux density as well as vertical gradient of mass flux density that increases the vertical flux divergence throughout the column. The CO profile for the supercell case has a local maximum at 10 km and a larger vertical gradient than the other cases. This gradient (first term on the right of equation 3.5) also contributes to the large CO VFD per unit area on 29 May. Section 3.3.4 discusses the roles of the vertical gradient of mass flux density and vertical gradient of trace gas mixing ratios in VFD in more detail.

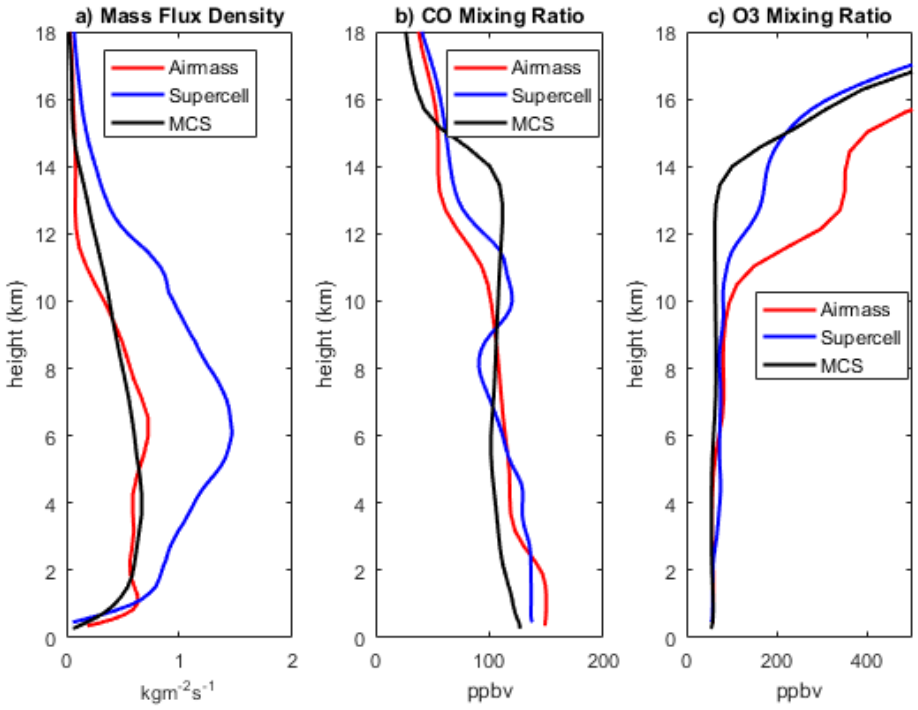

Figure 3.9 Average (a) mass flux density, (b) CO mixing ratio, and (c) O3 mixing ratio vertical profiles in the storm region (composite reflectivity >0 dBZ) at the mature stage for the 21 May air mass case (red), the 29 May supercell case (blue), and the 11 June MCS case (black).

The CO vertical profile is well mixed on 11 June contributing to a relatively low VFD per unit area for this case. In order to understand why the profile is so well mixed on 11 June, we compare CO mixing ratio X-Z cross-sections for the three cases at six different times (Figures 3.10-3.12). The rear side (left side in Figure 3.12) of the 11 June MCS shows evidence of injection of cleaner mid-level air by a rear inflow jet into the lower troposphere, which was not seen in the other two cases. Injection by a rear inflow jet is typical for this type of convection (Houze et al., 1989). A prominent bow echo occurred during the 11 June MCS event (Figure 3.5), which was produced by the mid-level strong rear inflow jet. The jet brought relatively clean mid-level air

into the storm, which then descended in downdrafts. If this relatively clean air also enters the updraft region, it will reduce the CO mixing ratio vertical gradient, as well as CO mixing ratios in the lower atmosphere. Based on equation 3.5, decreasing the CO mixing ratio and/or CO mixing ratio vertical gradient will lead to a decrease of vertical flux divergence.

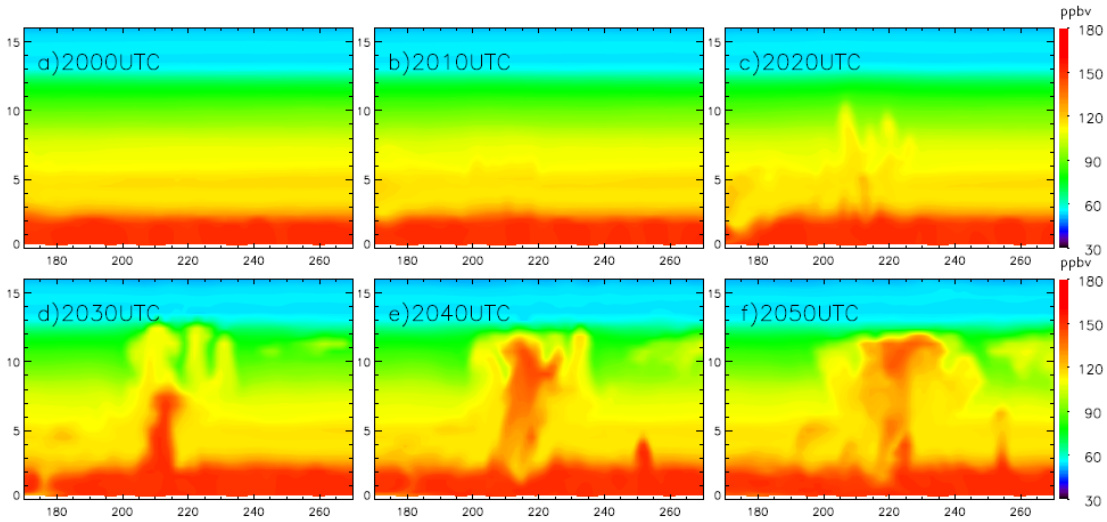

Figure 3.10 WRF-Chem-LDA simulated CO mixing ratio vertical cross-sections along the black solid line highlighted in Figure 3.3f, at (a) 2000 UTC, (b) 2010 UTC, (c) 2020 UTC, (d) 2030 UTC, (e) 2040 UTC, and (f) 2050 UTC on 21 May 2012.

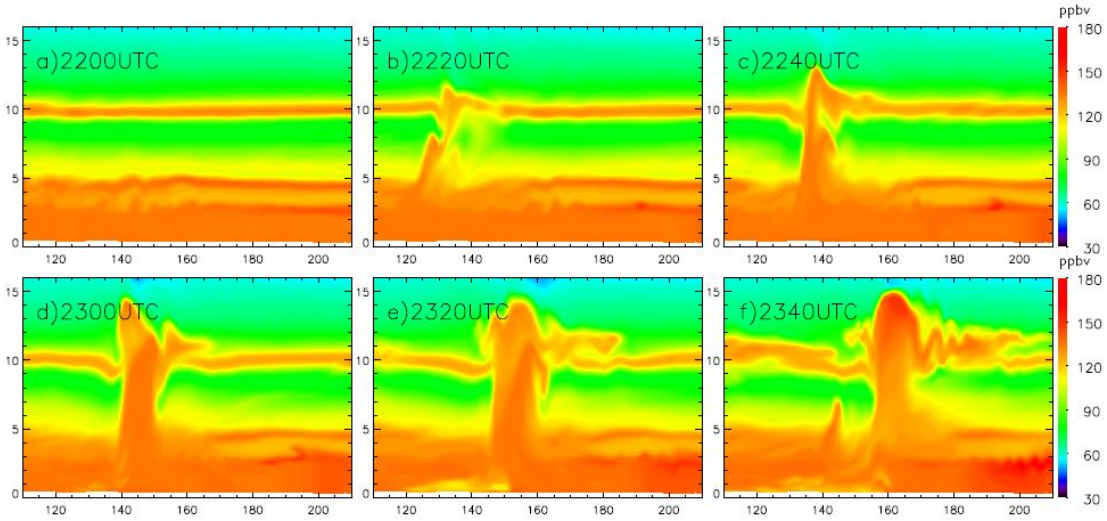

Figure 3.11 WRF-Chem-LDA simulated CO mixing ratio vertical cross-sections along the black solid line highlighted in Figure 3.4d, at (a) 2200 UTC, (b) 2220 UTC, (c) 2240 UTC, (d) 2300 UTC, (e) 2320 UTC, and (f) 2340 UTC on 29 May 2012.

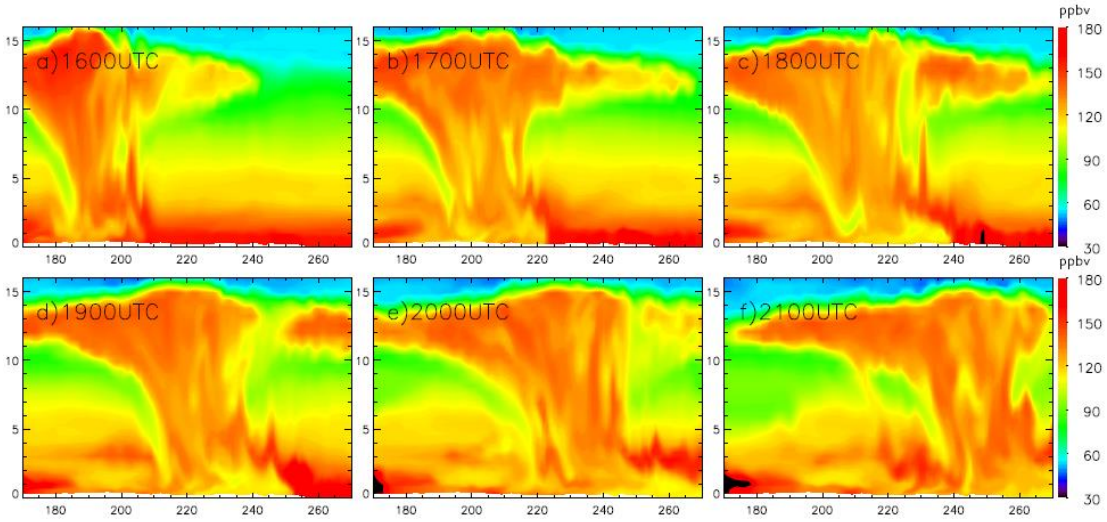

Figure 3.12 WRF-Chem-LDA simulated CO mixing ratio vertical cross-sections along the black solid line highlighted in Figure 3.5e at (a) 1600 UTC, (b) 1700 UTC, (c) 1800 UTC, (d) 1900 UTC, (e) 2000 UTC, and (f) 2100 UTC on 11 June 2012.

In order to test whether the relatively clean air in the rear side of the storm could enter the storm inflow and be transported to the UT, a tracer experiment was designed to determine the amount of the downdraft air that was transported to the upper-levels of the storm. After CI, tracer T was added to the storm downdraft region at one timestep and its mixing ratio was evaluated at upper-levels of the storm (above 8 km) after 60 minutes. The mixing ratio for the tracer was set to 0.1 ppmv in the downdraft region from 0 km to 4 km, and 0 elsewhere. After an hour, we calculated the ratio of upper-level T mixing ratio and the total mixing ratio of T integrated over the model domain. The tracer calculation was performed for the 21 May and 11 June cases. Here, we define the rear inflow ratio as:

$$rear\ inflow\ ratio = \frac{high\ level\ T\ mixing\ ratio}{total\ T\ mixing\ ratio} \tag{3.6}$$

Therefore, the rear inflow ratio increases with the amount of downdraft air entering the updraft. The rear inflow ratio for 21 May is 0.01 after 60 minutes, while

the rear inflow ratio for 11 June is 0.1. Clearly, for the 11 June case, the cleaner downdraft air entered the updraft region. For this case, about 10% of the low-level downdraft air was transported to the UT, which leads to the low value of VFD for CO in the upper troposphere.

3.3.4 Upward Vertical Transport of Different Trace Gases

Different trace gases have different vertical distribution, which affects the vertical transport pattern (equation 3.5). Thus, we choose CO and O_3 as example tracers, which have different and opposite vertical distributions and gradients. Figure 3.13 shows the initial vertical profiles (Figure 3.13a-13c), LMD as a function of time (Figure 3.13d-13f), and VFD (Figure 3.13g-13l) of CO and O_3. From equation 3.5, the following is obtained:

$$VFD(per\ unit\ area) \propto \overline{\rho w \frac{\partial C_{gas}}{\partial z}} + \overline{C_{gas} \frac{\partial \rho w}{\partial z}} \tag{3.7}$$

For CO and O_3, the mass flux density (ρw) and its vertical gradient will be the same, while the trace gas vertical gradients will have opposite signs. Therefore, the sign of the first term on the right hand side (RHS) will differ between CO and O_3 VFDs, while the second term will have the same sign but different amplitudes. Figure 3.14 compares the value of the two terms. We call the first term the trace gas gradient term and the second term the mass flux density gradient term, because they control the sign of each term. In the lower and mid troposphere for all three cases, the mass flux gradient term is much larger than the trace gas gradient term (compare top and bottom rows of Figure 3.14), which means that to first order the product of the trace gas mixing ratio

and mass flux gradient controls the VFD distribution, and the direction of the transport is determined by the mass flux gradient rather than the trace gas gradient. This explains why the VFD distributions for CO and O_3 in all three cases are similar (Figure 3.13g-3.13l), except in the uppermost troposphere and stratosphere where the trace gas gradient term is important for O_3 due to its strong vertical gradient. In this altitude range, the VFD profiles of O_3 and CO diverge.

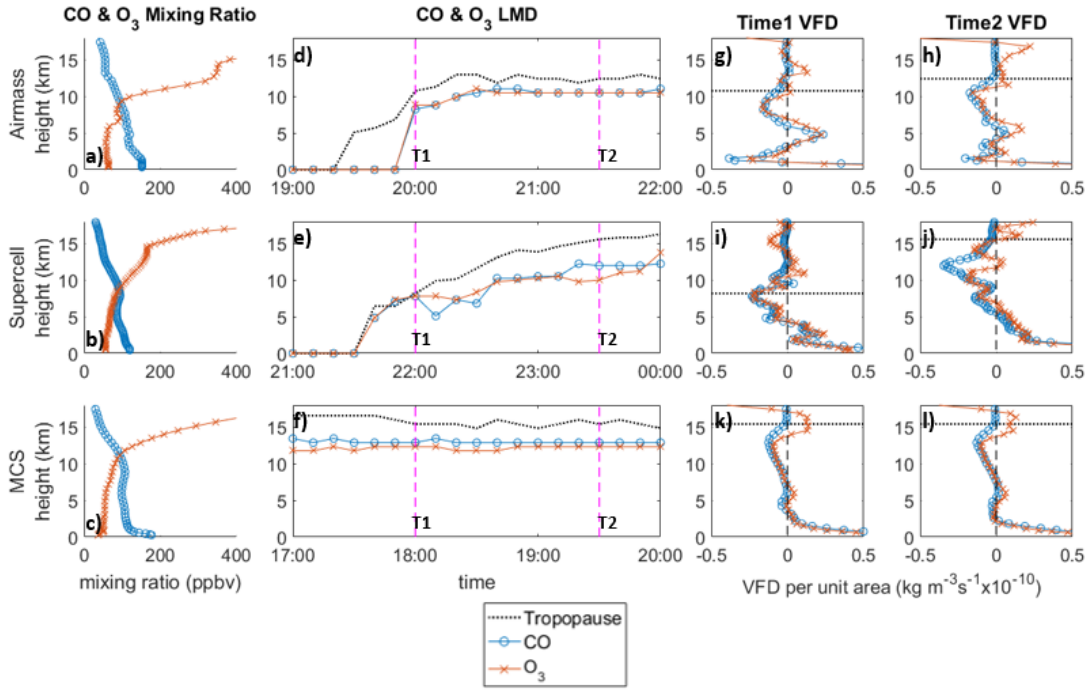

Figure 3.13 CO (blue) and O_3 (orange) initial mixing ratio vertical profile for (a) 21 May air mass case, (b) 29 May supercell case, and (c) 11 June MCS case. The WRF-Chem-LDA simulated LMD using CO and O_3 as example tracers for (d) 21 May air mass case, (e) 29 May supercell case, and (f) 11 June MCS case. The WRF-Chem-LDA simulated VFD per unit area at Time 1 (T1) and Time 2 (T2) using CO and O_3 as example tracers for (g and h) 21 May air mass case, (i and j) 29 May supercell case, and (k and l) 11 June MCS case are shown. The tropopause (shown by dotted line) is calculated based on the WMO definition.

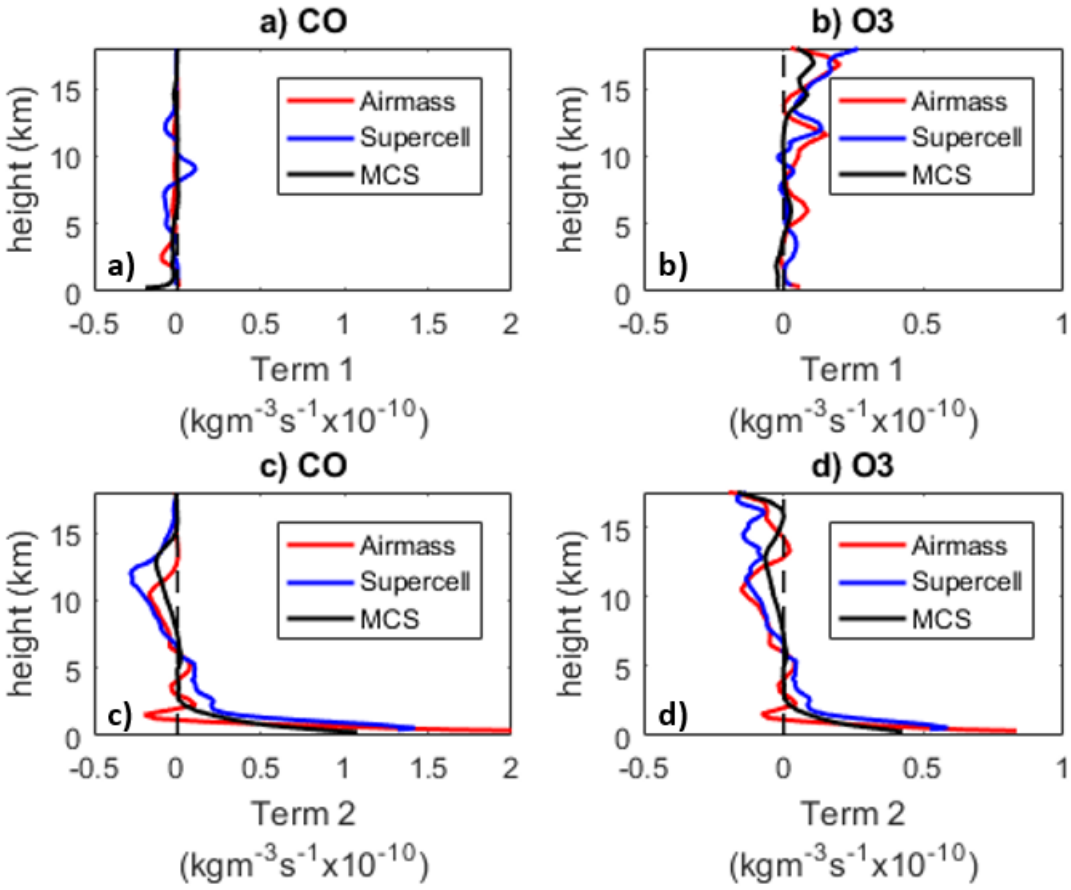

Figure 3.14 Trace gas gradient terms (the first term on the right side of equation (3.7)) for CO (a) and O3 (b) for the 21 May air mass case (red), the 29 May supercell case (blue), and the 11 June MCS case (black). Mass flux density gradient terms (the second term on the right side of equation (3.7)) for CO (c) and O3 (d) for same three cases.

3.3.5 Upward Vertical Transport Compared with Downward Vertical Transport

Besides upward transport, downward transport is also significant. In Figure 3.15, the VFD of upward transport, downward transport, and total (net) transport are compared side by side. CO vertical transport results show that in the mid and upper troposphere, net transport has the same sign as upward transport. This means that, within this altitude range, upward transport dominates vertical transport.

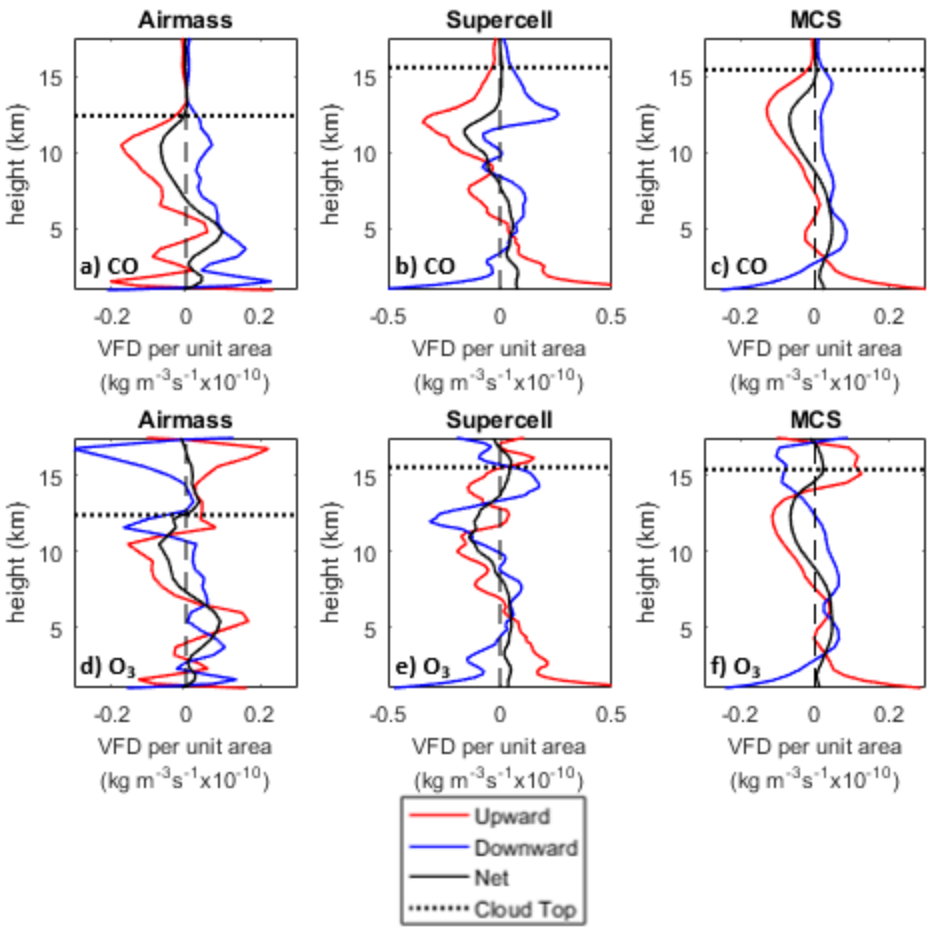

Figure 3.15 WRF-Chem-LDA simulated upward (red), downward (blue), and net (black) VFD per unit area using (a, b, c) CO and (d, e, f) O_3 as example tracers for the 21May air mass case, the 29 May supercell case, and the 11 June MCS case.

In the lower troposphere, either upward or downward transport may dominate. The vertical transport for O_3 at high levels remains, however, relatively more complex. Below the cloud top, defined here as the highest altitude where the sum of the mixing ratio of ice, snow, graupel, rain, and cloud exceeds 10^{-3} g kg^{-1}, there is a region where downward O_3 VFD is negative in all three cases. In this region, downward transport of high mixing ratio stratospheric O_3 causes O_3 convergence (negative net O_3 VFD). This model simulation result is similar to the observations. Huntrieser et al. (2016) analyzed

the in situ measurement of O_3 and reported that O_3-rich air from the LS was transported downward into the anvil and also surrounded the outflow. Pan et al. (2014) found that the wrapping of O_3-rich stratospheric air around the edge of the storm led to a ram-horn-shaped O_3 enhancement around the cloud edge reaching altitudes as low as 4 km below the local tropopause in the 30 May DC3 MCS case. Above the cloud top, there is a positive O_3 VFD region. In that region, the O_3 VFD divergence is caused by upward transport of low mixing ratio O_3 to the stratosphere.

3.3.6 Vertical Transport in Different Composite Reflectivity Regions

Sensitivity tests for vertical transport were simulated for different composite reflectivity regions. For each storm, the VFD per unit area and LMD were calculated every 10 minutes (Figure 3.16) within four composite reflectivity regions characterized by reflectivities exceeding 0 dBZ, 20 dBZ, 30 dBZ, and 40 dBZ. During the development stage of the 21 May airmass case and the 29 May supercell case, the heights of LMD vary between reflectivity regions, and the detrainment envelope is narrower in high reflectivity regions than in low reflectivity regions (at most 4 km narrower). After the storm matured, the heights of LMD and the detrainment envelope converge and become similar in all reflectivity regions. For the 11 June MCS case, the height of the LMD is insensitive to reflectivity region and varies little with time. In contrast to the airmass and supercell cases, the detrainment envelope for the MCS case is deeper in high reflectivity regions than in low reflectivity regions. The detrainment envelope for the region > 40 dBZ is 2 km thicker than the envelope for the region > 0 dBZ. Moreover, VFD analysis reveals that, for all three cases, VFD per unit area

remains stronger in the region > 40 dBZ region (storm core). Based on the analysis for these storm cases, the mean VFD per unit area in the region > 40 dBZ can be a factor 2-5 fold larger than the mean VFD in the region > 0 dBZ.

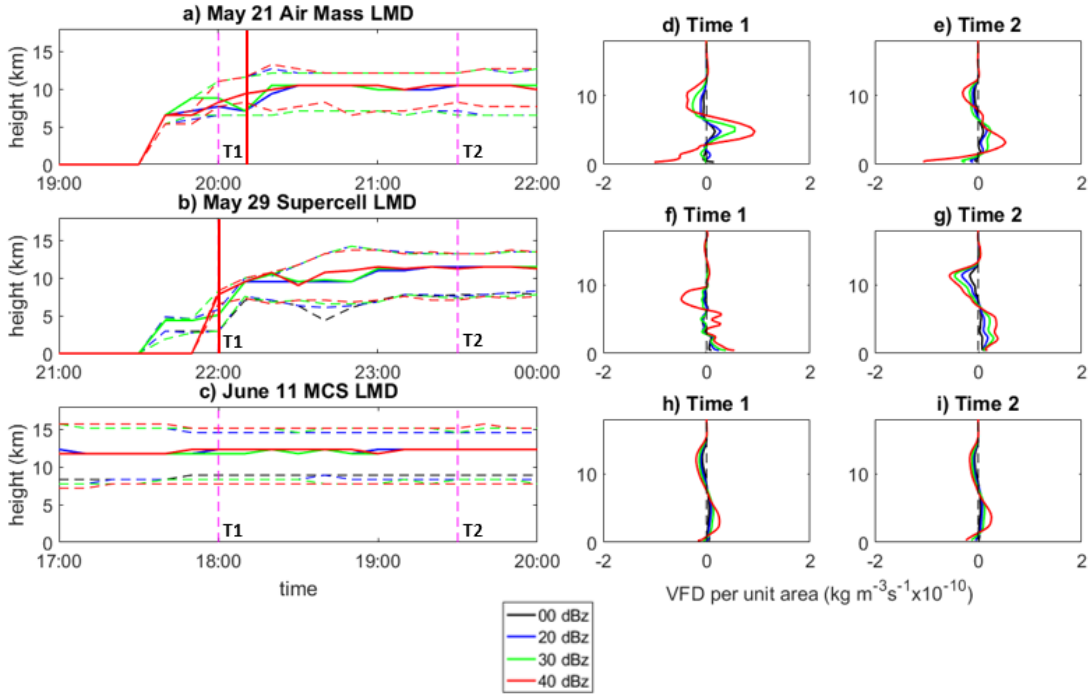

Figure 3.16 Time series of LMD from WRF-Chem simulations with LDA within four different reflectivity regions (exceeding: 00 dBZ (black), 20 dBZ (blue), 30 dBZ (green), and 40 dBZ (red), respectively) for (a) the 21 May air mass case, (b) the 29 May supercell case, and (c) the 11 June MCS case. The colored dashed lines represent the detrainment envelope of each reflectivity region. WRF-Chem-LDA simulated net VFD per unit area at Time 1 (T1) and Time 2 (T2) within different reflectivity regions for (d and e) the 21 May air mass case, (f and g) the 29 May supercell case, and (h and i) the 11 June MCS case. The vertical red lines in Figures 19a and 19b represent the time of anvil formation.

3.4 Summary

In this chapter, we analyze the deep convective transport in three different convective regimes from the DC3 field campaign using WRF-Chem simulations. After constraining the model solution via a computationally inexpensive lightning data

assimilation technique (Fierro et al. 2012, 2015), the model was able to better reproduce storm location, the timing of convection initiation, spatial structure and hence, the chemical distributions of interest. There was not a single set of model configuration and IC/BC that led to satisfactory simulations of all three cases. Each case required its own set of model specifications to obtain the best possible simulation.

The analysis of CO vertical transport demonstrated that the upward vertical flux divergence per unit area of the 29 May severe supercell case was the strongest, while the upward vertical flux divergence per unit area of the really expansive 11 June MCS case is comparable to that of the smaller 21 May airmass case. This result is in agreement with Bigelbach et al. (2014). For the airmass case, trajectories indicate that nearly all of the air parcels that originated below 1.5 km remained below 5 km, while air within the supercell and MCS systems was transported from near the surface to about 10 km in about 30 minutes.

Trace gas vertical cross-sections were examined and a tracer transport experiment was conducted to unveil some of the factors behind the simulated weak vertical transport of CO in the MCS case. The analysis revealed that a rear inflow jet transported relatively clean mid-level air into the downdraft region, which then descended and was entrained into the updraft region. This reduced trace gas mixing ratios in the low-level inflow and decreased the vertical gradient of trace gases, which contributed to the low VFD values.

We found that during storm development, the level of maximum detrainment became higher in altitude, and the depth of the detrainment envelope increased. Also, when analyzing two trace gases (CO and O_3) with different vertical profiles, it was found that the vertical flux divergence profiles of the two trace gases looked similar in the lower and mid troposphere, indicating that in this altitude range, the VFD profile is mostly controlled by the vertical distribution of mass flux density as opposed to the vertical distribution of the mixing ratio. In the upper troposphere, however, the CO and O_3 VFD profiles differed owing to strong O_3 gradients present at these levels. Comparing CO upward and downward transport, we found that upward transport dominates the vertical transport in the mid and upper troposphere. Nevertheless, the downward transport of stratospheric O_3 cannot be ignored. Sensitivity tests for vertical transport in different reflectivity regions show us that vertical transport remains stronger in the higher composite reflectivity region of the storms.

Chapter 4 : Evaluation of Parameterized Transport of Trace Gases

In this chapter, WRF-Chem is employed at cloud parameterized resolution (12 and 36 km) to simulate two different convective regimes that occurred during the DC3 field campaign: a severe supercell thunderstorm and an MCS case. The model at these resolutions was unable to reproduce the air mass storm simulated in Chapter 3. The purpose of the current chapter is to evaluate the model-simulated subgrid convective transport and redistribution of trace gases in these two convective regimes through comparisons with aircraft observations and finer resolution cloud-resolved simulations. To improve the model simulations, I prepared code to compute subgrid scale convective transport within the subgrid cumulus parameterization that performed the best in comparison with observed precipitation.

4.1 Model Setup

Table 4.1 WRF-Chem model configuration and physics and chemistry options.

	29 May Supercell	MCS
Meteorology IC/BC	*NAM-ANL starting from 18 UTC*	*GFS starting from 06 UTC*
Chemistry IC/BC	*MOZART scaled*	*MOZART scaled*
Grid resolution	*36 km, 12km*	
Vertical levels	*90*	
Time step	*120 s, 60 s*	
Cumulus scheme	*GF with KF closure*	*GF with all closure*
Microphysics	*Morrison*	
PBL	*MYJ*	*YSU*
Land surface	*Noah*	
Short/longwave radiation	*RRTMG*	
Chemistry option	*Chem_opt=13 (No chemical reaction, run with 5 tracers)*	
Subgrid trace gases transport	*Subgrid convective transport calculation within the GF cumulus scheme based on the GF mass flux*	

The WRF-Chem V3.9 containing the ARW dynamic core was utilized to simulate the aforementioned two cases. The detailed model configuration and physics and chemistry options for the two cases are listed in Table 4.1. Model outputs at 10 min intervals were used for the analysis.

4.1.1 Model Configuration, Initial and Boundary Conditions

For both cases, WRF-Chem model simulations were conducted on two domains at cloud-parameterized scales (36 km and 12 km horizontal grids, one way nested, two domains were run simultaneously). There were 90 vertical levels with a 50 hPa model top. The time steps for each domain were 120 s and 60 s, respectively.

We tried various IC and BC for both cases. The best simulation for the 29 May supercell case was initialized on 29 May at 1800 UTC using meteorological IC and BC derived from the 6 hourly 12 km NAM-ANL. These IC and BC are the same as used in the cloud-resolved simulation by Li et al. (2017). For the 11 June MCS case, the best simulation was initialized on 11 June at 0600 UTC using IC and BC derived from the 6 hourly GFS. Model output from MOZART-4 was used to generate the chemical IC and BC for both cases. However, for the 29 May supercell case, the MOZART CO mixing ratios were larger than aircraft observations, especially in the PBL. So, we use the following equation to tune the 1-15 km CO IC, where the unit of CO is parts per billion volume (ppbv), and the unit of height is kilometers (km).

$$\mathrm{CO}_{\mathrm{MOZART\ Scaled}} = \frac{85 + \mathrm{Height}}{100} \times \mathrm{CO}_{\mathrm{MOZART}} \tag{4.1}$$

For the 11 June MCS case, the MOZART CO mixing ratios were lower than aircraft observations. Therefore, the following equation was used to tune the 1-9 km CO IC.

$$\mathrm{CO}_{\mathrm{MOZART\ Scaled}} = \frac{109 - \mathrm{Height}}{100} \times \mathrm{CO}_{\mathrm{MOZART}} \tag{4.2}$$

After tuning the CO IC, the observed inflow CO mixing ratio was reproduced well in all the simulations. The WRF-Chem simulated low-level inflow CO mixing ratios were evaluated against aircraft measurements. For both cases, the simulations of CO mixing ratios in low-level inflow were within 5 % of the aircraft measurements (Table 4.2).

Table 4.2 WRF-Chem simulated low-level inflow CO mixing ratios compared with aircraft measurements for 29 May supercell case and 11 June MCS case.

	29 May Supercell	11 June MCS
Aircraft measurements	132.3 ± 3.1	117.5 ± 4.3
WRF-Chem 1km	136.3 ± 0.3	112 ± 7.8
WRF-Chem 12km	131.3 ± 0.7	119.4 ± 3.9
WRF-Chem 36km	131.7 ± 0.8	115.3 ± 3.8

4.1.2 Cumulus Parameterization

The cloud parameterizing WRF results were highly dependent on the choice of cumulus schemes, especially for the 29 May supercell case. In order to find the best-performing cumulus scheme for these storms, we tried five commonly used cumulus parameterization options in WRF: (1) Kain-Fritsch (KF) scheme (Kain, 2004), which uses a mass flux approach with downdrafts and CAPE removal time scale; (2) Betts-Miller-Janjic (BMJ) scheme (Janjic, 1994), a scheme which relaxes the column

moisture profile towards a well-mixed profile; (3) Grell-Freitas (GF) scheme (Grell & Freitas, 2014), which is a scale scheme based on the Grell-Devenyi (GD) scheme (details in section 4.4); (4) Grell-3D (G3D) scheme (Grell, 1993; Grell & Devenyi, 2002), which is an improved version of the GD scheme (a multi-closure, multi-parameter, ensemble method) that may also be used on high resolution; and (5) Tiedtke scheme (Tiedtke, 1989; Zhang et al., 2011), which is a mass flux type scheme with CAPE-removal time scale, shallow component and momentum transport.

4.1.3 Other Physics Options

The PBL option was Mellor-Yamada-Janjic (MYJ) scheme (Janjic, 1994) for the 29 May supercell case, and YSU scheme (Hong et al., 2006) for the 11 June MCS case. For both cases, the other main physics choices were the two-moment Morrison microphysics (Morrison et al., 2009) for microphysical processes, the RRTMG scheme (Iacono et al., 2008) for longwave and shortwave radiation, and the Noah scheme (Koren et al., 1999) for land surface processes.

4.1.4 Preliminary Precipitation Results

Figure 4.1 shows the precipitation during the three-hour period after CI was observed (observation: 2100-0000 UTC; KF: 1850-2150 UTC; BMJ: 2220-0120 UTC; GF: 2220-0120 UTC; G3D: 2040-2340 UTC; Tiedtke: 2300-0200 UTC) for the 29 May supercell case. National Centers for Environmental Prediction (NCEP) Stage IV precipitation observations interpolated to the 36 km grid are compared with results from model simulations using the five cumulus parameterizations discussed in section

4.1.2. The observations show a two cell structure with precipitation maxima in excess of 10 mm. The KF scheme did not reproduce the two cell structure of the observed storm. The BMJ and G3D schemes underestimated the precipitation maxima. Although the Tiedtke scheme captured the two cell structure of the storm and the maximum precipitation was close to observations, the simulated precipitation region was too small. Compared with the other results, the model simulation of the 3-hour precipitation location and strength were the best when using the GF scheme.

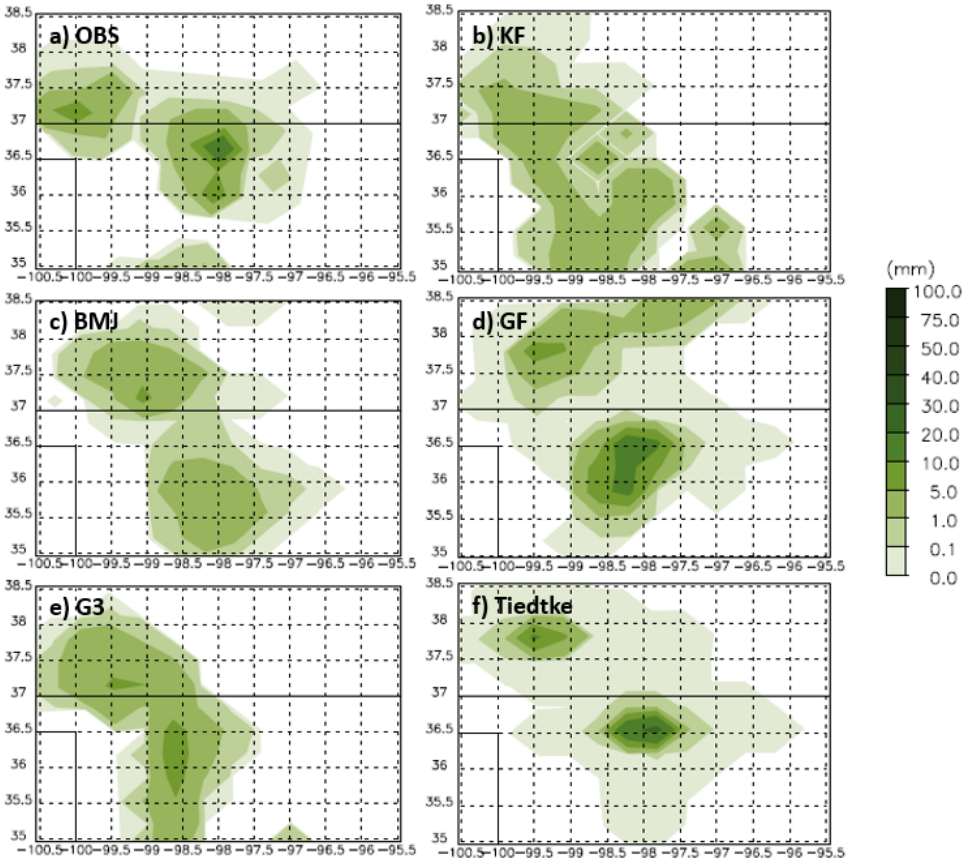

Figure 4.1 3-hour precipitation (mm) at 36 km resolution from the start of the convection for observation (2100-0000 UTC, a), WRF-Chem with KF cumulus scheme (1850-2150 UTC, b), BMJ cumulus scheme (2220-0120 UTC, c), GF cumulus scheme (2220-0120 UTC, d), G3 cumulus scheme (2040-2340 UTC, e), and Tiedtke cumulus scheme (2300-0200 UTC, f).

Although the 3-hour total precipitation of the GF simulation well matched the observation, the 1 hour maximum precipitation at the aircraft measuring time (3 hours after CI) was ~36.5% lower than the observation. In order to improve the maximum 1-hour precipitation simulation for the 29 May supercell case, we tried tuning the closure options inside the GF scheme following Qiao and Liang (2015, 2016, and 2017) who examined the effects of major cumulus parameterization closures on simulation of summer precipitation. They found that closure algorithms largely affect precipitation's geographic distribution, frequency and intensity, and diurnal cycle, with strong regional dependence. There are four major groups of closure assumptions used in the original GF scheme: the quasi-equilibrium based (AS) closure, the vertical velocity (W) closure, the total instability adjustment (KF) closure, and the moisture convergence (MC) closure. The AS closure (Arakawa and Schubert, 1974) determines the cloud base mass flux (CBMF) by adjusting the cloud work function towards a climatological value to maintain instantaneous equilibrium between large-scale forcing and subgrid convection. The W closure (Brown, 1979; Frank & Cohen, 1987) calculates the CBMF using the environmental vertical velocity at lower tropospheric levels. In the MC closure (Krishnamurti et al., 1983), the calculation of the CBMF is based on moisture convergence. In the KF closure (Kain & Fritsch, 1993), the calculation of the CBMF is based on the assumption that the CAPE is simply removed by the convection over a specific time period. The original GF scheme uses an average CBMF from the results of the above closures.

We re-ran the WRF simulation four times with only one closure turned on at each time. Then we compared the observed and simulated first 3 hours maximum hourly precipitation, as the majority of convective transport is in the high precipitation region (Li et al., 2017). The results are listed in Table 4.3. The maximum hourly precipitation simulation with the KF closure perfectly matched the observed maximum hourly precipitation (the difference is within 5% of the observation). Therefore, we regarded the KF closure simulation as the best result, and our following analysis of the 29 May supercell case was based on this simulation. For the 11 June MCS case, the simulation with the original GF scheme performed well. Therefore, we did not test the performance of using different closures for this case, and the results in Section 5 use the normal GF scheme.

Table 4.3 The observation and WRF-Chem simulations of the maximum precipitation (mm) per hour for 29 May supercell case at 1 to 3 hours after CI.

	1 hour after CI	2 hour after CI	3 hour after CI
OBS	*1.84*	*4.53*	*16.87*
WRF-Chem with All 4 closures in GF	*3.83*	*6.17*	*10.71*
WRF-Chem with AS closure in GF	*3.28*	*5.42*	*14.68*
WRF-Chem with W closure in GF	*3.57*	*6.26*	*12.44*
WRF-Chem with MC closure in GF	*3.62*	*6.28*	*10.64*
WRF-Chem with KF closure in GF	*2.00*	*4.38*	*16.03*

4.1.5 Chemistry Option ad Subgrid Convective Transport Option

The chemistry option for both cases was option 13 (no chemical reaction, run with 5 tracers). Within WRF-Chem a routine separate from the transport of water vapor in WRF is used to calculate the fluxes for the chemical species and tracers. The default subgrid convective transport scheme inside the WRF-Chem is based on the GD

convection scheme, which is not consistent with our WRF-Chem simulation with GF cumulus scheme. Therefore, we rewrote the subgrid convective tracer transport routine within the GF scheme. The mass flux related variables (i.e. entrainment and detrainment rate, cloud top height, CBMF, downdraft mass flux, updraft mass flux, the originating level of updraft and downdraft, level of free convection, evaporation, and precipitation) from GF scheme were used to calculate the subgrid convective transport of trace gases in the new routine using the following equation (Grell & Freitas, 2014):

$$\left(\frac{\partial C}{\partial t}\right)_{subgrid} = -\frac{1}{\rho}\frac{\partial}{\partial z}\left[m_u(C_u - C_e) - m_d(C_d - C_e) + m_u C_{aq}\right] - \overline{C_{si}} + \overline{C_{so}} \quad (4.3)$$

where C represents the mass mixing ratio of CO, ρ represents air density, m represents massflux. The subscripts e, u, and d represent the environment, updraft, and downdraft, respectively. C_{aq} represents the chemical constituent in the aqueous phase, C_{so} is calculated using an aqueous phase chemistry routine (source), and C_{si} depends on the conversion rate of cloud water to rain water and the solubility of the tracer (sink). In this paper, we focus on the convective transport of an insoluble trace gas (CO). Thus, equation 4.3 can be simplified to:

$$\left(\frac{\partial C}{\partial t}\right)_{subgrid} = -\frac{1}{\rho}\frac{\partial}{\partial z}\left[m_u(C_u - C_e) - m_d(C_d - C_e)\right] \quad (4.4)$$

The GF scheme is based on the older GD scheme with several improvements. Firstly, to increase diurnal forcing, temperature and moisture perturbations are added when calculating the diurnal forcing and checking for trigger function. Moreover, in the GD scheme, the normalized mass flux at the initial level is 1 for both updraft and downdraft; however, in the GF scheme, for the updraft, the normalized mass flux

approaches the value of 1 quadratically from the initial level to the level of free convection, and for the downdraft, a similar smooth increase is prescribed for the first 5 levels. In addition, in the GD scheme, the non-resolved flux for one ensemble member is based on the CBMF of that ensemble member, while in the GF scheme, the non-resolved flux for one ensemble member is based on the average CBMF of all the ensemble members. Although not employed in the current analysis, the GF scheme is capable of representing aerosol cloud interaction (Grell & Freitas, 2014).

4.2 Meteorology Results

For the 29 May supercell case, the model with GF subgrid convection with KF closure (GF-KF run) produced a storm that began 80 min (for 36 km domain) and 30 min (for 12 km domain) later than observed. Because the 12 km convection started earlier, the 36 km parameterized convection did not affect the initiation of convection at 12 km. The 3-hour precipitation observation at 0000 UTC and model simulation at 0120 UTC (for 36 km domain) and at 0030 UTC (for 12 km domain) on May 30 are compared in Figure 4.2. Both the 36 km and 12 km WRF-Chem simulations capture the storm location, precipitation strength, and the two cells structure of the storm. Comparison of the middle 4 panels (Figures 4.2c, d, e, and f) indicates that the precipitation for the 36-km resolution simulation is mainly subgrid scale (subgrid scale mean precipitation is 3 times greater than grid scale mean precipitation), while the precipitation for the 12-km resolution simulation is mainly grid scale (grid scale mean precipitation is 2.7 times greater than subgrid scale mean precipitation). Therefore, in

the 36 km run, subgrid scale convection dominates, while in the 12 km run, grid scale convection dominates.

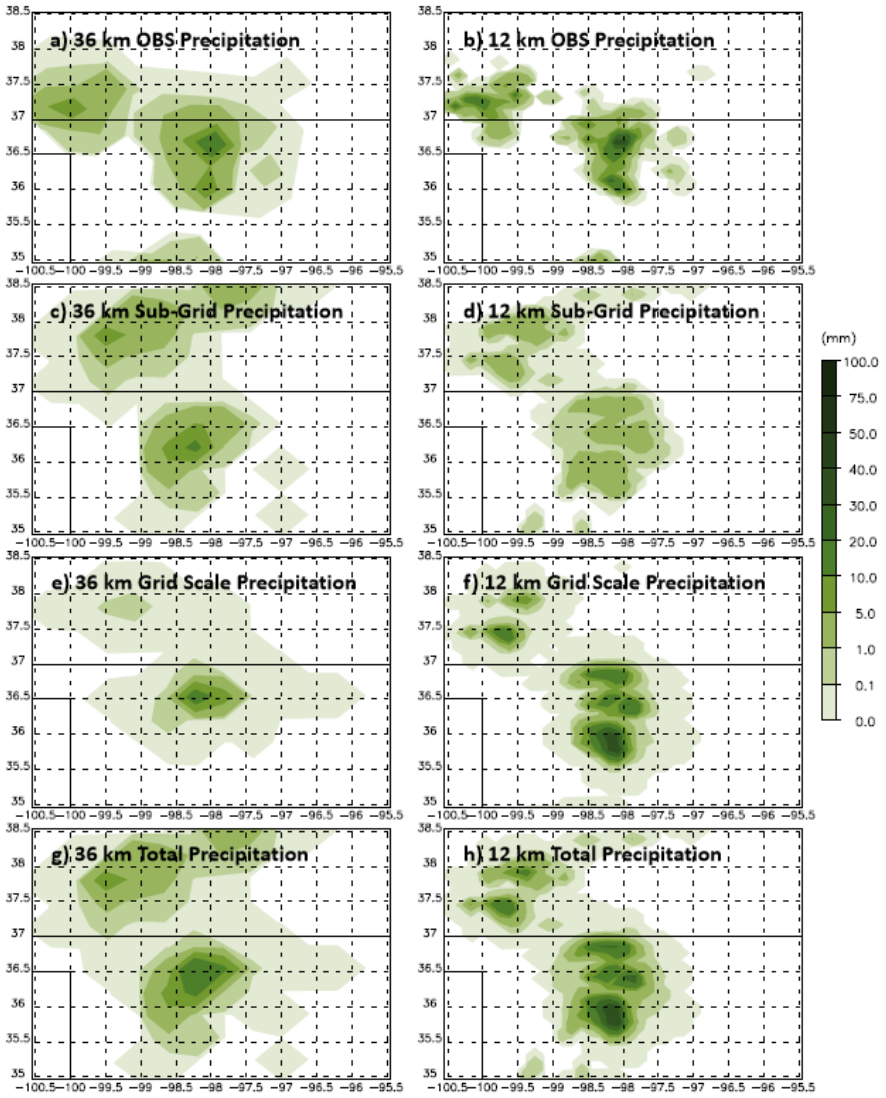

Figure 4.2 3-hour Precipitation observation (mm) interpolated to 36 km (a) grid and 12 km (b) grid from 2100 UTC 29 May to 0000 UTC 30 May, 2012; WRF-Chem simulated 36 km subgrid scale (c), grid scale(e), and total precipitation (g) at 0120 UTC on May 30, 2012; WRF-Chem simulated 12 km subgrid scale (d), grid scale(f), and total precipitation (h) at 0030 UTC on May 30, 2012.

The precipitation results with the GF scheme and the standard closure procedure for the 11 June MCS case are shown in Figure 4.3. Both 36 km and 12 km WRF-Chem

simulations capture the storm location and the strong precipitation region. In the 12 km simulation, the precipitation amount (Figure 4.3h) is larger than the observation, which is caused by the overestimate of the grid scale precipitation in the microphysics processes (Figure 4.3f). Also, in the 36 km run, subgrid scale convection dominates (subgrid scale mean precipitation is 3.5 times greater than grid scale mean precipitation), and in the 12 km run, grid and subgrid scale convection make similar contributions (grid scale mean precipitation is 1.1 times greater than subgrid scale mean precipitation). The precipitation rate simulations in the storm core region is within 10% of the observation. In the rear of the storm, the area of the weak precipitation region in both the 36 km and 12 km simulation is larger than in the observations. However, this will not have much influence on our convective transport analysis, as the majority of convective transport occurred in the storm core region after storm become mature. In section 3.3.4 I found that after the storm became mature, the convective transport in the storm core region, where composite reflectivity was higher than 40 dBZ, was a factor of 2-5 larger than the convective transport outside the core region.

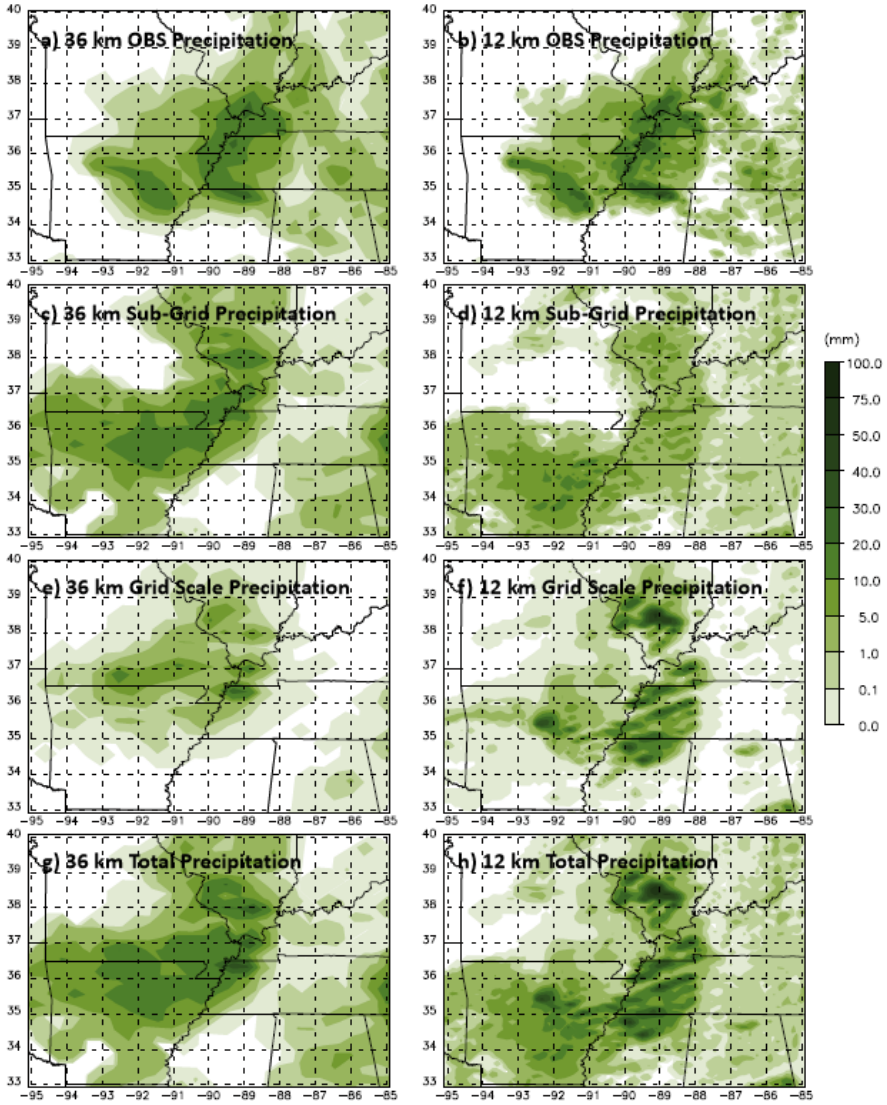

Figure 4.3 Similar to Figure 4.2 but from 1900 to 2200 UTC on 11 June, 2012 for both observation and WRF-Chem simulation.

4.3 Deep Convective Transport Results

4.3.1 Evaluation of the Convective Transport Simulation

We compared the convective transport between the cloud parameterized and cloud resolved simulations through a comparison of observed and simulated high level outflow CO mixing ratios. The cloud resolved simulations we use here for the 29 May

supercell and the 11 June MCS are described in Bela et al. (2016a) and Li et al. (2017), respectively, as well as the model set up and evaluation.

In order to better evaluate the influence of the subgrid scale convection on the outflow CO mixing ratio, we conducted three sensitivity test runs for the cloud parameterized simulation: (1) using our new GF subgrid scale convective transport scheme (hereafter GFCT scheme); (2) using the original WRF-Chem GD subgrid scale convective transport scheme (hereafter GDCT scheme); (3) no subgrid convective transport (hereafter NoCT). For the 29 May case, both the DC-8 (Figure 4.4) and GV (Figure 4.5) measured storm outflow. The DC-8 measured storm outflow at ~ 10.8 km (average GPS height), at the same time, the GV measured storm outflow at ~ 11.7 km (average GPS height). For the 11 June case (Figure 4.6), the storm outflow region was only measured by the GV at an altitude of about 13 km. In each of the figures the outflow CO aircraft measurements are plotted on the CO simulation field at the aircraft flight altitude.

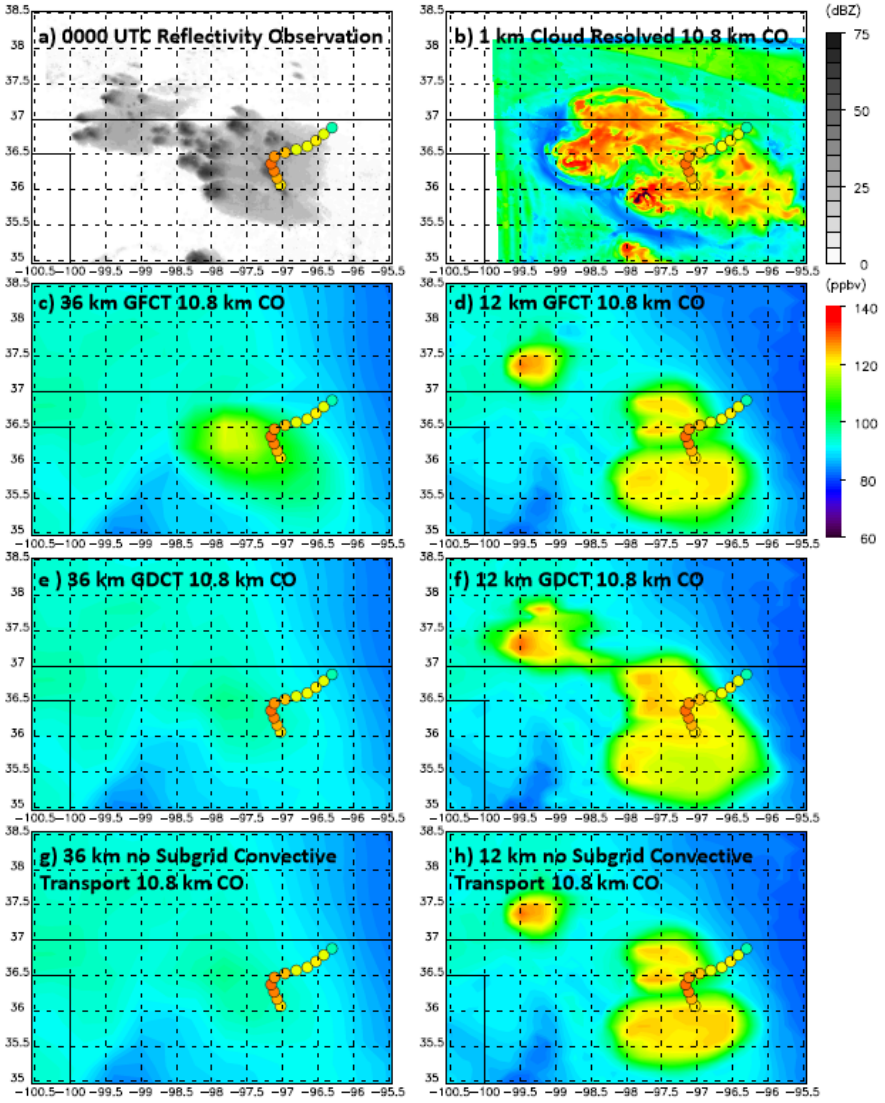

Figure 4.4 DC-8 measured outflow CO mixing ratio in ppbv at ~ 10.8 km altitude between 2348 UTC and 2358 UTC on 29 May, 2012 (colored dots). Background shading shows 0000 UTC NEXRAD composite reflectivity (dBZ) (a). Background colors show 0040 UTC 1 km cloud resolved simulation of 10.8 km CO mixing ratio (b), 0120 UTC 36 km cloud parameterized simulation of 10.8 km CO mixing ratio with GFCT (c), GDCT (e), and without subgrid convective transport (g); 0030 UTC 12 km cloud parameterized simulation of 10.8 km CO mixing ratio with GFCT (d), GDCT (f), and without subgrid convective transport (g).

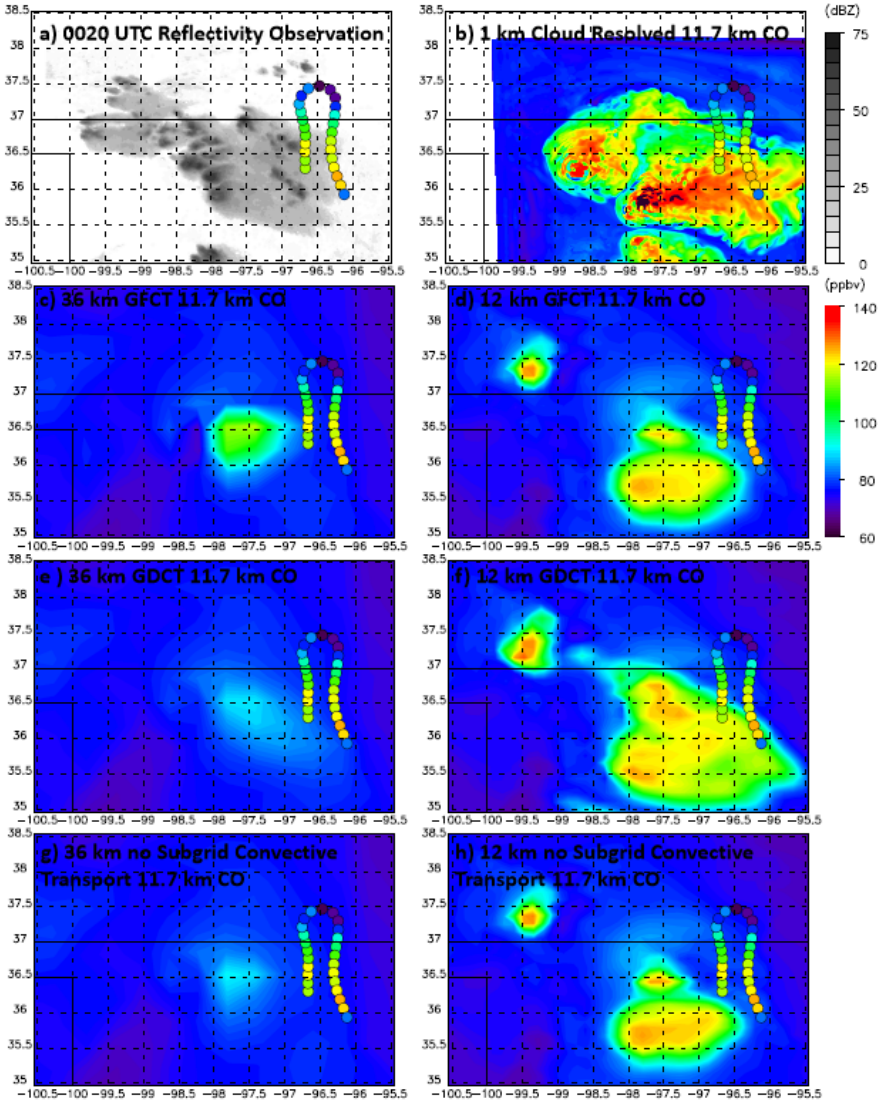

Figure 4.5 Similar to Figure 4.4 but for GV measured at 11.7 km between 0000 UTC and 0023 UTC on May 30, 2012 (colored dots); the NEXRAD data was at 0020 UTC, the cloud resolved simulation result sampled at 0100 UTC, the 36 km simulations sampled at 0140 UTC, the 12 km simulations sampled at 0050 UTC.

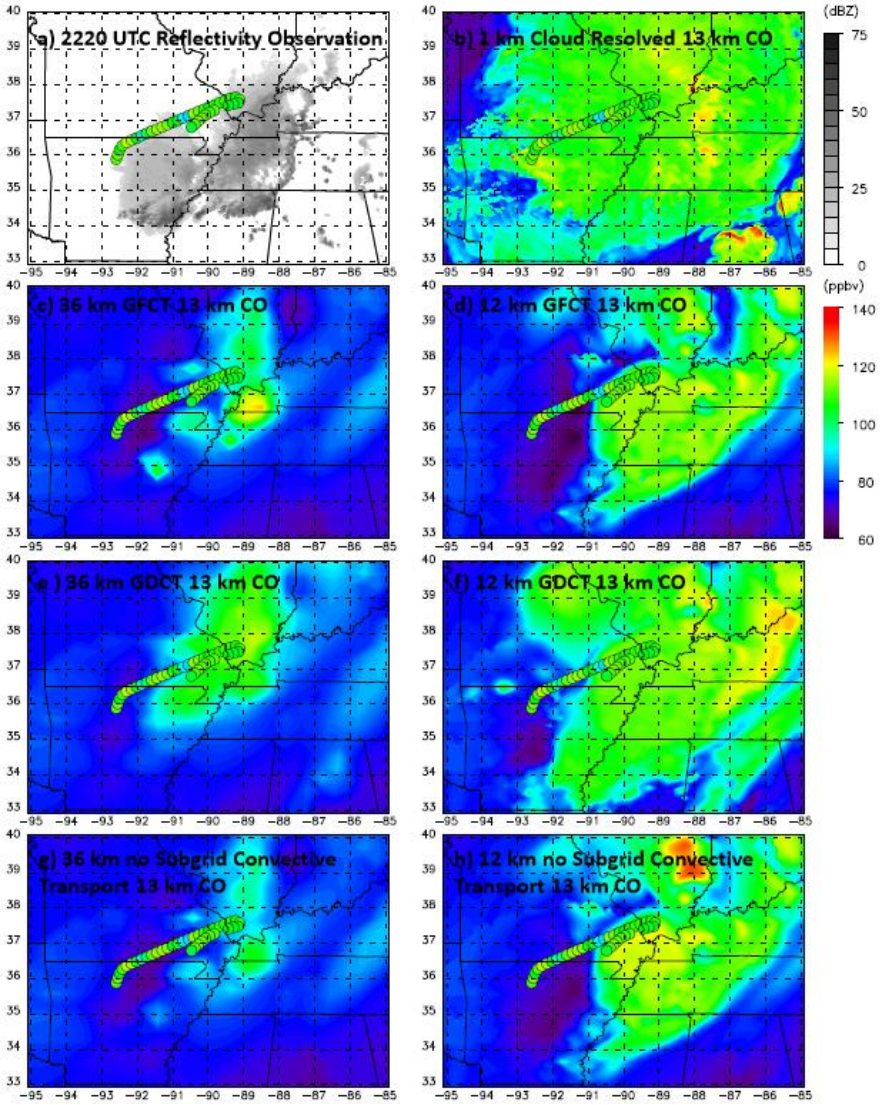

Figure 4.6 Similar to Figure 4.4 but for GV measured at 13 km between 2200 UTC and 2237 UTC on 11 June, 2012 (colored dots); the NEXRAD reflectivity, cloud resolved and parameterized simulation results sampled at 2220 UTC.

The comparison of the three simulations indicated that the application of the GFCT scheme improved the model simulation of the high level outflow CO, especially for the 36 km runs. In Figure 4.4, in the 36 km domain, both the GDCT run and the NoCT run failed to simulate the increase of CO associated with the outflow. Specifically, the GFCT simulated outflow CO mixing ratio at 10.8 km was on average

approximately 18 ppbv (18.5 %) larger than GDCT and NoCT results, but still 4 ppbv less than the aircraft measured anvil CO mixing ratio at the same altitude. In Figure 4.5, on the 11.7 km level, use of GFCT increased the 36 km domain outflow CO mixing ratio by 15 ppbv (17.6%) compared to GDCT and NoCT, but the resulting outflow was still 17 ppbv lower than the observed outflow. For the 11 June MCS case, all three 36 km runs simulated the CO increase in the outflow region (Figure 4.6). Nevertheless, only the GFCT reproduced the high CO mixing ratio (> 125 ppbv) in the storm core region which was seen in the cloud resolved run, which was 20% higher than NoCT and GDCT runs. Although the GFCT scheme improved the outflow CO simulation, 36 km cloud parameterized CO mixing ratios were still smaller than the aircraft observations and cloud resolved CO mixing ratios, and the cloud parameterized CO outflow region was smaller in area than observed and simulated by the cloud resolved model. We tried to tune the 36-km entrainment profile to match observations (Fried et al., 2016) and the cloud-resolved simulation (Bela et al., 2018, under review), but had little success. In the 12 km runs, the CO mixing ratio results from the three cloud parameterized runs looked similar. This is because the 12 km convection simulation was dominated by the grid scale convection as discussed in section 5.1. For the 29 May supercell case, the 12 km simulated CO outflow region was still smaller than aircraft observations but was much larger than the 36 km outflow region.

Vertical profiles of in-cloud CO at the locations of observed and modeled upper-level cloud outflow are shown in Figures 4.7-4.8. For the 29 May supercell case, the anvil associated with the simulated storm with GF parameterized convection

(Figure 4.4c, d and Figure 4.5c, d) is smaller than the observed (Figure 4.4a and Figure 4.5a) and cloud-resolved anvils (Figure 4.4b and Figure 4.5b). Therefore, the location of the model profile is shifted by 0.75 degrees to sample the maximum of model outflow. The in-cloud points are defined as where the total liquid and ice mixing ratio is greater than 0.01 g/kg or the altitude is lower than the cloud top. In all the three 36 km runs, the mid-level CO mixing ratio increased; however, only the GFCT run reproduced the CO mixing ratio peak in the UT, which suggested that the convective transport in the GFCT scheme transports the PBL CO to the UT more effectively. Unlike the result of 36 km domain, the CO outflow mixing ratio simulation in the 12 km domain matched the observation well. The differences among the three runs (GFCT, GDCT, and NoCT) are small, which is because the grid scale convective transport rather than the subgrid scale transport dominates in the 12 km runs.

In the 36 km results of the 11 June MCS case (Figure 4.8), the GDCT result was close to the result of NoCT. The GFCT simulated UT CO mixing ratio (8-13 km) was larger than the other two runs, but the increase was not as apparent as the increase in the 29 May supercell case. This implied that the subgrid convective transport was more significant in the supercell case than the MCS case. In the lower troposphere, both GFCT (8% lower) and GDCT (13% lower) simulated CO mixing ratios were smaller than the NoCT result. This result is because in the downdraft region of the MCS, there was an injection of relatively clean mid-level clean air to the storm downdraft, when then descended to the lower troposphere and decreased the CO mixing ratio in this region. This is also found in the cloud resolved results (Li et al., 2017). In

the cloud resolved runs, the CO mixing ratio in the region affected by this kind of injection was ~16% smaller than in the unaffected region.

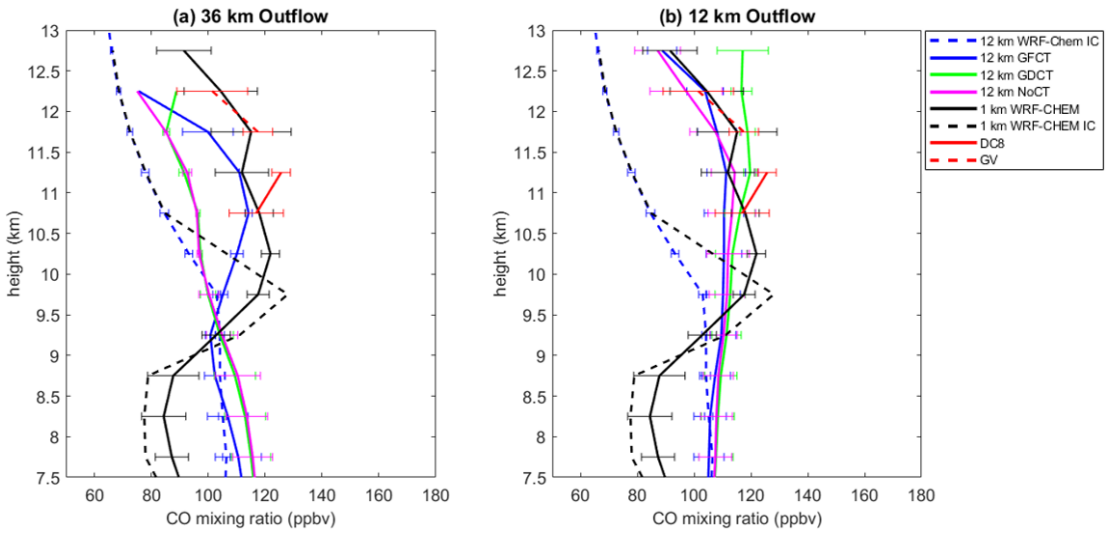

Figure 4.7 Mean outflow CO profiles from the 29 May supercell storm as observed by the DC-8 (red solid line) and GV (red dash line) aircraft, mean profiles as simulated in the 36 km (a) and 12 km (b) resolution WRF-Chem run with GFCT (blue), GDCT (green), NoCT (magenta), and mean profiles as simulated in the 1 km cloud-resolved WRF-Chem run (black), compared with the IC for cloud parameterized run (blue dash) and cloud resolved run (black dash). Model profiles shifted in horizontal with respect to the aircraft profiles by 0.75 degrees to ensure sampling of model outflow. Bela et al. (2016a) used DC8 measurements to create a horizontally homogeneous IC for CO in a limited domain cloud-resolved model. Since our cloud parameterized domain was much larger than Bela et al. (2016), we used MOZART to create the IC for our 36 km and 12 km runs.

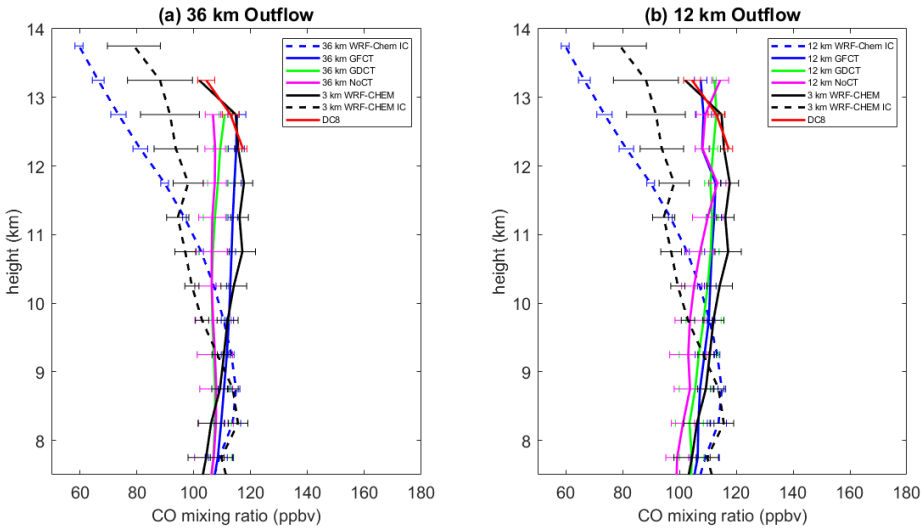

Figure 4.8 Mean outflow CO profiles from the 11 June MCS case as observed by the DC-8 (red solid line) aircraft, mean profiles as simulated in the 36 km (a) and 12 km (b) resolution WRF-Chem run with GFCT (blue), GDCT (green), NoCT (magenta), and mean profiles as simulated in the 1 km cloud-resolved WRF-Chem run (black), compared with the IC for cloud parameterized run (blue dash) and cloud resolved run (black dash) based on the model output along the aircraft sampling track.

4.3.2 Comparison of Subgrid Convective Transport and Turbulent Mixing

We also investigated whether vertical turbulent mixing affects the convective transport of PBL CO to the upper-levels. In order to contrast the influence of vertical turbulent mixing and subgrid convective transport on the CO vertical profile, we conducted 4 sensitivity runs: (1) GFCT with turbulent mixing (vertmix_onoff=1), (2) GFCT without turbulent mixing (vertmix_onoff=0), (3) NoCT with turbulent mixing, (4) NoCT without turbulent mixing. Turning vertical turbulent mixing off in this manner did not affect the meteorological simulation. Results showed that the difference between turning on and turning off turbulent mixing was negligible, in the mid troposphere and UT, particularly in the supercell case. In the lower troposphere (under 2 km), the difference between turning on and off vertical mixing was significant but not particularly large (5% for 29 May supercell case, and 13% for 11 June MCS

case). Without turbulent mixing the vertical gradient of the low-level CO mixing ratio was larger.

4.3.3 Comparison of Subgrid Scale and Grid Scale Convective Transport

We compared the subgrid and grid scale convective transport by analyzing the CO tendency in the convective region due to convective transport. The CO tendency due to subgrid scale convective transport is calculated using equation 4.4, and the CO tendency due to grid scale convective transport is calculated using the following equation:

$$\left(\frac{\partial \mathrm{C}}{\partial \mathrm{t}}\right)_{\mathrm{grid}} = \left[\left(\mathrm{advh}_{\mathrm{co}_{t+1}} + \mathrm{advz}_{\mathrm{co}_{t+1}}\right) - \left(\mathrm{advh}_{\mathrm{co}_{t}} + \mathrm{advz}_{\mathrm{co}_{t}}\right)\right]/\mathrm{dt} \qquad (4.5)$$

where advz_co and advh_co are the grid scale accumulated vertical tendency and accumulated horizontal tendency for CO. We calculated the CO tendency for two regions: where the precipitation rate was > 0 mm/hr and where the precipitation rate was > 3 mm/hr. The > 0 mm/hr results provide us information on convective transport from the beginning of the storm to the end of the simulation, especially at the start of the storm when the precipitation was not strong. Comparing the > 0 mm/hr results with the > 3 mm/hr results enables us to see the relationship between convective transport and the precipitation rate.

The CO tendency results for the 29 May supercell case are shown in Figures 4.9 (averaged over the precipitation rate > 0 mm/hr region) and 4.10 (averaged over the precipitation rate > 3 mm/hr region). In both grid and subgrid scale, the convective transport tended to increase the CO mixing ratio at the cloud top. As the storm started

to develop, the CO detrainment layer at the storm top increased in height. In Figure 10, the subgrid scale convective transport started earlier than the grid scale convective transport in both the 12 km and 36 km domains. The subgrid scale convective transport reached its maximum when the grid scale convection started to form a continuous constant-altitude detrainment layer in the UT at around 0300 UTC in the 36 km domain and about 0000 UTC in the 12 km domain. After that time, the subgrid scale convective transport began to decay. The grid scale convective transport of CO at the beginning of the storm was also stronger than when the storm became mature. Comparing Figure 4.10, with Figure 4.9, the average grid and subgrid scale CO tendencies in the region with the precipitation rate greater than 3 mm/hr were much stronger than the average CO tendency in the > 0 mm/hr precipitation rate region, which proves that both grid scale and subgrid scale transport are stronger in the heavier precipitation region.

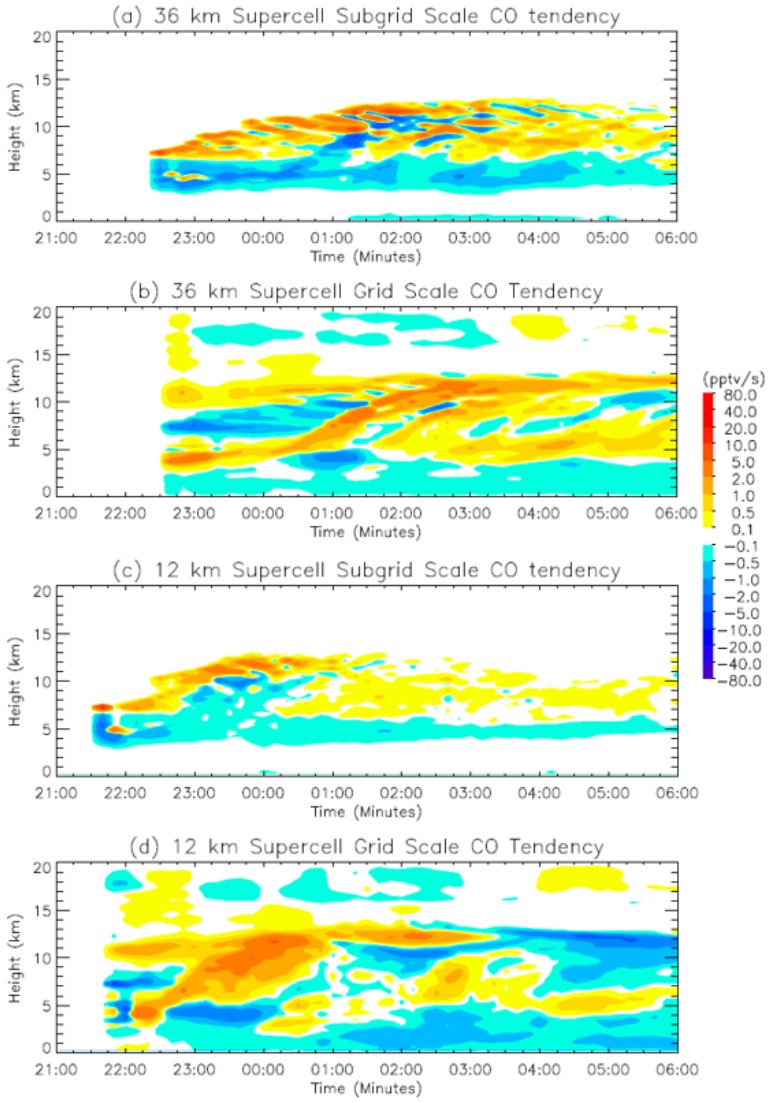

Figure 4.9 Subgrid scale CO tendency (pptv/s) for the 29 May supercell case at 36 km (a) and 12 km (c) horizontal resolution domain, and grid scale CO tendency (pptv/s) at 36 km (c) and 12 km (d) horizontal resolution domain.

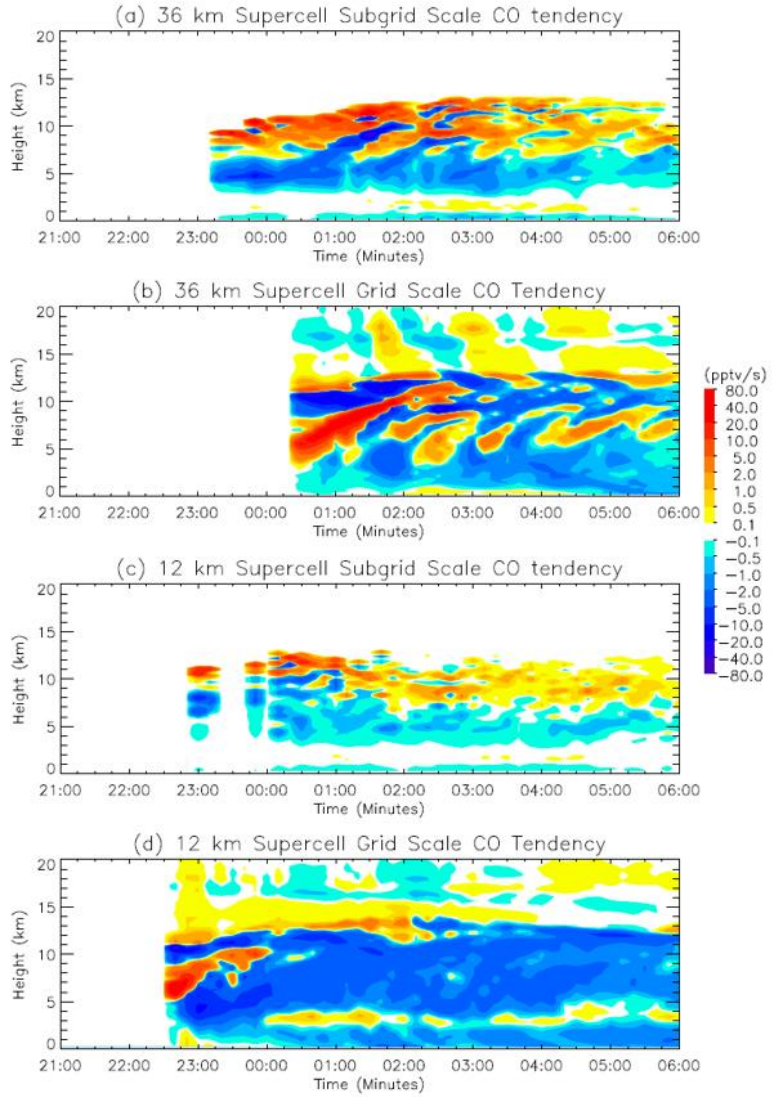

Figure 4.10 Similar to Figure 10 but for the region where precipitation was greater than 3 mm/hr.

The CO tendency results for the 11 June MCS case are shown in Figure 4.11-4.12. Compared to the 29 May supercell results, the CO tendencies due to both subgrid and grid scale convection in the > 0 mm/hr precipitation region were smaller, especially for the 12 km resolution. The magnitude of CO tendency in the stronger precipitation region (> 3 mm/hr) was comparable to the 29 May supercell results. Similar to the supercell case, both grid and subgrid scale CO tendencies in the MCS case were

strongest when the continuous constant-altitude detrainment layer began (1400 UTC). After that time, when the storm moved southeastward to the Kentucky and Tennessee region, the mean upper-level CO tendency due to grid and subgrid scale convection was very weak. Furthermore, unlike the results in the supercell case, the grid scale transport occurred nearly at the same time with the subgrid scale convective transport. This is because in the supercell case, the grid spacing is too coarse to resolve the strength of the convergence at the beginning of the storm. Therefore, the parameterization has to initiate and maintain the convection until the resolved-scale can respond to the redistribution of water and heat. While, in the MCS case, the convergence occurred over a large enough spatial scale to be resolved in the grid scale at the start of the storm.

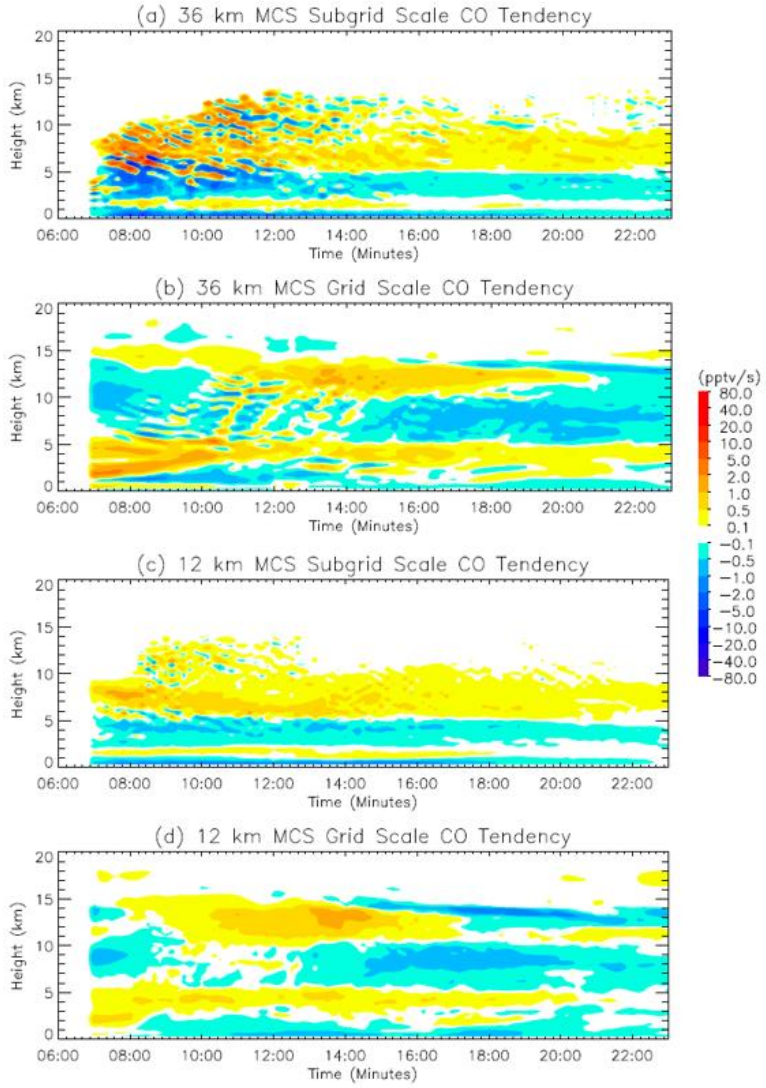

Figure 4.11 Subgrid scale CO tendency (pptv/s) for the 11 June MCS case at 36 km (a) and 12 km (c) horizontal resolution domain, and grid scale CO tendency (pptv/s) at 36 km (c) and 12 km (d) horizontal resolution domain.

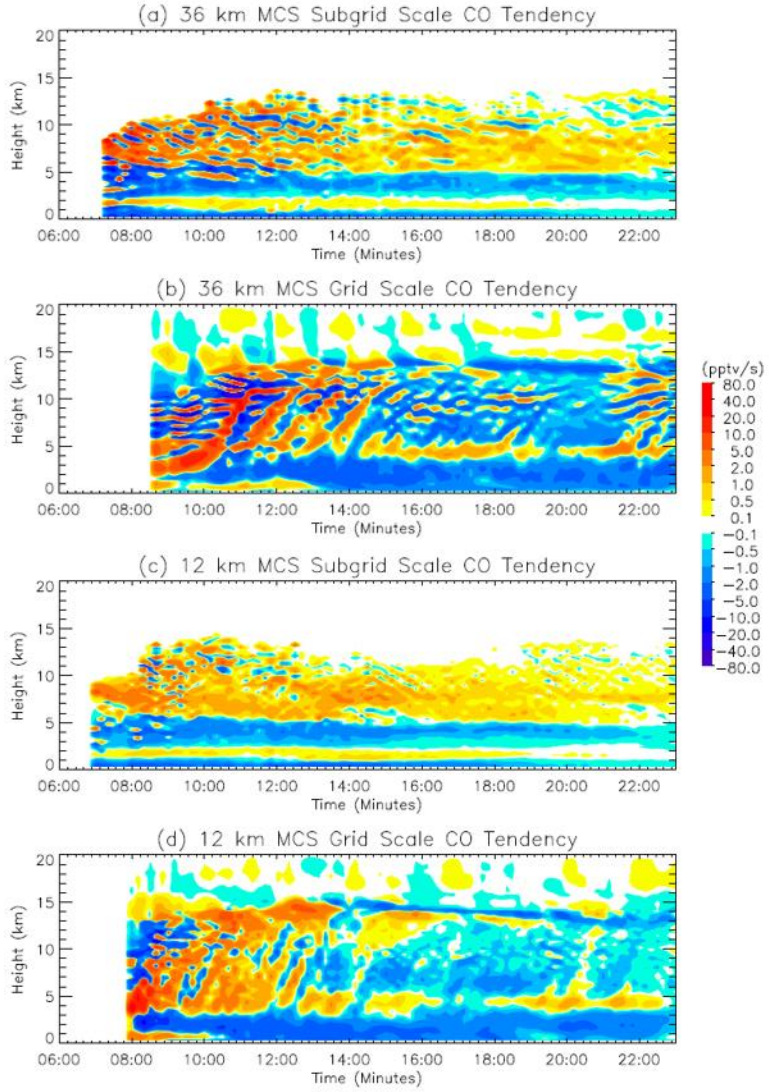

Figure 4.12 Similar to Figure 12 but for the region where precipitation was greater than 3 mm/hr.

Furthermore, we calculate the ratio (R) between the column maximum CO increase rate due to subgrid scale convection and the maximum CO increase rate due to grid scale convection at each 10-min interval model output time, and its 1 hour running mean ($\overline{R_{1h}}$) which was plotted in the Figure 4.13, using the following equation:

$$R_t = \frac{\max\left(\left(\frac{\overline{\partial C}}{\partial t}\right)_{subgrid\ 1,t}, \left(\frac{\overline{\partial C}}{\partial t}\right)_{subgrid\ 2,t}, \left(\frac{\overline{\partial C}}{\partial t}\right)_{subgrid\ 3,t} \cdots \left(\frac{\overline{\partial C}}{\partial t}\right)_{subgrid\ k,t}\right)}{\max\left(\left(\frac{\overline{\partial C}}{\partial t}\right)_{grid\ 1,t}, \left(\frac{\overline{\partial C}}{\partial t}\right)_{grid\ 2,t}, \left(\frac{\overline{\partial C}}{\partial t}\right)_{grid\ 3,t} \cdots \left(\frac{\overline{\partial C}}{\partial t}\right)_{grid\ k,t}\right)} \quad (4.6)$$

$$\overline{R_{1h}} = \frac{1}{7}\left(\sum_{t=t-3}^{t+3} R_t\right) \quad (4.7)$$

where t represents the model output time, and k represent the model height level. In Figure 14, we show the results before the grid scale and subgrid scale CO tendencies began to decay (see Figure 4.9, 4.11). After that time, the grid scale CO tendency was weak, which led to meaningless large values of the subgrid/grid ratio.

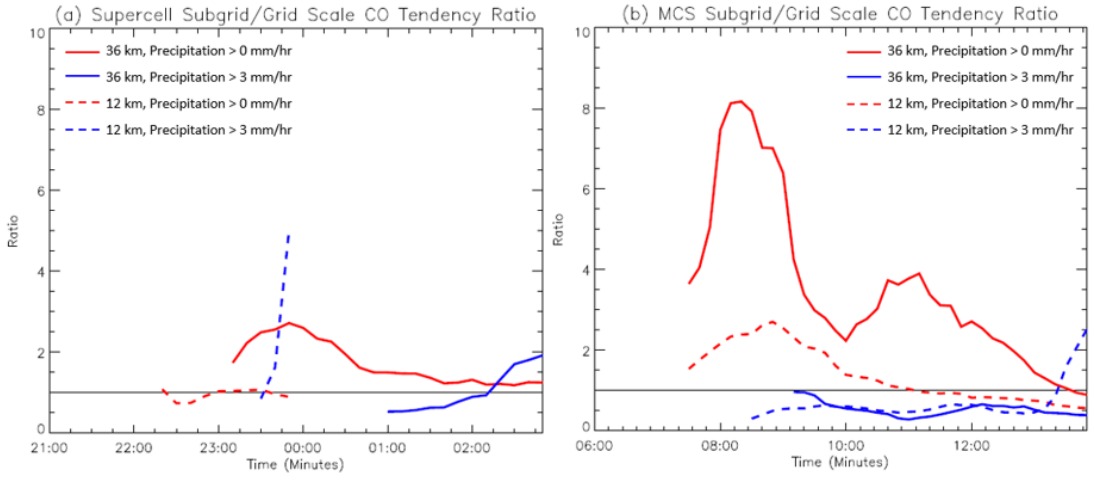

Figure 4.13 1-hour running means of the subgrid/grid convective transport ratio for the 29 May supercell case (a) and 11 June MCS case (b).

For the 29 May supercell case, in the 36 km domain, the subgrid/grid ratio was smaller in the stronger precipitation region than the precipitation > 0 mm/hr region. In the > 0 mm/hr result, the subgrid/grid ratio was always greater than 1 (solid red line), which means the subgrid scale convective transport plays a more significant role compared to the grid scale convective transport. Meanwhile, in the > 3 mm/hr result,

the subgrid/grid ratio (solid blue line) was less than 1, which means the grid scale convective transport contributes more. The 36 km results for the MCS case were similar to the 36 km results of the supercell case. In both cases, the subgrid/grid ratios in the 12 km domain were smaller than the 36 km results. Thus, the subgrid scale convection contributes more in the lower resolution domain, and when the weaker precipitation region is included (especially in the beginning of the storm). There were some large values in the supercell 12 km precipitation > 3 mm/hr results, which resulted from the weak grid scale convective transport at around 0000 UTC.

Wang et al. (1996) found that averaged over the storm duration the subgrid contribution to tracer convective transport was about 48% for a tropical MCS case at 30 km resolution and 64% for a midlatitude squall line case at 25 km resolution. However, as shown in Figure 4.13, the contribution of subgrid convective transport varies over time, which Wang et al. did not discuss. In this paper, we study the evolution of the subgrid contribution (SC) using the following equation:

$$SC_t = \frac{\sum_{tstart}^{t} \left(\frac{\partial C}{\partial t}\right)_{subgrid}}{\sum_{tstart}^{t} \left(\frac{\partial C}{\partial t}\right)_{subgrid} + \sum_{tstart}^{t} \left(\frac{\partial C}{\partial t}\right)_{grid}} \tag{4.8}$$

where tstart is the earliest time when both subgrid and grid scale convection are operating to cause positive CO tendencies at high altitude (8-14 km for the supercell case, and 10-16 km for the MCS case). Time series of SC for the first 4 hours (240 minutes) are shown in Figure 4.14. Results show that the SC is very large at the beginning but decreases as the storm develops. In the 36 km domain, the SC for both cases is initially 90 %. After two hours, the SC of the supercell case was still over 80%,

while the SC of the MCS case was around 65%. After four hours, the SC of both cases was around 30 %. In the 12 km domain, the SC was smaller than the 36 km results. The SC decreased faster in the MCS case than the supercell case, but the SC for the MCS case remained larger than that for the supercell case throughout most of the 4 hours. At 4 hours, the SC for both cases equaled 15 %.

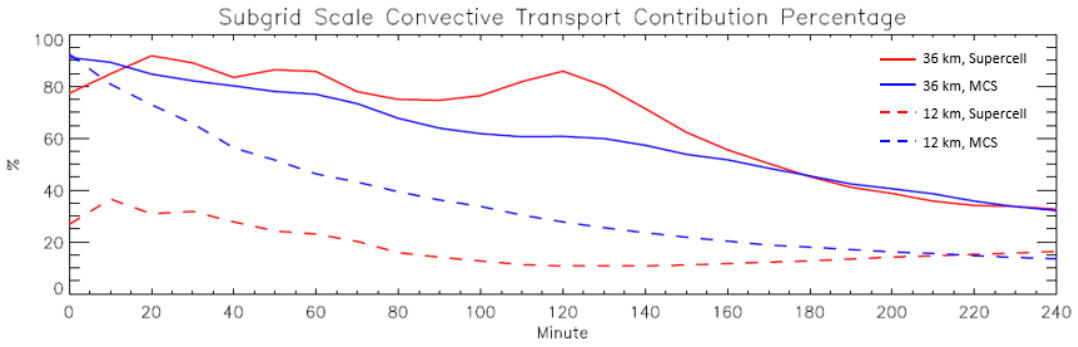

Figure 4.14 Accumulated subgrid scale convective transport contribution percentage for 29 May supercell case (red) and 11 June MCS case (blue) at a resolution of 36 km (solid) and 12 km (dash).

4.4 Summary

In this chapter, we analyze cloud parameterized deep convective transport for two different convective regimes from the DC3 field campaign using WRF-Chem simulations: a supercell case and an MCS case. The simulations were conducted at horizontal resolutions of 36 km and 12 km using 1-way nesting. We tried several cumulus parameterization schemes (KF, BMJ, GF, G3, and Tiedke) in WRF with the GF scheme producing the best comparison with observed precipitation. By tuning the closures inside the GF scheme, the model simulation of the precipitation was further improved (maximum precipitation increased by 36 %) in the supercell case. The normal

GF scheme performed well for the MCS case. The simulation at both resolutions reproduced the storm location and spatial structure. Based on the precipitation in both cases, subgrid scale convection dominated in the 36 km domain, while grid scale convection dominated in the 12 km domain. Based on the precipitation results, our convective transport study was conducted using the GF scheme in the meteorological portion of WRF-Chem.

In order to gain a better simulation of the subgrid convective transport, we replaced the WRF-Chem default scheme for the subgrid convective transport (GDCT) with a scheme that uses the mass fluxes calculated in the GF scheme to calculate the trace gas tendency due to subgrid convective transport (GFCT). Therefore, tracer transport is calculated within the GF scheme in a manner consistent with that done for water vapor. Compared with the results using GDCT and NoCT, the upper-level outflow CO mixing ratio for GFCT was 15-18 ppbv (17-18 %) larger in the 29 May supercell case resulting in a better agreement with measurements. In the 11 June MCS case, the GFCT improved the upper-level CO mixing ratio simulation in the storm core region by ~ 25 ppbv. Thus, in order to better reproduce the transport of trace gases, subgrid convective transport needs to be consistent with the convective cloud parameterization in the meteorological model that drives the chemical transport, which is not generally the case in current-generation chemical transport models such as WRF-Chem and The Community Multiscale Air Quality Modeling System (CMAQ). Furthermore, the CO mixing ratio improvement in the 29 May case was greater than in the 11 June case implying that the subgrid convective transport may be more important

in supercells than MCSs. In addition in the MCS case, we found that sub-grid scale transport results in lower CO mixing ratios near the surface due to an injection of relatively clean mid-level air to the storm downdraft, which then descends to the lower troposphere and decreases the CO mixing ratio. The GFCT scheme was able to capture this feature, which is in agreement with a cloud-resolved simulation of the storm.

Although the GFCT scheme improved the upper-level outflow CO simulation, the 36 km cloud parameterized CO mixing ratios within the upper tropospheric cloud were still smaller than the aircraft observations and the cloud resolved CO mixing ratio. In addition, the cloud parameterized CO in the outflow region on the downwind side was smaller than in the observations and cloud resolved simulation.

Furthermore, we compared the impact of vertical turbulent mixing with the subgrid convective transport. Results indicated that in the UT, the difference between turning on and turning off turbulent mixing was negligible. The subgrid convective transport dominated the vertical redistribution of the CO. However, in the lower troposphere the turbulent mixing effect was essential to a good simulation.

Moreover, we examined the CO tendency due to subgrid convective transport and grid scale convective transport. Results showed that the subgrid scale convective transport started earlier than the grid scale convective transport in the supercell case, since the grid spacing is too coarse to resolve the strength of the convergence at the beginning, thus the parameterization has to initiate until the resolved-scale can respond

to the redistribution of water and heat. While, in the MCS case, the grid scale resolved the strength of the convergence at the start of the storm, so the grid scale transport occurred nearly at the same time with the subgrid scale convective transport. As the storm started to develop, the CO detrainment layer at the storm top increased in height. Both the subgrid and grid scale convective transport reached its maximum when the grid scale convection started to form a continuous constant-altitude detrainment layer in the UT. After that time, both the subgrid and grid scale convective transport began to decay. Both the grid scale and subgrid scale CO tendencies in the supercell case were larger than in the MCS case. Furthermore, the subgrid scale convective transport played a more significant role in the supercell case than the MCS case. By comparing the CO tendency in different precipitation rate regimes, we found that both subgrid and grid scale convective transport were stronger in the higher precipitation region. The analysis of the subgrid/grid ratio demonstrated that during the development of the storm, the subgrid scale convection contributes more in the lower resolution domain and weak precipitation region (i.e. in the beginning of the storm).

Finally, we examine the subgrid contribution (SC) to the CO transport. Results show that the SC is very large at the beginning but decreases as the storm develops. In the 36 km domain, at the beginning the SC for both cases equaled 90 %. After 4 hours, the SC decreased to 30 % for both cases. In the 12 km domain, the SC was smaller than the 36 km results. The SC decreased faster in the MCS case than the supercell case. After 4 hours, the SC for both cases was around 15 %.

Chapter 5 : Evaluation of Parameterized Wet Scavenging of Trace Gases

In this Chapter, WRF-Chem is employed at cloud parameterized resolution (36 km) with chemistry and emissions to simulate the deep convective transport and wet scavenging processes of five soluble species (CH_2O, CH_3OOH, H_2O_2, HNO_3, and SO_2) in the May 29 supercell case. The purpose of this study is to evaluate the model-simulated subgrid wet scavenging and to improve subgrid wet scavenging by determining appropriate ice retention factors, and by adjusting the conversion rate of cloud water to rain water.

5.1 Description of WRF-Chem Subgrid Wet Scavenging Scheme

5.1.1 The Original WRF-Chem Subgrid Wet Scavenging Scheme

As shown in chapter 4 equation 4.3, the original WRF-Chem subgrid scheme included a sink due to wet scavenging C_{si}. C_{si} depends on the conversion rate of cloud water to rain water and on the solubility of the tracer. It is calculated using the following equation (Grell and Freitas, 2014):

$$C_{s_i} = \alpha C_u \, m_u q_r \tag{5.1}$$

Where C_u is the trace gas mixing ratio in the updraft, m_u is the updraft air mass, and q_r is the mass mixing ratio of rain. The variable α can be calculated using Henry's Law:

$$\alpha = \frac{\frac{K_h q_l}{\rho_l}}{\frac{K_h q_l}{\rho_l} + \frac{1}{R_{gas} T}} \tag{5.2}$$

$$K_h = H_{eff} \times 101.325 \quad (Unit: \frac{mol}{m^3 Pa}) \tag{5.3}$$

$$H_{eff} = H_{298} e^{-\left(\frac{\Delta H}{R}\right) t_{fac}} \quad (Unit: \frac{mol}{dm^3 atm}) \tag{5.4}$$

$$t_{fac} = \frac{t_0 - T}{t_0 T} \tag{5.5}$$

where H_{298} (M/atm=mol $dm^{-3}atm^{-1}$) is the Henry's Law coefficient at 298 K, T is the air temperature (K), q_l is total liquid water content (kg m^{-3}), ρ_l is the density of water (=1000 kg m^{-3}), Rgas is the ideal gas constant (J mol^{-1} K^{-1}), t_0 = 298 K, and $\frac{\Delta H}{R}$ is given in Table 5.1. The value of H_{eff} between 240 K and 298 K is plotted in Figure 5.1.

Table 5.1 Henry's Law parameters in the original scheme

Species	H_{298}(M atm-1)	-ΔH/R (K)
CH_2O	*3.23E+03*	*7100*
CH_3OOH	*3.11E+02*	*5241*
H_2O_2	*8.33E+04*	*7379*
HNO_3	*2.60E+06*	*8700*
SO_2	*1.2*	*3100*

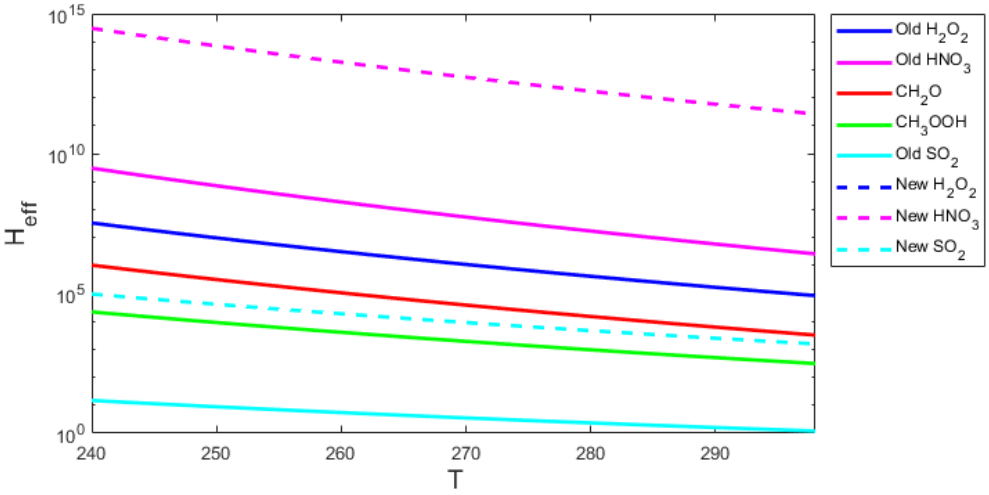

Figure 5.1 H_{eff} value between 240 K and 298 K. (note: the new H_2O_2 H_{eff} values are very close to the old ones, and the dashed line is on top of the solid line)

5.1.2 Improvement of Henry's Law's parameters

In order to be consistent with the grid scale wet scavenging code, we made some changes in the part of the calculation of the Henry's Law's coefficient in the subgrid scale wet scavenging code. For some species, including H_2O_2, HNO_3, and SO_2, H_{eff} is increased by the rapid acid dissociation in the aqueous phase (Neu and Prather, 2012):

$$H_{eff_{pH}} = H_{298_{pH}} e^{\left(-\frac{\Delta H}{R}\right)_{pH} t_{fac}} \quad (5.6)$$

$$H_{eff_{new}} = H_{eff}\left(1 + \frac{H_{eff_{pH}}}{pH}\right) \ (for\ H_2O_2\ and\ SO_2) \quad (5.7)$$

$$H_{eff_{new}} = \frac{H_{eff_{pH}}}{pH} \qquad (for\ HNO_3) \quad (5.8)$$

where pH (potential of hydrogen) equals $1e^{-5}$. The values of H_{298} and H_{298pH} used in the improved scheme are given in Table 5.2 (based on Neu and Prather, 2012; Bela, 2016b). The new H_{eff} values of H_2O_2, HNO_3, and SO_2 are shown in Figure 5.1. The result for H_2O_2 does not change much, while for the HNO_3, and SO_2, their solubility increased.

Table 5.2 Henry's Law parameters in the improved scheme

Species	H_{298}(M atm-1)	-ΔH/R (K)	H_{298pH} (M atm-1)	-ΔH/R_{pH} (K)
CH_2O	*3.23E+03*	*7100*	-	-
CH_3OOH	*3.11E+02*	*5241*	-	-
H_2O_2	*8.33E+04*	*7379*	*2.20E-12*	*-3730*
HNO_3	-	-	*2.60E+06*	*8700*
SO_2	*1.2*	*3100*	*1.30E-02*	*1965*

5.1.3 Adding Retention of Soluble Species on Frozen Hydrometeors

The original WRF-Chem subgrid wet scavenging scheme does not include the processes that occur when hydrometeors freeze (some species may partly stay in ice and partly go out to the gas phase). In the original WRF-Chem wet scavenging (Grell

and Frietas, 2014) all the soluble species stay 100% in ice. Here, we introduce an ice retention factor to the grid points with a temperature below 273.15 K to improve model simulation of the subgrid wet scavenging process:

$$C_{si} = \begin{cases} C_{si} & T \geq 273.15\ K \\ rC_{si} & T < 273.15K \end{cases} \tag{5.9}$$

where r is the ice retention factor. The value of r is discussed in section 5.3.2.

5.2 Model Setup

5.2.1 Meteorology, Chemistry and Emission Options

In this chapter, we only conducted the simulation at 36 km for the 29 May supercell case, as the subgrid convective transport of the 11 June MCS case and in the 12 km domain of both storms was not as important compared with the subgrid convective transport as shown in Chapter 4. The model setup details are listed in Table 5.3. We used the same meteorology setup as presented in Chapter 4: GF with KF closure for the cumulus parameterization; Mellor-Yamada-Janjic scheme (Janjic, 1994) for PBL scheme; two-moment Morrison microphysics (Morrison et al., 2009) for microphysical processes, the RRTMG scheme (Iacono et al., 2008) for longwave and shortwave radiation, and the Noah scheme (Koren et al., 1999) for land surface processes.

The chemistry option was MOZCART chemistry using the KPP library. Photolysis rates were calculated using the F-TUV photolysis scheme (Tie et al., 2003). Fire emissions were calculated from the FINN data. The 2011 NEI data were used to

create anthropogenic emissions. Anderson et al. (2014) and Travis et al. (2016) found that NEI overestimated the NO_x emission by 30-70 %. Therefore, we reduced the NEI NO_x emission by 50% in our simulation. I used the MEGAN v2.04 to generate biogenic emissions. Aircraft emission data were obtained from Baughcum et al. (1999). Lightning NOx production is set at 82 moles per flash (Cummings, 2017) for both cloud-to-ground and intracloud flashes (see Section 5.2.3).

Table 5.3 WRF-Chem model configuration and physics and chemistry options.

Meteorology Initial/Boundary Conditions	*NAM 18 UTC*
Chemistry Initial/Boundary Conditions	*MOZART scaled*
Grid Resolution	*36 km*
Vertical Levels	*90*
Time step	*120 s*
Cumulus Parameterization	*GF with KF closure*
Microphysics	*Morrison*
PBL	*MYJ*
Longwave Radiation	*RRTMG*
Shortwave Radiation	*RRTMG*
Lightning Schemes	*Price and Rind [1992; PR92] lightning flash rate scheme based on level of neutral buoyancy (Wong et al., 2013)*
Cloud Top Height Adjustment	*0*
Flashrate Factor	*17*
LNO_x Scheme	*Combined intra-cloud and cloud-to-ground flashes single-mode vertical distributions with LMA flashes vertical profile*
Moles of NO emitted per intra-cloud flash	*82*
Moles of NO emitted per cloud-to-ground flash	*82*
Fire Emissions	*FINN*
Anthropogenic Emissions	*NEI with NO_x reduced by 50%*
Biogenic Emissions	*MEGAN v2.04*
Chemistry Option	*MOZCART*

5.2.2 IC/BC for Chemistry

We used MOZART-4 to create the chemical IC and BC. In order to have a better simulation of simulated inflow, I adjusted the IC to better match aircraft observations using the equations listed in Table 5.4. The model simulated inflow trace gas mixing ratios are compared with aircraft data in Table 5.4. The differences between the simulation and observation of all the species in low-level inflow were within 10 % of the aircraft measurements, except H_2O_2. However, the high level H_2O_2 in the inflow will not affect the H_2O_2 in the outflow due to its high solubility and short lifetime in the lower troposphere.

Table 5.4 IC formulation equations with inflow observations and simulation

Species	IC equations	Observation	WRF-Chem inflow
CO	*C=C(72+2H)/100 0<H<14 km*	*136.8 ± 1.1*	*141.4 ± 1.4*
CH_2O	*C=C((14-H)*0.8+1) 0<H<14 km*	*5.2 ± 0.3*	*4.9 ± 0.2*
CH_3OOH	*C=C((14-H)*0.25+1) 0<H<14 km*	*1.6 ± 0.1*	*1.6 ± 0.0*
HNO_3	*C=C(58+3H)/100 0<H<14 km*	*0.6 ± 0.1*	*0.6 ± 0.0*
O_3	*C=C(60+10H)/100 0<H<4 km*	*54.9 ± 1.9*	*59.5 ± 0.8*
H_2O_2	*C=0.3C*	*2.5 ± 0.2*	*6.6 ± 0.0*
SO_2	-	-	*0.5 ± 0.2*

5.2.3 Lightning NO_x

The lightning option is PR92 (Price and Rind, 1992; Wong et al., 2013) which is the recommended method for predicting lightning flash rate for parameterized convection in WRF-Chem. This scheme is based on the level of neutral buoyancy from the convective parameterization. However, this scheme severely underpredicted the flash rates for this storm. Therefore, I used a flash rate adjustment factor of 17 to get the best simulation of the ENTLN observed storm total flashes (ENTLN measured

strokes/4, personal communication from Earth Networks to Dr. Kenneth Pickering) between 2100 UTC – 0500 UTC (Figure 5.2). The LNO_x scheme we used is based on Ott et al. (2010), but with the vertical profile (Cummings, 2017) of the total flashes observed by OKLMA (Figure 5.3). The LNO_x production rate is based on Cummings (2017). I compared the simulated NO_x with the aircraft measured NO_x at the time (100 min later than the aircraft measurement time) when the model simulated cumulative flashes was similar with the ENTLN observed cumulative flashes at the aircraft measuring time. As the simulated LNO_x had not been convectively transported to as high an altitude in the model as indicated by the aircraft, I compared the simulated NO_x at an altitude 0.5 km lower than the observations. The simulated mean NO_x mixing ratio (1.46 ppbv) matched the observed NO_x (1.44 ppbv).

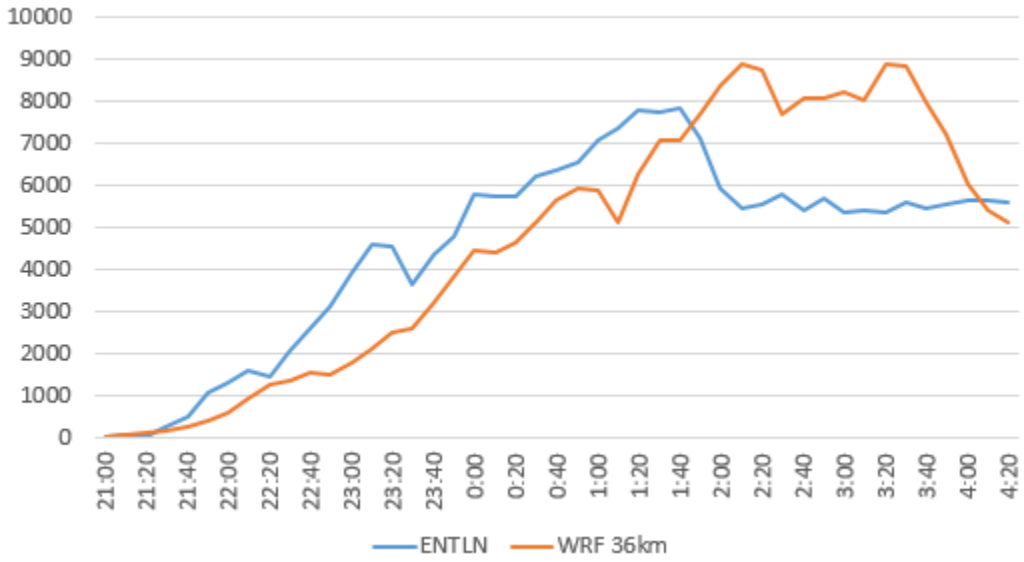

Figure 5.2 ENTLN measured flashes (blue) with 80 min later model simulated flashes (orange).

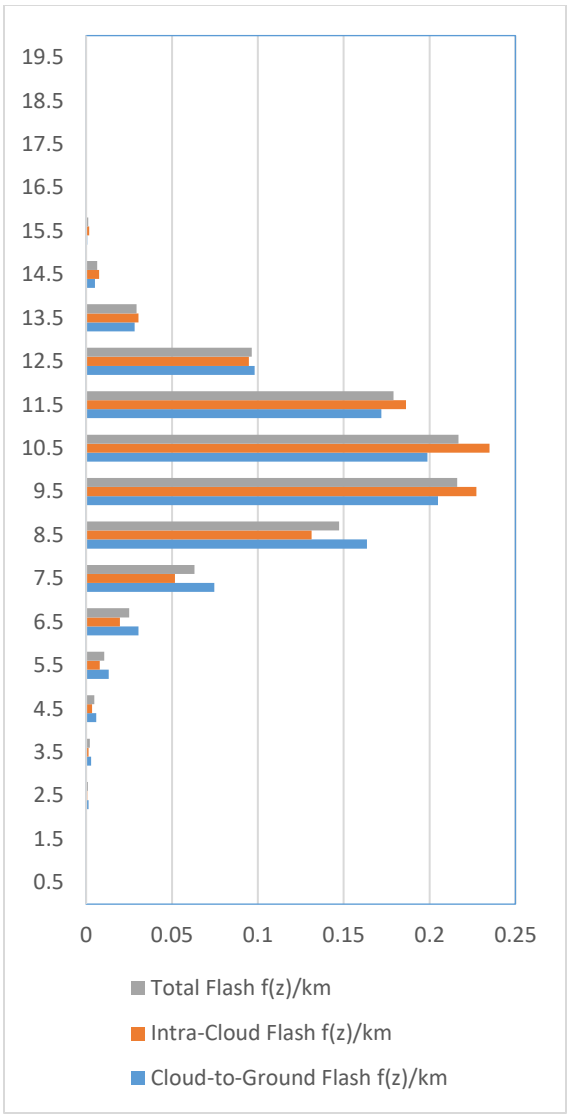

Figure 5.3 Vertical profile of total flashes (green), intra-cloud flashes (orange), and cloud-to-ground flashes (blue)

5.3 Results

5.3.1 Results without Retention of Soluble Species on Ice

Two WRF-Chem runs were conducted in this section. In the first run, I ran WRF-Chem without wet scavenging (both grid and subgrid). In the second run, I ran

with wet scavenging (both grid and subgrid). I compared the simulated UT vertical profiles of in-cloud CH_2O, CH_3OOH, H_2O_2, HNO_3, and SO_2 along the aircraft measuring track with the GV and DC8 outflow measurements. The analysis times for the model simulation and the observations are the same as the times used in Chapter 4. Results are shown in Figure 5.4. The WRF-Chem original wet scavenging scheme removed too much of the CH_2O, CH_3OOH and H_2O_2 in the UT, while the wet scavenging of HNO_3 was not sufficient.

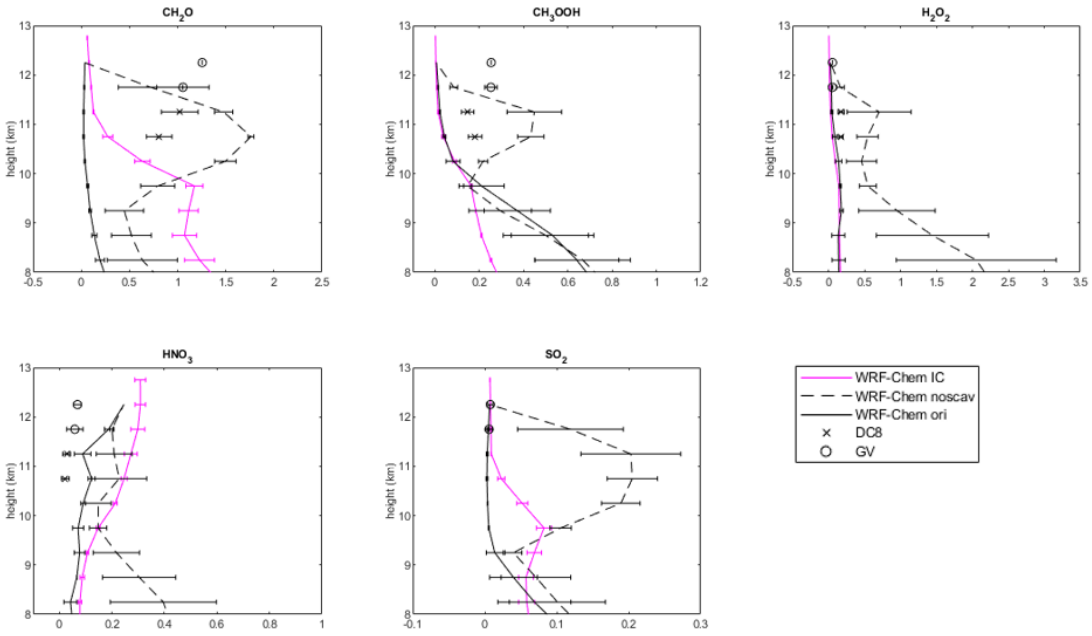

Figure 5.4 Mean outflow vertical profiles (ppb) of CH_2O, CH_3OOH, H_2O_2, HNO_3, SO_2, from the 29 May supercell storm as observed by the DC-8 (black cross) and GV (black circle) aircraft, mean profiles as simulated in the 36 km resolution WRF-Chem run with (black solid line) and without (black dash line) original WRF-Chem, compared with the IC for cloud parameterized run (magenta). Model profiles shifted in east-west direction with respect to the aircraft profiles by 0.75 degrees west to ensure sampling of model outflow.

According to Grell and Freitas (2014), the subgrid scale wet scavenging depends on the solubility of the tracer and on the conversion rate of cloud water to rain water. In order to improve subgrid wet scavenging simulation, I tried adjusting the

solubility of the tracer by introducing the ice retention factor in section 5.3.2, and adjusting the conversion rate of cloud water to rain water in section 5.3.3.

5.3.2 Estimates of Retention on Ice

One possible reason for the overestimate of subgrid wet scavenging in the UT is that the original WRF-Chem subgrid wet scavenging scheme does not separate scavenging by ice and water. When cloud water freezes, part of the dissolved gases will be released into the air. In cloud-resolved modeling Leriche et al. (2013) used ice retention factors for SO_2, H_2O_2, and HNO_3 based on the results from previous studies (Voisin et al., 2000; von Blohn et al., 2011). They found that chemical species with very high effective Henry's law constants (e.g. strong acids) are likely to be fully retained in the ice hydrometeor under all conditions. Highly soluble gases such as strong acids are almost completely dissociated in water so ions are hardly able to leave the liquid phase (von Blohn et al., 2011). For chemical species with lower effective Henry's law constants (e.g. SO_2 and H_2O_2), the pH, temperature, drop size, and air speed around the hydrometeor become important factors in the retention fraction (Stuart and Jacobson, 2004). Following this conclusion, they estimated the ice retention factors for CH_2O and CH_3OOH using data for SO_2 and H_2O_2 and according to the values of the effective Henry's law constant. They suggested using the same ice retention factor for SO_2 as for CH_3OOH, and using the same ice retention factor as H_2O_2 for CH_2O.

Without dealing with the ice wet scavenging process separately from the liquid water wet scavenging will overestimate the scavenging efficiency. Therefore, here I add an ice retention factor (r) in the model following equation 5.9. I tested five ice retention factor values: r=0, r=0.1, r=0.25, r=1, and r=var (values varying by species, as defined in Leriche et al., 2013, see Table 5.5). The ice retention factor was applied to both subgrid and grid scale wet scavenging. Results are shown in Figure 5.5.

Table 5.5 Ice retention fraction values for each soluble species in the WRF-Chem simulation

	CH_2O	CH_3OOH	H_2O_2	HNO_3	SO_2
No scav.	*0*	*0*	*0*	*0*	*0*
scav. r=0	*0*	*0*	*0*	*0*	*0*
scav. r=0.1	*0.1*	*0.1*	*0.1*	*0.1*	*0.1*
scav. r=0.25	*0.25*	*0.25*	*0.25*	*0.25*	*0.25*
scav. r=1	*1*	*1*	*1*	*1*	*1*
scav. r=var	*0.64*	*0.02*	*0.64*	*1*	*0.02*

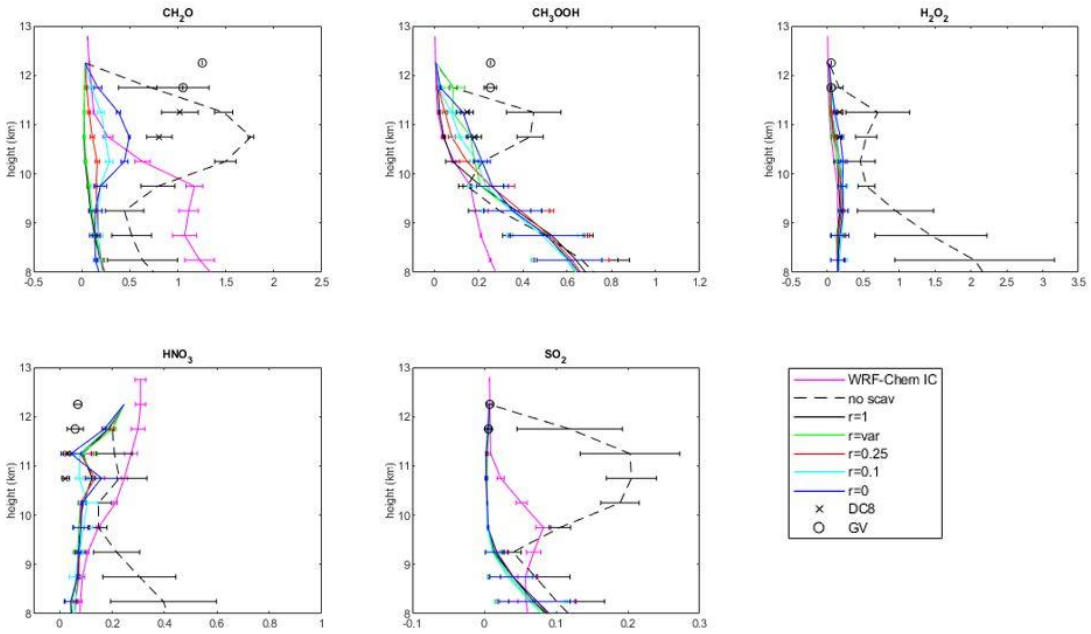

Figure 5.5 Similar with Figure 5.3, but with 5 sensitivity runs with different ice retention factors: r=0 (blue), r=0.1 (cyan), r=0.25 (red), r=var (green), and r=1.

The introduction of the ice retention factor improved the model simulation of CH_2O, CH_3OOH and H_2O_2, the wet scavenging efficiencies for which were overestimated in the original WRF-Chem run. Compared to the original WRF-Chem results (r = 1.0), when using r=0, the differences between observation and simulation were reduced by 26%, 37%, and 16% for CH_2O, CH_3OOH and H_2O_2. I compared the average aircraft measurements with the model simulation in the same area in Table 5.6. According to Figure 4.7, the simulated UT CO peak was 0.5 km lower than the observed UT peak, which means that the model simulated maximum detrainment layer was around 0.5 km lower than the observation, so in Table 5.6, we compared the aircraft measurement with the simulation model layer that was 0.5 km lower than the aircraft measuring height.

Table 5.6 Values from observations and WRF-Chem simulations of mean mixing ratio (ppb) of soluble species in UT outflow region

	OBS	rf=0	rf=0.1	rf=0.25	rf=var	rf=1	No scav.
CH_2O	*1.036*	*0.374*	*0.210*	*0.102*	*0.034*	*0.030*	*1.364*
CH_3OOH	*0.209*	*0.135*	*0.100*	*0.073*	*0.128*	*0.041*	*0.296*
H_2O_2	*0.115*	*0.144*	*0.116*	*0.1*	*0.077*	*0.080*	*0.469*
HNO_3	*0.044*	*0.115*	*0.109*	*0.119*	*0.124*	*0.122*	*0.196*
SO_2	*0.007*	*0.004*	*0.004*	*0.004*	*0.005*	*0.004*	*0.179*

For CH_2O, all the runs with wet scavenging underestimate the UT CH_2O mixing ratio. The run without wet scavenging produced the best result. One possible reason is that the model removes too much CH_2O below the altitude of the freezing point. When using wet scavenging, the usage of r=0 produced the closest result to the observation. For CH_3OOH, r=0 produced the best result. Similar to CH_2O, all the runs with wet scavenging underestimate the UT CH_3OOH mixing ratio. For H_2O_2, r=0.1 gave the best

result. The difference between r=0.1 and the observation is less than 1%. For HNO_3, all the runs overestimate the UT mixing ratio. For SO_2, all the runs with wet scavenging produced very good results compared to the no wet scavenging run, which had too much SO_2 in the upper troposphere.

Furthermore, we calculated the scavenging efficiencies (SE) from the WRF-Chem simulations as the percentage difference in mean outflow values between the simulations with and without scavenging following Bela et al. (2016a):

$$SE(\%) = 100 \times \left(\frac{\overline{C_{noscav}} - \overline{C_{scav}}}{\overline{C_{noscav}}} \right) \tag{5.10}$$

where C_{noscav} and C_{scav} are the mean in-cloud outflow values of trace gases in the simulation without wet scavenging and the simulation with wet scavenging, respectively. The SE results are compared to the observed SE result from Bela et al. (2016a) for the 29 May supercell case in Figure 5.6.

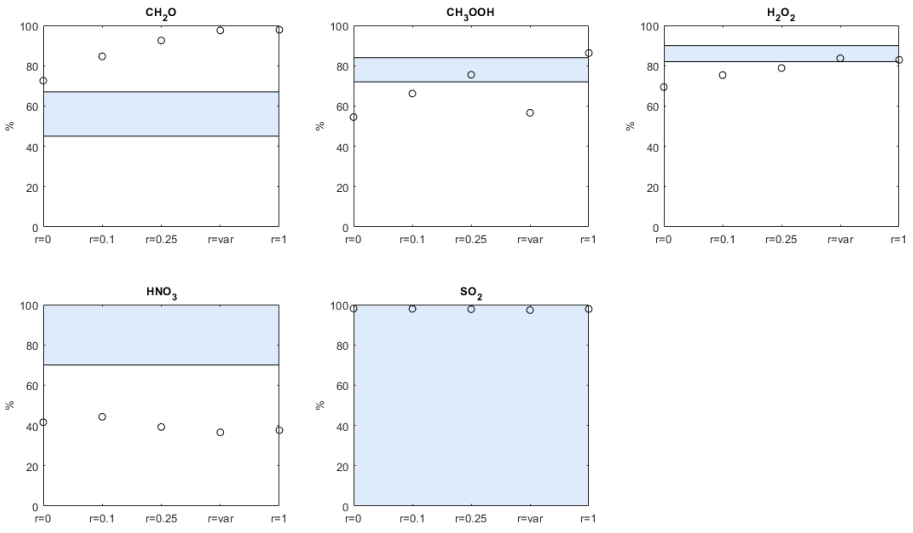

Figure 5.6 Observed scavenging efficiencies (shaded) and model simulated scavenging efficiencies (circle) from 5 sensitivity runs with different ice retention factors: r=0, r=0.1, r=0.25, r=1, and r=var.

For CH_2O, all the runs overestimate the SE. However, lowering the ice retention factor reduces the difference between modeled and observed SEs, and the SE from r=0 is the closest one to the observation. For CH_3OOH, r=0.25 produced the best result. For H_2O_2, best result comes from r=var (0.64) run. For HNO_3, all the runs underestimate the SEs. For SO_2, all the simulated SEs are within the observed SE range. Comparing the SEs for all the five species, we found that the simulated SEs for CH_3OOH were highly sensitive to the ice retention factor (for r ranging from 0 to 1, SE=54%-86%), which is consistent with what was found in Bela et al. (2018).

5.3.3 Improving the Cloud to Rain Ratio

In the original GF cumulus scheme, the following equations are used to calculate conversion rate (c_0) of cloud water to rain water:

$$c_0 = \begin{cases} 0.004 & T \geq 270\ K \\ 0.002 & T < 270K \end{cases} \tag{5.11}$$

We adjusted the conversion rate (c_0) following Han and Hong (2016) using the equation below:

$$c_0 = \begin{cases} a & T \geq 273.15\ K \\ ae^{[b(T-273.15)]} & T < 273.15K \end{cases} \tag{5.12}$$

where a=0.004, b=0.07. The c_0 values between 220 K and 298 K are shown in Figure 5.7. Compared to the original c_0 value in the GF scheme, the new c_0 is reduced below 260 K, which is at 6 km and above.

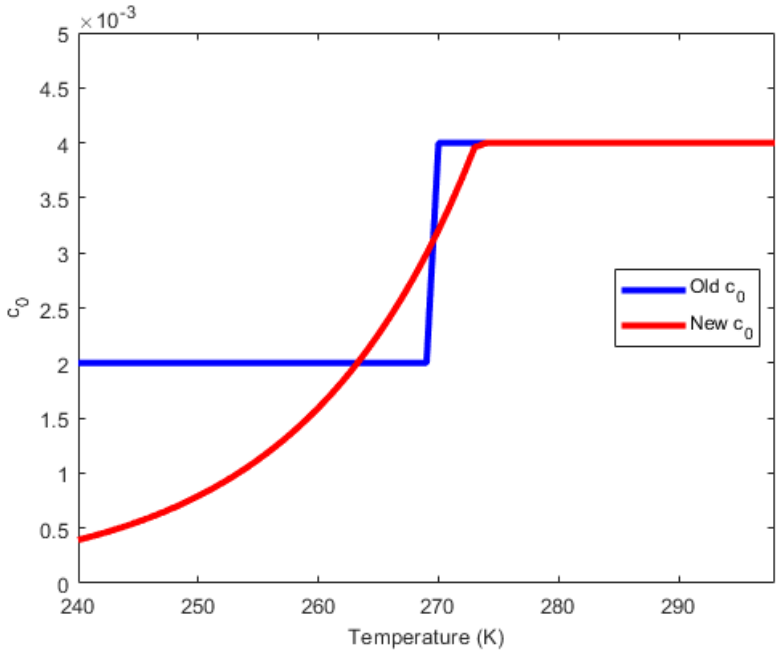

Figure 5.7 Conversion rate (c_0) of cloud water to rain water from the original GF scheme (blue), and the new conversion rate (red) based on Han and Hong (2016).

As in section 5.3.2, we conducted five sensitivity runs with different ice retention factors (Table 5.5), and a run without wet scavenging using the new conversion rate of cloud water to rain water. The simulated vertical profile of the soluble trace gases, mean mixing ratios in the UT outflow region, and SEs are shown in Figure 5.8, Table 5.7 and Figure 5.9, respectively. Compared to the results in section 5.3.2, use of the new conversion rate of cloud to rain improves the outflow CH_2O and CH_3OOH mixing ratios, by increasing UT CH_2O mixing ratios by 12 % and increasing CH_3OOH by 63%. Similar to the results in section 5.3.2, r=0 produced the best result for CH_2O and CH_3OOH; r=0.1 produces the best result for H_2O_2. All the wet scavenging runs overestimate the HNO_3 mixing ratio; all the wet scavenging runs well reproduced the observed SO_2 in UT. In addition, we found that changing the conversion rate does not affect the SEs much.

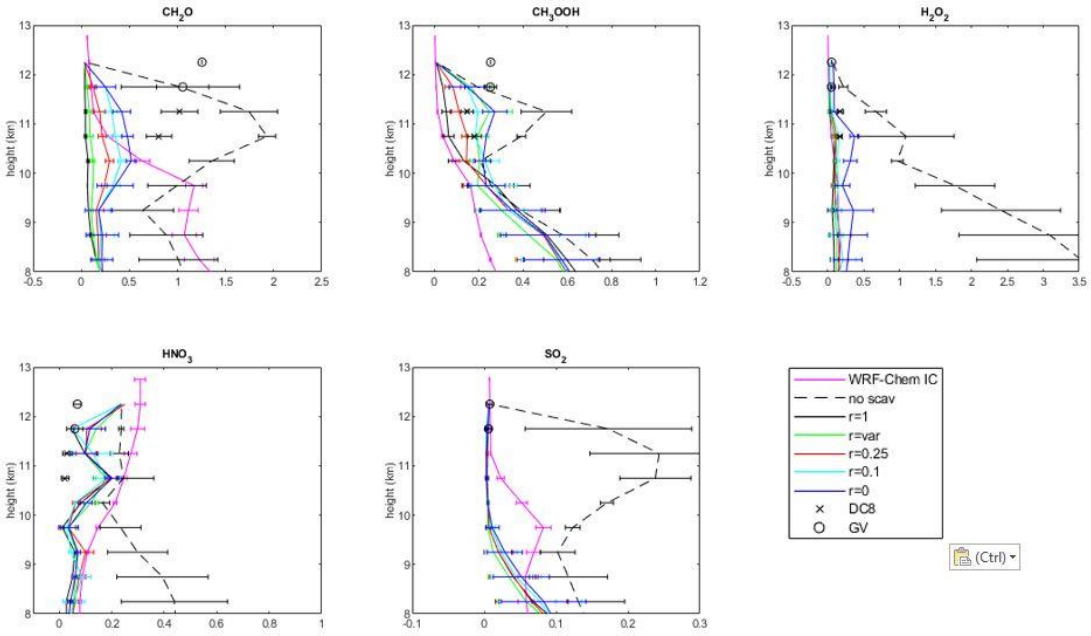

Figure 5.8 Similar to Figure 5.5, but for the runs with the new conversion rate of cloud water to rain water.

Table 5.7 Similar to Table 5.6, but for the runs with the new conversion rate of cloud water to rain water.

	OBS	r=0	r=0.1	r=0.25	r=var	r=1	No scav.
CH_2O	*1.036*	*0.419*	*0.335*	*0.208*	*0.092*	*0.05*	*1.517*
CH_3OOH	*0.209*	*0.219*	*0.189*	*0.122*	*0.202*	*0.072*	*0.325*
H_2O_2	*0.115*	*0.219*	*0.096*	*0.079*	*0.069*	*0.059*	*0.738*
HNO_3	*0.044*	*0.130*	*0.105*	*0.118*	*0.134*	*0.106*	*0.219*
SO_2	*0.007*	*0.004*	*0.003*	*0.004*	*0.004*	*0.005*	*0.206*

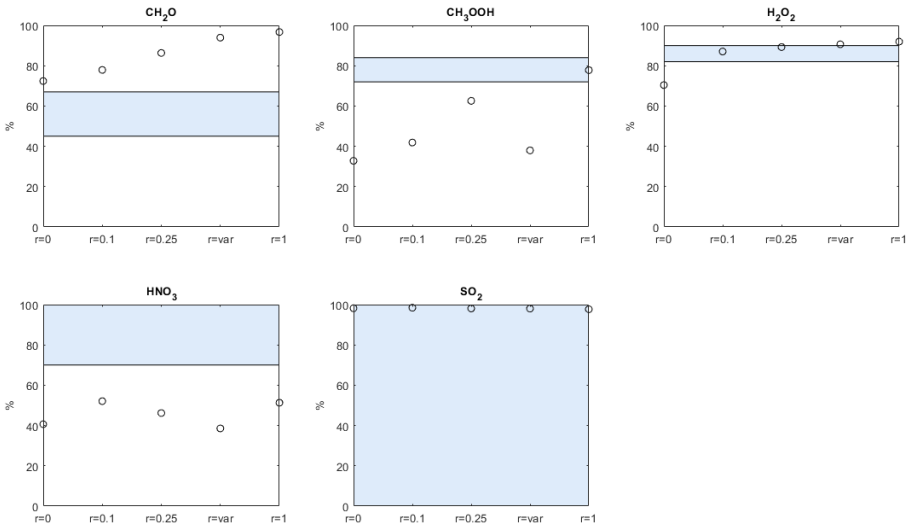

Figure 5.9 Similar to Figure 5.5, but for the runs with the new conversion rate of cloud water to rain water.

Based on all the results in section 5.3.2 and section 5.3.3, we concluded that the best estimate of the ice retention factor for each soluble species are: r=0 for CH_2O and CH_3OOH, r=0.1 for H_2O_2. The model overestimated the HNO_3 even with r=1, so we suggest using r=1 for HNO_3. Our best estimates of the ice retention factors for CH2O and H_2O_2 are lower than Leriche et al. (2013), but similar for CH_3OOH. Compared to the best estimate from Bela et al. (2016) which were based on the cloud resolved simulation, our results are close to their results except for CH_3OOH (their best estimate was 1).

5.4 Summary

In this chapter, we evaluated the simulation of WRF-Chem subgrid wet scavenging. We use WRF-Chem to simulate the 29 May supercell storm observed during the DC3 field campaign at 36 km resolution, and compare the mixing ratio of

five soluble species (CH_2O, CH_3OOH, H_2O_2, HNO_3, and SO_2) from the model simulation and aircraft observation. CH_2O, CH_3OOH, H_2O_2 are important HO_x precursors, and HO_x is necessary for ozone production. HNO_3 is an important NO_x reservoir species, and SO_2 is an important source of sulfate aerosol in the UT.

Simulation results showed that the original WRF-Chem wet scavenging scheme removed too much CH_2O, CH_3OOH and H_2O_2 in the UT, and overestimated the HNO_3 mixing ratio in the cloud outflow region. In order to improve subgrid wet scavenging simulation, we adjusted the solubility of the tracer by introducing the ice retention factor, and adjusted the conversion rate of cloud water to rain water.

The introduction of the ice retention factor improves the model simulation of CH_2O, CH_3OOH and H_2O_2, whose wet scavenging efficiencies were overestimated in the original WRF-Chem run. Compared to the original WRF-chem results, when using r=0, the differences between observation and simulation were reduced by 26%, 37%, and 16% for CH_2O, CH_3OOH and H_2O. The usage of the new conversion rate of cloud water to rain water provided an additional improvement of CH_2O, CH_3OOH by increasing CH_2O by 12 % and increasing CH_3OOH by 63%. However, the simulated CH_2O was still much lower (60%) than the observation, and the simulated HNO_3 was still higher (1.38 times greater) than the observation. The SE analysis demonstrated that all the wet scavenging runs underestimate the SE of HNO_3, and overestimated the SE of CH_2O.

Based on the results in section 5.3.2 and section 5.3.3, we concluded that the best simulation is using the new conversion rate of cloud water to rain water, and using ice retention factor for soluble species. The best estimate of the ice retention factors are: r=0 for CH_2O and CH_3OOH, r=0.1 for H_2O_2, r=1 for HNO_3. The SO_2 simulation did not respond to the change of ice retention factor, so we suggest the value from the laboratory results, which is 0.02. Our best estimates of the ice retention factors for CH2O and H_2O_2 are lower than Leriche et al. (2013) and similar for CH_3OOH. Compared to the best estimate from Bela et al. (2016), which were based on the cloud resolved simulation, our results are close to their results except for CH_3OOH (their best estimate was 1).

Chapter 6 : Tropospheric Ozone Production Downwind of Deep Convection

In this Chapter, we use the model described in Chapter 5 with our best estimate of ice retention factors, which are r=0 for CH_2O and CH_3OOH, r=0.1 for H_2O_2, r=1 for HNO_3, and r=0.02 for SO_2, to run a much longer simulation (from 1800 UTC 29 May to 0000 UTC 31 May) to study the ozone change downwind of deep convection. Four sensitivity runs were conducted to analyze the influence of the ice retention factor on downwind ozone production. The purpose of this chapter is to estimate the downwind production of ozone and its sensitivity to the choice of different ice retention factors.

6.1 Ozone Simulation (Control Simulation) Compared with Aircraft Data at Time of Active Convection

The vertical profile of observed and simulated mean in-cloud ozone along the aircraft measurement track is shown in Figure 6.1. I removed the points affected by stratospheric ozone for both aircraft measurements and simulations by excluding the points where the observed and modeled ratio of O_3 to CO was greater than 1.25. It is not appropriate to include these points as the model does not include stratospheric chemistry. Therefore, in Figure 6.1, there was no model simulation results plotted on the level of 12.25 km. Besides that, the model well reproduced the mean ozone vertical distribution.

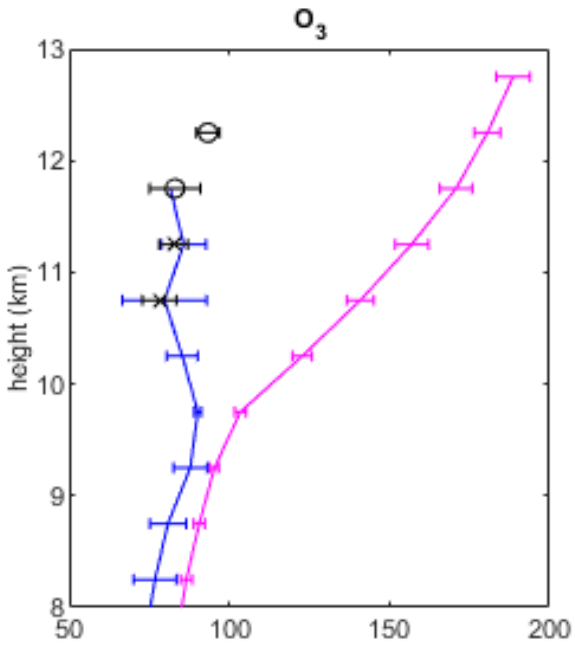

Figure 6.1 Mean anvil outflow vertical profiles (ppbv) of O_3 from the 29 May supercell storm as observed by the DC-8 (black cross) and GV (black circle) aircraft, mean profiles as simulated in the 36 km resolution WRF-Chem (blue), compared with the IC for cloud parameterized run (magenta). Model profiles shifted in east-west direction with respect to the aircraft profiles by 0.75 degrees west to ensure sampling of model anvil outflow.

As the storm developed, the UT ozone mixing ratio was reduced due to the convective transport of low ozone air from the PBL to the UT. The aircraft measured mean ozone mixing ratios in the storm anvil region are shown in Table 6.1. The GV measured mean ozone mixing ratio was 82.9 ppbv and the DC8 measured mean ozone mixing ratio was 78.1 ppbv. The model simulated mean ozone mixing ratio at GV measuring height was 81.6, and the simulated average ozone mixing ratio at DC-8 measuring height was 79.8 ppbv. The model simulated mean ozone mixing ratios were close to the observations (the differences between the observation and simulation were less than 2%).

Table 6.1 Aircraft measured and model-simulated mean ozone (ppbv) in the storm anvil and one day downwind of storm.

	DC8 measuring altitude		GV measuring altitude	
	OBS	WRF-Chem	OBS	WRF-Chem
Storm region	78.1±5.3	79.8±13.0	82.9±8.0	81.6±7.0
1 day after	104.3±3.3	97.0±6.9	113.5±1.4	115.8±11.7
Net ozone change	25.9	17.2	30.6	34.2
Net ozone production	-	10.7±1.0	-	5.5±2.5

6.2 Downwind Ozone Production

Guided by near-real-time GOME-2 satellite data for NO_2 and forecast trajectory analysis, the DC-8 and GV measured the storm outflow of the 29 May supercell case in the southern Appalachian region on the day following the storm (30 May). The DC-8 mainly measured at ~ 11 km from 2100 UTC 30 May to 0000 UTC 31 May, and GV mainly sampled at ~ 11.4 km from 2200 UTC to 2330 UTC 30 May. The aircraft measured ozone on 30 May in the downwind region was larger than the ozone mixing ratio measured in the anvil outflow during the active storm (Table 6.1). The mean ozone mixing ratio at 11 km measured by DC-8 was 104.3 ppbv, which was 25.9 ppbv larger than one day before in the anvil outflow, while the mean ozone mixing ratio at 11.4 km measured by GV was 113.5 ppbv, which was 30.6 ppbv larger than one day before.

Figures 6.2-6.7 show the hourly simulated NO_x and ozone mixing ratio at the DC-8 measurement altitude (~11 km, left) and GV measurement altitude (~11.4 km, right), compared with the aircraft measurements. As the modeled storm started 80 min later than the observation, I plotted the aircraft data 80 min later in Figures 6.2-6.7. In

Figure 6.2-6.7, the model reproduced the UT NO_x and ozone horizontal transport. The high NO_x and low ozone air, which represented the storm downwind outflow, was transported to the southern Appalachian region by the end of 30 May.

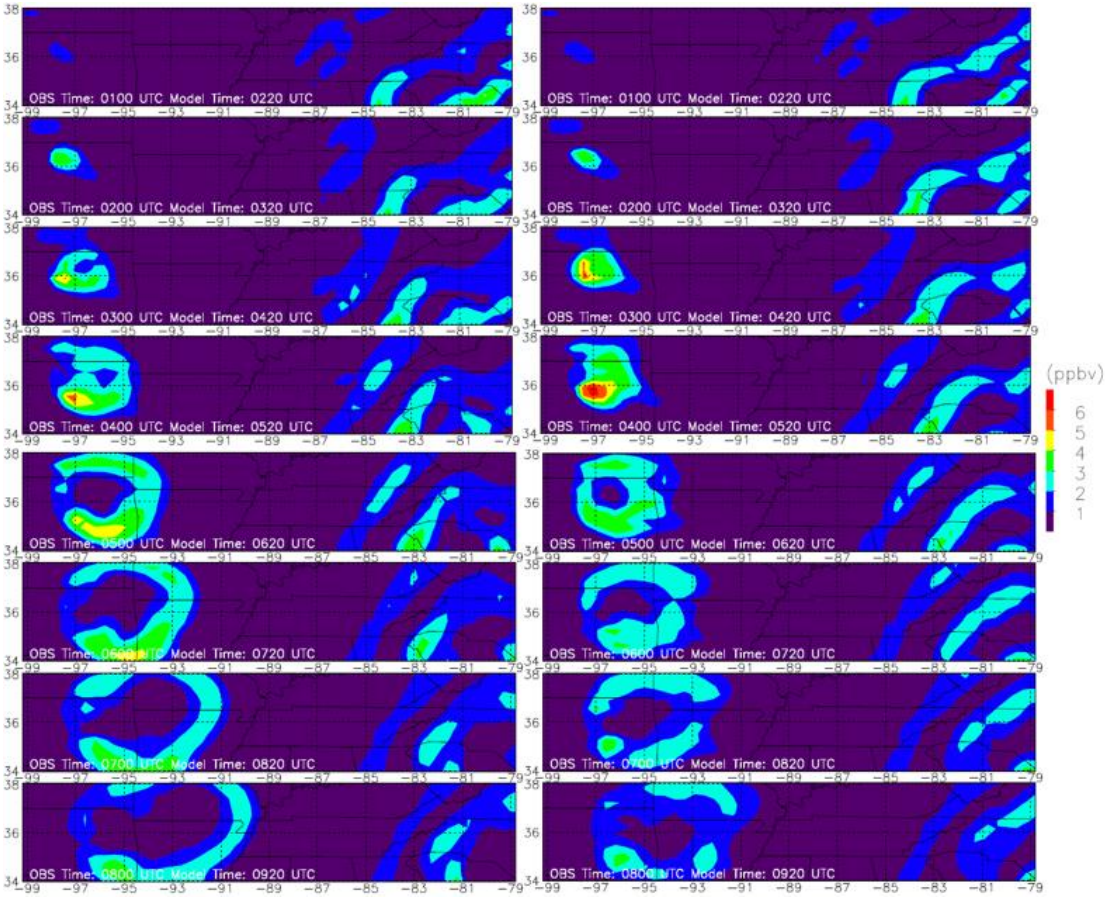

Figure 6.2 Hourly NO_x simulation at 11 km from 0100 UTC to 0800 UTC (model time: 0220 UTC to 0920 UTC) 30 May at 11 km (left); and NO_x simulation at 11.4 (right).

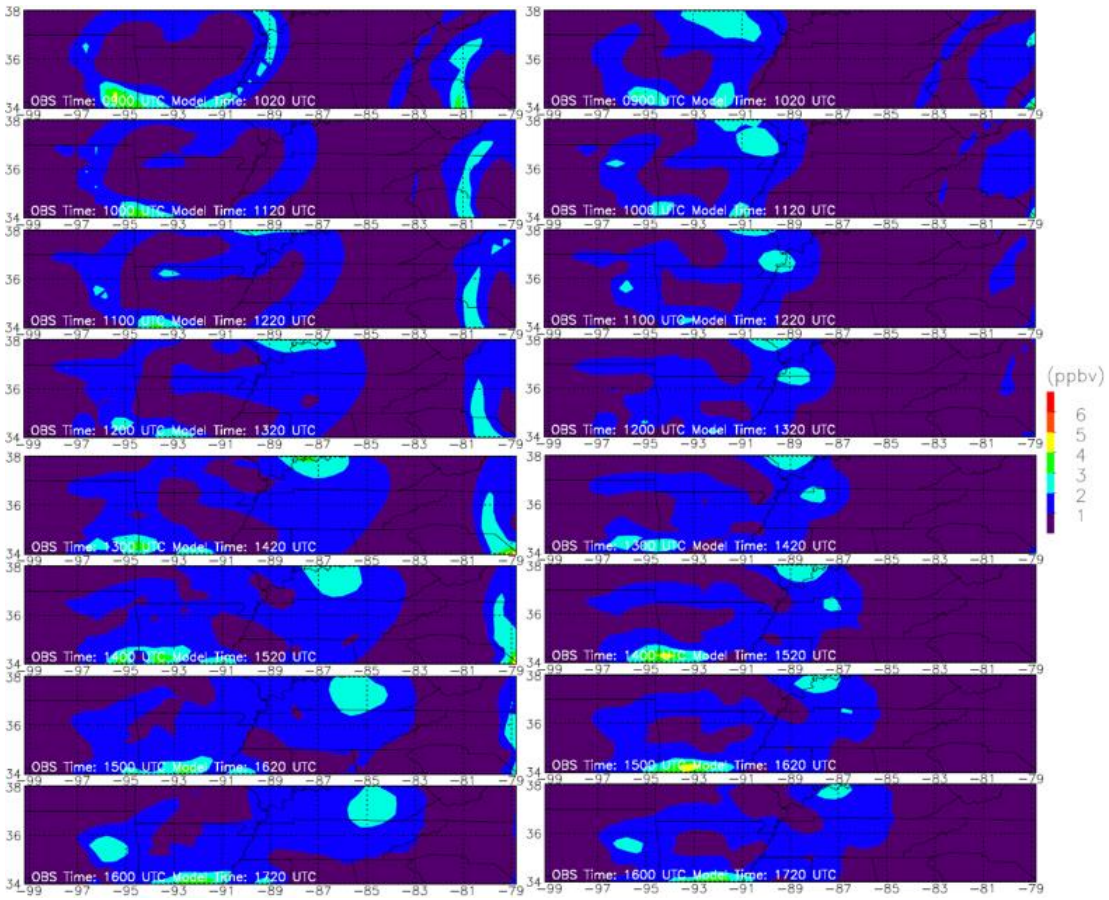

Figure 6.3 Similar to Figure 6.2, but from 0900 UTC to 1600 UTC (model time: 1020 UTC to 1720 UTC) 30 May.

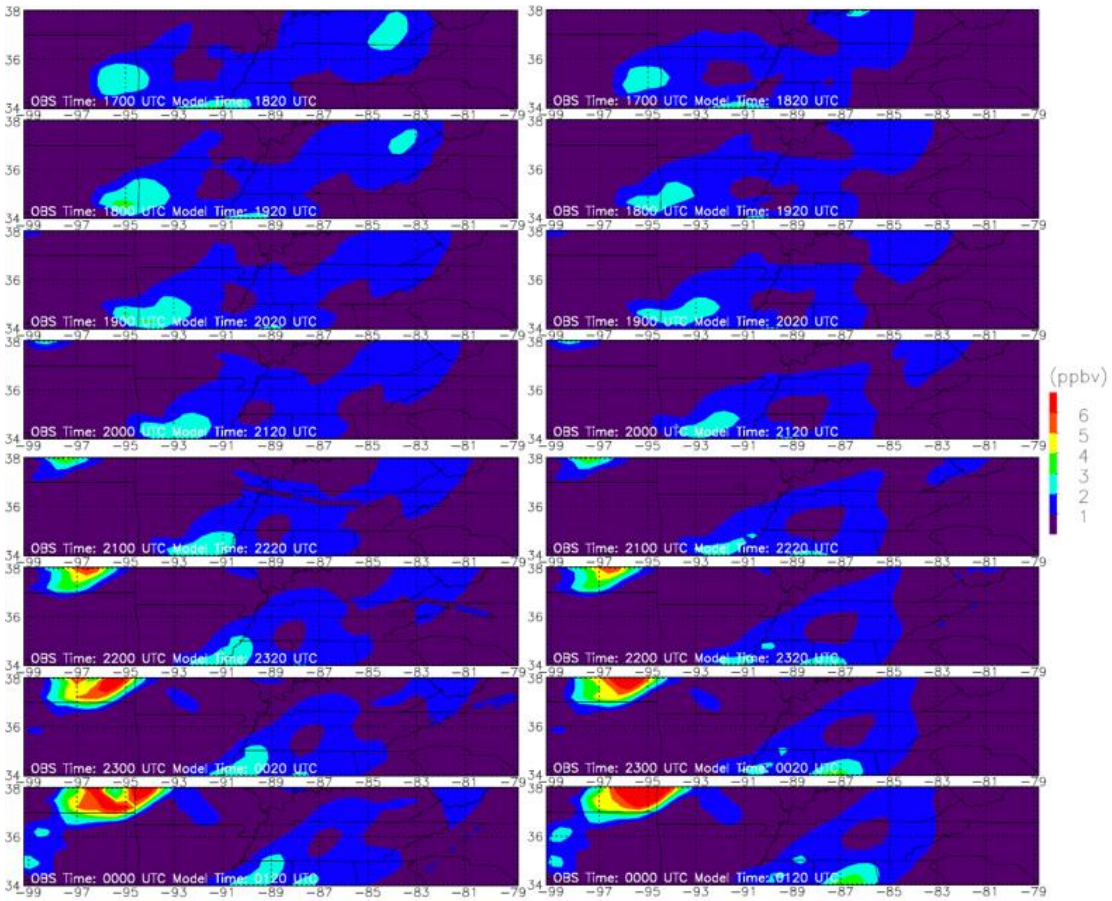

Figure 6.4 Similar to Figure 6.2, but from 1700 UTC 30 May to 0000 UTC 31 May (model time: 1820 UTC 30 May to 0120 UTC 31 May) with DC-8 measurements (circles, left); and with GV measurements (circles, right). The aircraft measuring time was between 80-140 min before the model plotting time.

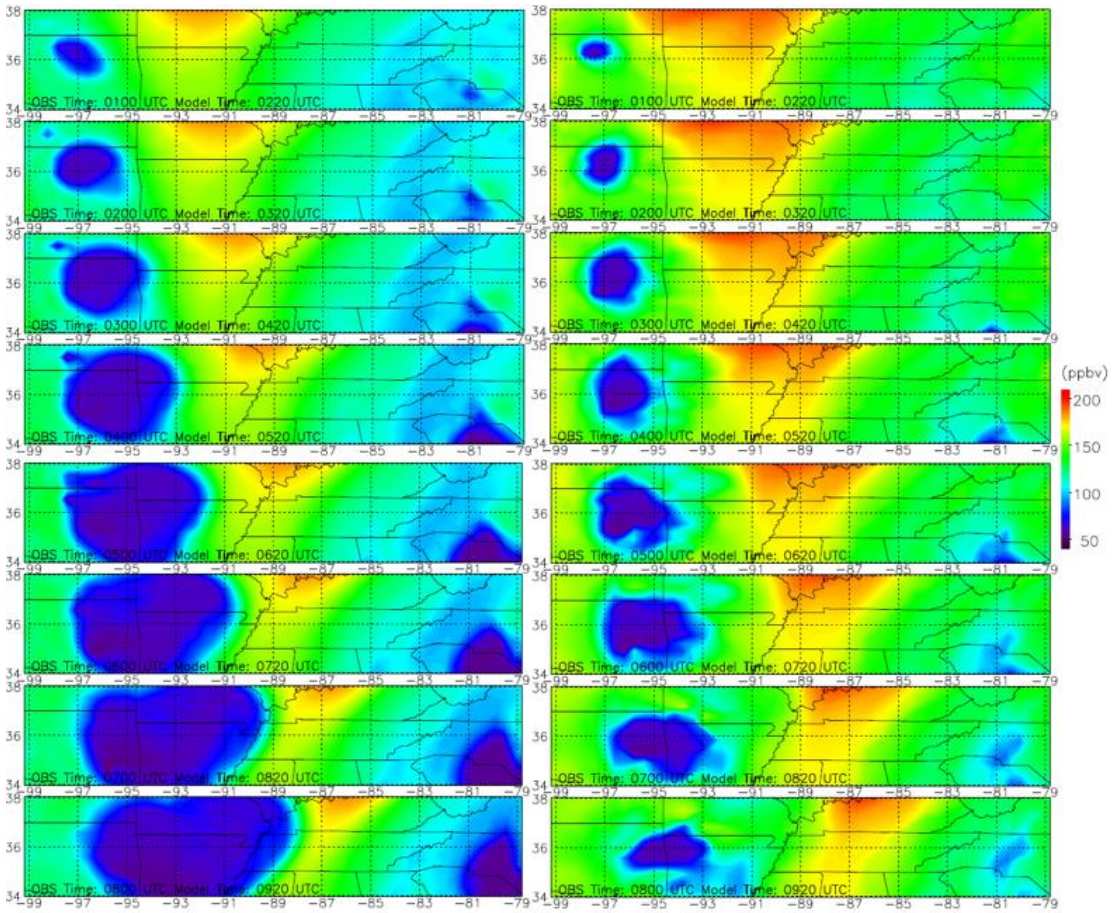

Figure 6.5 Hourly ozone simulation at 11 km from 0100 UTC to 0800 UTC (model time: 0220 UTC to 0920 UTC) 30 May at 11 km (left); and ozone simulation at 11.4 (right).

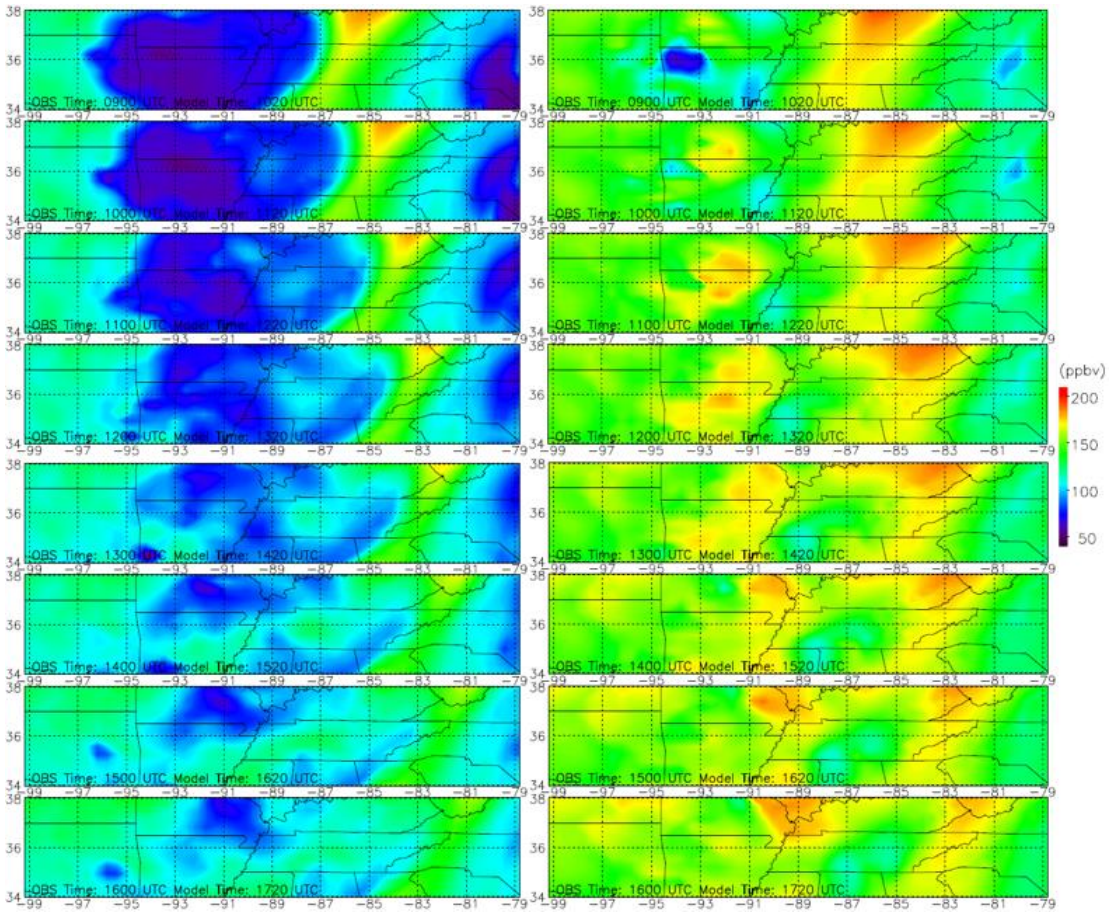

Figure 6.6 Similar to Figure 6.5, but from 0900 UTC to 1600 UTC 30 May (model time: 1020 UTC to 1720 UTC).

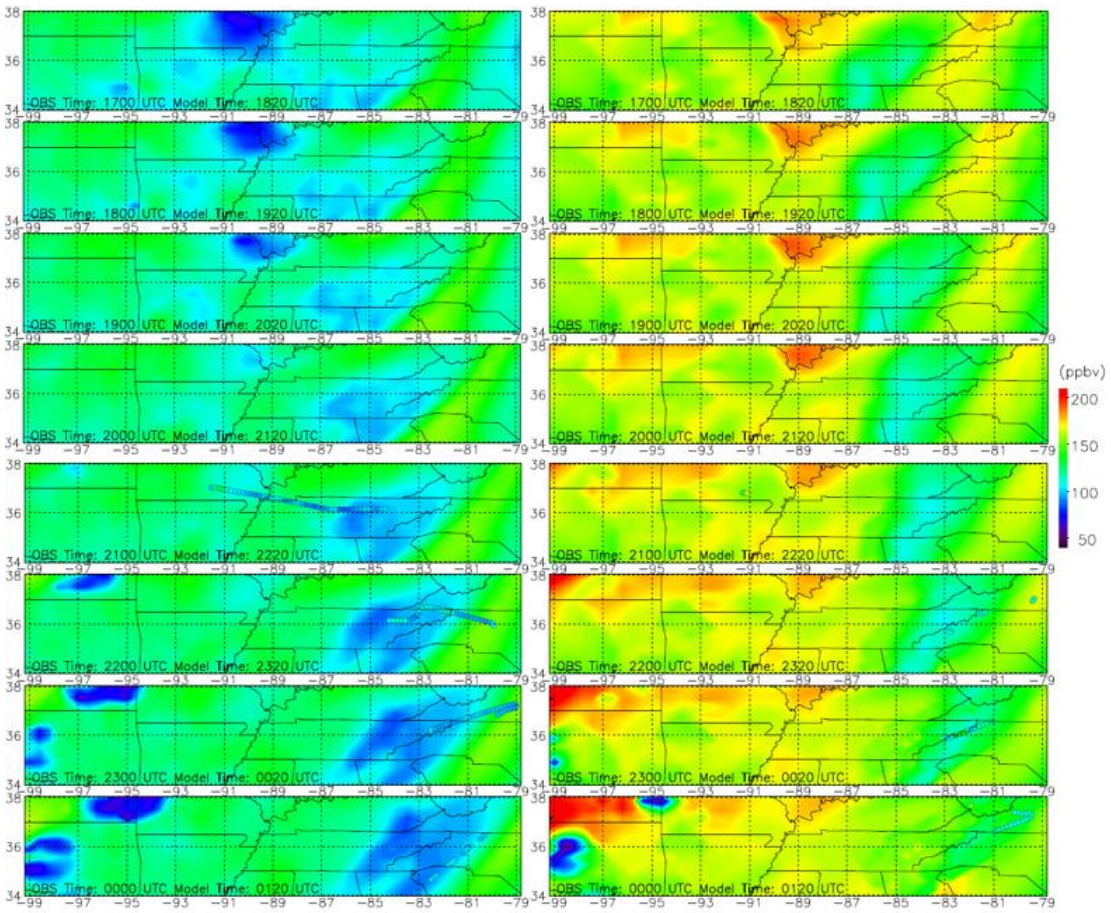

Figure 6.7 Similar to Figure 6.5, but from 1700 UTC 30 May to 0000 UTC 31 May (model time: 1820 UTC 30 May to 0120 UTC 31 May) with DC-8 measurements (circles, left); and with GV measurements (circles, right). The aircraft measuring time was between 80-140 min before the model plotting time.

I calculated the simulated mean ozone mixing ratio in the downwind outflow region at 0000 UTC 31 May along the aircraft flight track (Table 6.1). The storm downwind outflow region was defined as the region where NO_x >0.5 ppbv. The simulated mean ozone mixing ratios in that region were similar to the observations (Table 6.1). The simulated mean ozone mixing ratio at 11 km was 97.0 ppbv (7 % lower than the observation), and 113.3 ppbv (2 % higher than the observation) at 11.4 km. Therefore, the simulated average ozone increase was 17.2 ppbv at the DC8 measuring

level and 34.2 ppbv at the GV measuring level. The simulated increase was very close to the observed increase at 11.4 km, but 34% smaller than observed at 11 km. However, not all of the increase was caused by photochemical production. Some of the increase could be due to mixing of larger ozone values (e.g. there was a stratospheric intrusion of large ozone values out ahead of the convective outflow plume) from areas surrounding the low ozone plume as it moved downwind. In Figure 6.5, before sunrise time (approximately 1030 UTC on 30 May), the low ozone region started to shrink between 0800 UTC and 1000 UTC at the GV measuring height, which suggests that the ozone increase was due to mixing during this period. After sunrise, ozone rapidly increased in this air mass due to photochemical production. Considering this, I calculated the 24-hour net ozone production between 0000 UTC May 30 (model time: 0120 UTC May 30) and 0000 UTC May 31 (model time: 0120 UTC May 31) at all grid points in the downwind region of the flights, by adding the ozone production at each time step beginning at 0000 UTC (model time: 0120 UTC) to the model as a tracer. Results are shown in Figure 6.8 and Table 6.1. The simulated net ozone production was 10.7 ppbv/day (62% of the total simulated ozone change) at the DC8 measuring height, and 5.5 ppbv/day (16% of the total simulated ozone change) at GV measuring height. Thus, at the DC8 measuring height, the net ozone production dominated the ozone change, while at the GV measuring height, the mixing of larger ozone values dominated the ozone change. Compared to the net ozone production results from the previous studies (7-15 ppbv/day), the simulated net ozone production at DC8 measuring height was within the range, while the net ozone production at GV measuring height was smaller than the results from the previous studies.

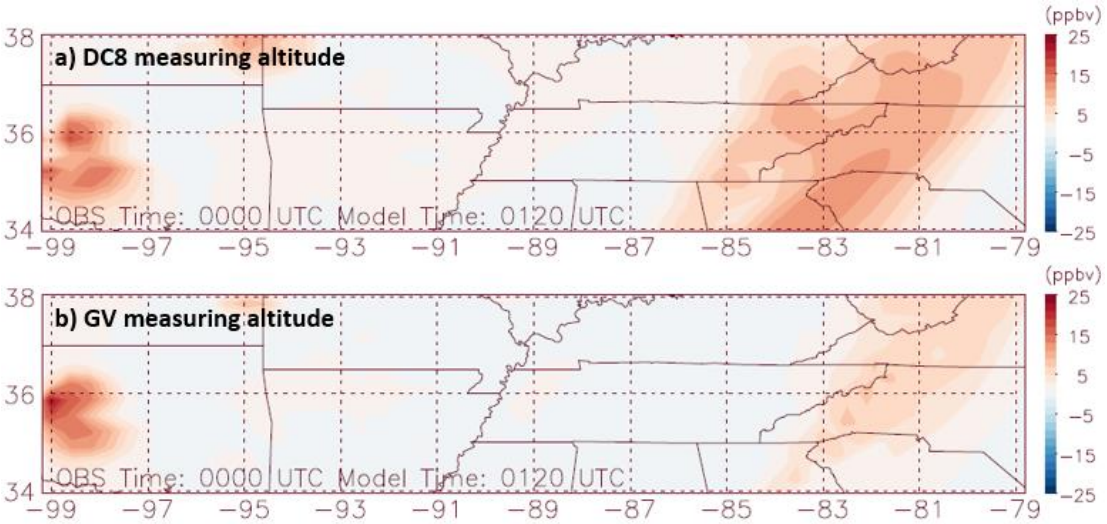

Figure 6.8 24-hour net ozone production between 0000 UTC May 30 (model time: 0120 UTC) and 0000 UTC May 31 (model time: 0120 UTC) in air arriving at map locations at DC8 measuring altitude (a) and GV measuring altitude (b).

6.3 Influence of Ice Retention Factor on Ozone Production

In this section, we conducted 4 sensitivity runs and compared the results with the simulation in section 6.2 (control run). The four sensitivity runs include (Table 6.2): (1) without wet scavenging (No Scav); (2) ice retention factor (r) equals 1 (r=1); (3) using ice retention factor based on laboratory measurements (Leriche et al., 2013); (4) using ice retention factor based on Bela et al. (2016a, 2018).

Table 6.2 Ice retention factors for control run and each sensitive run

	CH_2O	CH_3OOH	H_2O_2	HNO_3	SO_2
Control	*0*	*0*	*0.1*	*1*	*0.02*
No scav.	*0*	*0*	*0*	*0*	*0*
r=1	*1*	*1*	*1*	*1*	*1*
r=lab	*0.64*	*0.02*	*0.64*	*1*	*0.02*
r=Bela	*0*	*1*	*0.1*	*1*	*1*

Figure 6.9 shows the downwind ozone mixing ratio differences between the control run and each sensitivity run, with positive (negative) values meaning larger

(smaller) than the control run. Without turning on the wet scavenging, the model overestimates the ozone production during transport to the downwind region. When setting the ice retention factor as 1 (all species stay in ice, as in the standard WRF-Chem), the downwind ozone production was underestimated. Comparing the results of each sensitivity run, I found that the downwind ozone production is very sensitive to the choice of ice retention factors for the soluble species.

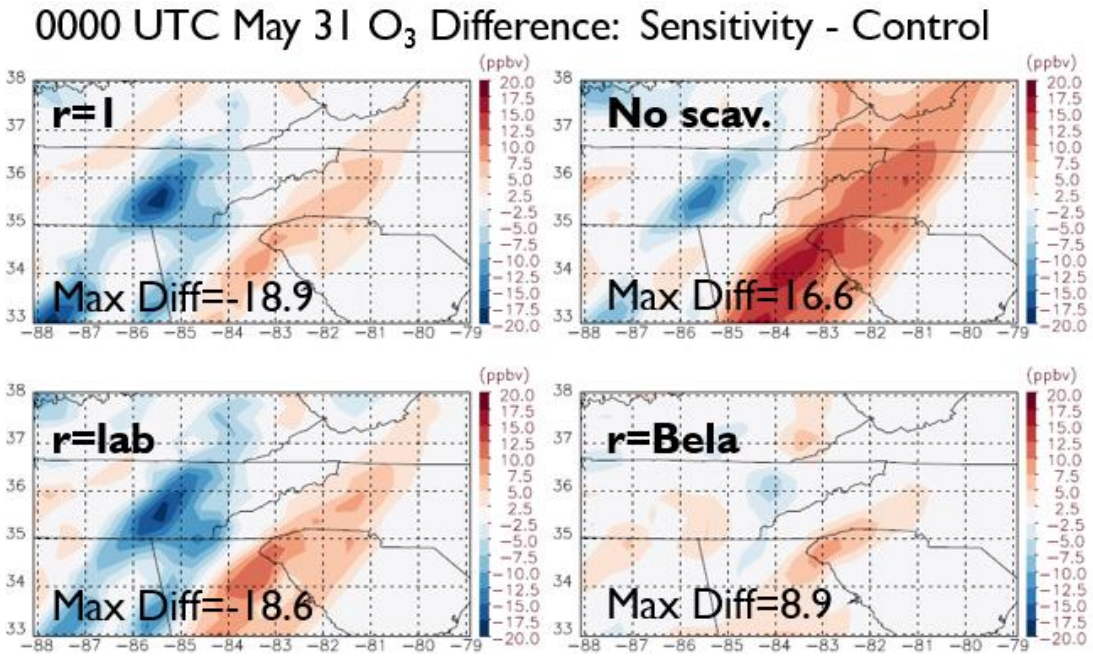

Figure 6.9 The ozone mixing ratio differences between each sensitivity run and control run.

6.4 Summary

In this chapter, we examine the downwind ozone mixing ratio evolution. The model well reproduces the convective transport of ozone and the downwind ozone transport and production. When the storm was active, the UT ozone mixing ratio was reduced due to the vertical transport of low ozone PBL air to the UT. During the

nighttime, UT ozone kept decaying. After sunrise, the ozone mixing ratio increased rapidly, which resulted from the photochemical reactions. The aircraft measured mean ozone mixing ratio increased 25.9 ppbv at DC8 measuring height, and 30.6 at GV measuring height in the downwind outflow region compared with the anvil region. The average ozone increase in the model was 17.2 ppbv at DC8 measuring level and 34.2 ppbv at GV measuring level. The simulated net ozone production was 10.7 ppbv/day (62% of the total simulated ozone change) at DC8 measuring height, and 5.5 ppbv/day (16% of the total simulated ozone change) at GV measuring height. Thus, at DC8 measuring height, the net ozone production dominated the ozone change, while at GV measuring height, the mixing of larger ozone values dominated the ozone change. Compared to the net ozone production results from the previous studies (7-15 ppbv/day), the simulated net ozone production at DC8 measuring height was within the range, while the net ozone production at GV measuring height was lower than the results from the previous studies.

Moreover, we explored the sensitivity of the ice retention factors on the downwind ozone production simulation. The results of the sensitivity tests showed that the downwind ozone production is very sensitive to the choice of ice retention factors for the soluble species.

Chapter 7 : Conclusions and Recommendations for Future Research

7.1 Conclusions

Deep convective transport of surface moisture and pollution from the planetary boundary layer to the upper troposphere and lower stratosphere affects the radiation budget and climate. The first part of my Ph.D. research analyzed the deep convective transport in three different convective regimes from the 2012 Deep Convective Clouds and Chemistry field campaign: 21 May Alabama air mass thunderstorms, 29 May Oklahoma supercell severe storm, and 11 June MCS. There was not a single set of model configuration and IC/BC that led to satisfactory simulations of all three cases. Each case required its own set of model specifications to obtain the best possible simulation. Lightning data assimilation within the WRF-Chem is utilized to improve the simulations of storm location, vertical structure, and chemical fields. Analysis of vertical flux divergence shows that deep convective transport in the 29 May supercell case is the strongest per unit area, while transport of boundary layer insoluble trace gases is relatively weak in the MCS and airmass cases. The weak deep convective transport in the strong MCS is unexpected and is caused by the injection into low-levels of midlevel clean air by a strong rear inflow jet. In each system, the magnitude of tracer vertical transport is more closely related to the vertical distribution of mass flux density than the vertical distribution of trace gas mixing ratio. Finally, the net vertical transport is strongest in high composite reflectivity regions and dominated by upward transport.

In the second part, I used cloud parameterized WRF-Chem simulations to analyze the subgrid deep convective transport of CO at 12 km and 36 km horizontal resolution in the same DC3 supercell and mesoscale convective systems, and I compare the simulation results with aircraft measurements and cloud resolved simulations. The best WRF simulations of these storms in terms of precipitation were obtained with use of the Grell-Freitas (GF) convective scheme. The default WRF-Chem subgrid convective transport scheme was replaced with a scheme to compute convective transport within the GF subgrid cumulus parameterization, which resulted in more realistic vertical distributions of modeled trace gases, especially in the 36 km resolution domain. I examined the CO tendencies due to subgrid and grid scale convective transport. Results showed that the subgrid convective transport started earlier than the grid scale convective transport. The subgrid scale convective transport reached its maximum at the time when the grid scale convection started to form a continuous constant-altitude detrainment layer. After that, both the subgrid and grid scale convective transport began to decrease. The subgrid scale convective transport played a more significant role in the supercell case than the MCS case. Subgrid contribution reached ~90 % at the beginning of the storm, and decreased to ~ 30 % (17 %) for the 36 km (12 km) domain 4 hours later.

In the third part of my research, I improved the simulation of WRF-Chem subgrid wet scavenging by introducing the ice retention factor and adjusting the conversion rate of cloud water to ice water. Simulation results showed that the original WRF-Chem wet scavenging scheme removed too much CH_2O, CH_3OOH and H_2O_2 in

the UT, and overestimated the HNO_3 mixing ratio in the cloud outflow region. The introduction of the ice retention factor improves the model simulation of CH_2O, CH_3OOH and H_2O_2, the wet scavenging efficiencies of which were overestimated in the original WRF-Chem run. The differences between observation and simulation were reduced by 26%, 37%, and 16% for CH_2O, CH_3OOH and H_2O, when using r=0. The usage of the new conversion rate of cloud water to rain water provided an additional improvement of CH_2O, CH_3OOH by increasing CH_2O by 12 % and increasing CH_3OOH by 63%. However, the simulated CH_2O was still much lower (60%) than the observation, and the simulated HNO_3 was still higher (1.38 times greater) than the observation. The SE analysis demonstrated that all the wet scavenging runs underestimated the SE of HNO_3, and overestimated the SE of CH_2O. Based on all the results in section 5.3.2 and section 5.3.3, we concluded that the best simulation is using the new conversion rate of cloud water to rain water, and using ice retention factor for soluble species. The best estimate of the ice retention factors are: r=0 for CH_2O and CH_3OOH, r=0.1 for H_2O_2, r=1 for HNO_3. The SO_2 simulation did not respond to the change of ice retention factor, so we suggest the value from the laboratory results, which is 0.02. Our best estimates of the ice retention factors for CH_2O and H_2O_2 are lower than Leriche et al. (2013), but similar for CH_3OOH. Compared to the best estimate from Bela et al. (2016), which were based on the cloud resolved simulation, our results are close to their results except for CH_3OOH (their best estimate was 1).

In the fourth part, I examined the downwind ozone mixing ratio evolution. The model well reproduced the convective transport of ozone and the downwind ozone

transport and production. When the storm was active, the UT ozone mixing ratio was reduced due to the vertical transport of low ozone PBL air to the UT. During the nighttime, the plume of UT ozone kept decaying. After sunrise, the ozone mixing ratio increased rapidly, which resulted from the photochemical reactions. The aircraft measured mean ozone mixing ratio increased 25.9 ppbv at DC8 measuring height, and 30.6 at GV measuring height in the downwind outflow region compared with the anvil region. The average ozone increase in the model was 17.2 ppbv at DC8 measuring level and 34.2 ppbv at GV measuring level. The simulated net ozone production was 10.7 ppbv/day (62% of the total simulated ozone change) at DC8 measuring height, and 5.5 ppbv/day (16% of the total simulated ozone change) at GV measuring height. Thus, at DC8 measuring height, the net ozone production dominated the ozone change, while at GV measuring height, the mixing of larger ozone values dominated the ozone change. Compared to the net ozone production results from the previous studies (7-15 ppbv/day), the simulated net ozone production at DC8 measuring height was within the range, while the net ozone production at GV measuring height was lower than the results from the previous studies.

Moreover, I explored the sensitivity of the ice retention factors on the downwind ozone production simulation. The results of the sensitivity tests showed that the downwind ozone production is very sensitive to the choice of ice retention factors for the soluble species.

7.2 Future Work

7.2.1 Deep Convective Transport

A detailed investigation of deep convective transport in different convective regimes is fundamental to understanding how deep convective transport influences the radiation budget and climate of the Earth. We have examined convective transport for case studies representing three types of convection. Quantifying the relative frequency of these types of convection and others using data from satellites and other sources is an active area of research [e.g., Machado and Rossow, 1993; Tan et al., 2013; Tselioudis et al., 2013; Cotton et al., 1995]. However, comprehensive studies with detailed storm classification of the global frequencies of different convective regimes are lacking. For example, studies showing detailed classifications of storms (i.e., squall lines with different stratiform rain patterns, bow echo, supercell, multicell, isolated cells, and broken line) are needed. In addition, studies with a detailed classification of convective regimes [e.g., Gallus et al., 2008; Schoen and Ashley, 2010] need to be expanded to include additional regions. Comprehensive studies to determine these frequencies are lacking, but this is recommended as an area of future work. Next, it would be interesting to examine the deep convective transport of other trace gases, water vapor, and aerosol in different convective regimes.

7.2.2 Cloud Parameterized Convective Transport

According to the results in Chapter 4, in order to obtain reasonable simulations of the impact of convection on tropospheric composition, subgrid convective transport

needs to be computed in a manner consistent with the subgrid convection in the driving meteorological model. This is true regardless of whether the chemical transport is computed online with the meteorology or in an offline manner. If cumulus schemes other than GF are used, the convective transport needs to be performed consistently with those schemes. Thus, more work needs to be done on writing the module of subgrid scale convective transport of trace gases for different cumulus parameterizations.

7.2.3 Cloud Parameterized Wet Scavenging

Based on the results in Chapter 6, downwind ozone production is very sensitive to the choice of ice retention factors of some soluble species. In order to have a better estimation of the ice retention efficiency, there is great need to obtain a good simulation of the cloud ice in the cumulus parameterizations. However, most of the cumulus parametrizations do not have the cloud ice simulation. Thus, more efforts need to be put into the work of adding ice physics in the cumulus schemes. Also, we need to do more sensitivity tests to estimate the ice retention for different convective regimes.

Bibliography

Anderson, D. C., Loughner, C. P., Diskin, G., Weinheimer, A., Canty, T. P., Salawitch, R. J., Worden, H. M., Fried, A., Mikoviny, T., Wisthaler, A., et al. (2014). Measured and modeled CO and NO_y in DISCOVER-AQ: An evaluation of emissions and chemistry over the eastern US. *Atmospheric Environment* 96, 78–87.

Allen, D. J., Pickering, K. E., Duncan, B. and Damon, M. (2010), Impact of lightning NO emissions on North American photochemistry as determined using the Global Modeling Initiative (GMI) model, *J. Geophys. Res*., 115, D22301, doi:10.1029/2010JD014062.

Allen, D.J., Pickering, K.E., Pinder, R.W., Henderson, B.H., Appel, K.W., and Prados, A. (2012). Impact of lightning-NO on eastern United States photochemistry during the summer of 2006 as determined using the CMAQ model. *Atmos. Chem. Phys.* 12, 1737–1758.

Apel, E. C., Hornbrook, R. S., Hills, A. J., Blake, N. J., Barth, M. C., Weinheimer, A., Cantrell, C., Rutledge, S. A., Basarab, B., Crawford, J., et al. (2015). Upper tropospheric ozone production from lightning NOx-impacted convection: Smoke ingestion case study from the DC3 campaign. *J. Geophys. Res. Atmos*. *120*, 2014JD022121.

Arakawa, A., and Schubert, W. H. (1974). Interaction of a Cumulus Cloud Ensemble with the Large-Scale Environment, Part I. *J. Atmos. Sci.* 31, 674–701.

Barth, M. C., Kim, S.-W., Skamarock, W. C., Stuart, A. L., Pickering, K. E., and Ott, L. E. (2007a). Simulations of the redistribution of formaldehyde, formic acid, and peroxides in the 10 July 1996 Stratospheric-Tropospheric Experiment: Radiation, Aerosols, and Ozone deep convection storm, *J. Geophys. Res*., 112, D13310, doi:10.1029/2006JD008046.

Barth, M. C., Kim, S. -W., Wang, C., Pickering, K. E., Ott, L. E., Stenchikov, G., Leriche, M., Cautenet, S., Pinty, J. -P., Barthe, C., et al. (2007b). Cloud-scale

model intercomparison of chemical constituent transport in deep convection. *Atmos. Chem. Phys. 7*, 4709–4731.

Barth, M. C., Lee, J., Hodzic, A., Pfister, G., Skamarock, W. C., Worden, J., Wong, J., and Noone, D. (2012). Thunderstorms and upper troposphere chemistry during the early stages of the 2006 North American Monsoon. *Atmos. Chem. Phys. 12*, 11003–11026.

Barth, M. C., Cantrell, C. A., Brune, W. H., Rutledge, S. A., Crawford, J. H., Huntrieser, H., Carey, L. D., MacGorman, D., Weisman, M., Pickering, K. E., et al. (2015). The Deep Convective Clouds and Chemistry (DC3) Field Campaign. *Bull. Amer. Meteor. Soc. 96*, 1281–1309.

Baughcum, S., Begin, J., Franco, F., Greene, D., Lee, D., McLaren, M. -L., Mortlock, A., Newton, P., Schmitt, A., Sutkus, D., et al. (1999). Aircraft Emissions: Current Inventories and Future Scenarios. *Scholarship at Penn Libraries*.

Beirle, S., et al. (2006), Estimating the NO_X produced by lightning from GOME and NLDN data: A case study in the Gulf of Mexico, *Atmos. Chem. Phys.*, 6, 1075–1089.

Beirle, S., H. Huntrieser, and T. Wagner (2010), Direct satellite observation of lightning-produced NO_X, *Atmos. Chem. Phys.*, 10, 10,965–10,986, doi:10.5194/acp-10-10965-2010.

Bela, M. M., Barth, M. C., Toon, O. B., Fried, A., Homeyer, C. R., Morrison, H., Cummings, K. A., Li, Y., Pickering, K. E., Allen, D. J., et al. (2016aBela). Wet scavenging of soluble gases in DC3 deep convective storms using WRF-Chem simulations and aircraft observations. *J. Geophys. Res. Atmos. 121*, 2015JD024623.

Bela, Megan M., "Cloud and Biomass Burning Effects on the Abundance of Ozone and Its Precursors over the Amazon Basin and Central and Southeast U.S" (2016b). Atmospheric & Oceanic Sciences Graduate Theses & Dissertations. 66.

Bela, M.M., Barth, M.C., Toon, O.B., Fried, A., Ziegler, C., Cummings, K. A., Li, Y., et al. (2018). Effects of microphysical scavenging, entrainment, and aqueous

chemistry on wet removal of formaldehyde and peroxides in deep convection observed over the central U.S. *J. Geophys. Res*. Atmos. Under review.

Bertram, T. H., Perring, A. E., Wooldridge, P. J., Crounse, J. D., Kwan, A. J., Wennberg, P. O., Scheuer, E., Dibb, J., Avery, M., Sachse, G., et al. (2007). Direct Measurements of the Convective Recycling of the Upper Troposphere. *Science 315*, 816–820.

Bigelbach, B. C., Mullendore, G. L., and Starzec, M. (2014). Differences in deep convective transport characteristics between quasi-isolated strong convection and mesoscale convective systems using seasonal WRF simulations. *J. Geophys. Res. Atmos*. *119*, 11,445-11,455.

Biggerstaff, M. I., Wicker, L. J., Guynes, J., Ziegler, C., Straka, J. M., Rasmussen, E. N., Dogget IV, A., Carey, L. D., Schroeder, J. L., and Weiss, C. (2005). The Shared Mobile Atmospheric Research and Teaching (SMART) Radar: A collaboration to enhance research and teaching. *Bull. Amer. Meteor. Soc.*, **86**, 1263-1274, doi: 10.1175/BAMS-86-9-1263.

Brown, J. M. (1979). Mesoscale Unsaturated Downdrafts Driven by Rainfall Evaporation: A Numerical Study. *J. Atmos. Sci.* 36, 313–338.

Bucsela, E. J., et al. (2010), Lightning-generated NO_X seen by the Ozone Monitoring Instrument during NASA's Tropical Composition, Cloud and Climate Coupling Experiment (TC4), *J. Geophys. Res.*, 115, D00J10, doi:10.1029/2009JD013118.

Carlton, A. G., Turpin, B. J., Altieri, K. E., Seitzinger, S., Reff, A., Lim, H.-J., and Ervens, B. (2007), Atmospheric oxalic acid and SOA production from glyoxal: Results of aqueous photooxidation experiments, *Atmos. Environ.*, 41(35), 7588–7602, doi:10.1016/j.atmosenv.2007.05.035.

Chatfield, R. B., and Crutzen, P. J. (1984). Sulfur dioxide in remote oceanic air: Cloud transport of reactive precursors. *J. Geophys. Res.* 89, 7111–7132.

Chin, M., Ginoux, P., Kinne, S., Torres, O., Holben, B.N., Duncan, B.N., Martin, R.V., Logan, J.A., Higurashi, A., and Nakajima, T. (2002). Tropospheric Aerosol Optical Thickness from the GOCART Model and Comparisons with Satellite and

Sun Photometer Measurements. *J. Atmos. Sci. 59*, 461–483.

Chen, G., Langley Research Center (LaRC), NASA, and J. Olson (2014a), NSF/NCAR GV HIAPER 1 Minute Data Merge. Version 1.0. UCAR/NCAR-Earth Observing Laboratory. [Available https://data.eol.ucar.edu/dataset/353.196.]

Chen, G., Langley Research Center (LaRC), NASA, and J. Olson (2014b), NSF/NCAR GV HIAPER 1 Second Data Merge. Version 1.0. UCAR/NCAR-Earth Observing Laboratory. [Available https://data.eol.ucar.edu/dataset/353.194.]

Chen, G., Langley Research Center (LaRC), NASA, Olson, J. 2016. NASA DC-8 1 Minute Data Merge, Version 4.0. UCAR/NCAR - Earth Observing Laboratory. http://data.eol.ucar.edu/dataset/353.192.

Chen, G., Langley Research Center (LaRC), NASA, Olson, J. 2016. NASA DC-8 1 Second Data Merge, Version 4.0. UCAR/NCAR - Earth Observing Laboratory. http://data.eol.ucar.edu/dataset/353.189.

Clyne, J. and Rast, M. (2005). A prototype discovery environment for analyzing and visualizing terascale turbulent fluid flow simulations, *SPIE-IS&T Electronic Imaging, 5669*, 284-294.

Clyne, J., Mininni, P., Norton, A., and Rast, M. (2007). Interactive desktop analysis of high resolution simulations: application to turbulent plume dynamics and current sheet formation, *New Journal of Physics*, *9*, 301.

Cummings, K. A. (2017). An Investigation of the Parameterized Prediction of Lightning in Cloud-Resolved Convection and the Resulting Chemistry, (Doctoral dissertation). Retrieved from DRUM. (http://hdl.handle.net/1903/19920). College Park, MD: University of Maryland.

Dickerson, R. R., Huffman, G. J., Luke, W. T., Nunnermacker, L. J., Pickering, K. E., Leslie, A. C. D., Lindsey, C. G., Slinn, W. G. N., Kelly, T. J., Daum, P. H., Delany, A. C., Greenberg, J. P., Zimmerman, P. R., Boatman, J. G., Ray, J. D., and Stedman, D. H. (1987). Thunderstorms: an important mechanism in the transport of air pollutants, *Science*, *235*:460-465.

DiGangi, E. A., MacGorman, D. R., Ziegler, C. L., Betten, D., Biggerstaff, M., Bowlan, M., and Potvin, C. (2016). An overview of the 29 May 2012 Kingfisher supercell during DC3. *J. Geophys. Res. Atmos*. 2016JD025690.

Doswell III, C. A. (2001). Severe convective storms – an overview, chapter in *Severe Convective Storms*, C. A. Doswell III editor, American Meteorological Society, Boston, MA.

Emmons, L. K., Walters, S., Hess, P. G., Lamarque, J.-F., Pfister, G. G., Fillmore, D., Granier, C., Guenther, A., Kinnison, D., Laepple, T., et al. (2010). Description and evaluation of the Model for Ozone and Related chemical Tracers, version 4 (MOZART-4). *Geosci. Model Dev*. *3*, 43–67.

ENTLN, 2012: Total Lightning Network. [Available online at http://www.earthnetworks.com/Products/TotalLightningNetwork.aspx.]

Fast, J. D., Gustafson, W. I., Easter, R. C., Zaveri, R. A., Barnard, J. C., Chapman, E. G., Grell, G. A., and Peckham, S. E. (2006). Evolution of ozone, particulates, and aerosol direct radiative forcing in the vicinity of Houston using a fully coupled meteorology-chemistry-aerosol model. *J. Geophys. Res. 111*, D21305.

Fierro, A. O., Mansell, E. R., Ziegler, C. L., and MacGorman, D. R. (2012). Application of a Lightning Data Assimilation Technique in the WRF-ARW Model at Cloud-Resolving Scales for the Tornado Outbreak of 24 May 2011. *Mon. Wea. Rev. 140*, 2609–2627.

Fierro, A. O., Gao, J., Ziegler, C. L., Mansell, E. R., MacGorman, D. R., and Dembek, S. R. (2014). Evaluation of a Cloud-Scale Lightning Data Assimilation Technique and a 3DVAR Method for the Analysis and Short-Term Forecast of the 29 June 2012 Derecho Event. *Mon. Wea. Rev.* 142, 183–202.

Fierro, A. O., Clark, A. J., Mansell, E. R., MacGorman, D. R., Dembek, S. R., and Ziegler, C. L. (2015). Impact of Storm-Scale Lightning Data Assimilation on WRF-ARW Precipitation Forecasts during the 2013 Warm Season over the Contiguous United States. *Mon. Wea. Rev*. *143*, 757–777.

Fierro, A. O., Gao, J., Ziegler, C. L., Calhoun, K. M., Mansell, E. R., and MacGorman,

D. R. (2016). Assimilation of Flash Extent Data in the Variational Framework at Convection-Allowing Scales: Proof-of-Concept and Evaluation for the Short-Term Forecast of the 24 May 2011 Tornado Outbreak. *Mon. Wea. Rev. 144*, 4373–4393.

Frank, W. M., & Cohen, C. (1987). Simulation of Tropical Convective Systems. Part I: A Cumulus Parameterization. *J. Atmos. Sci.* 44, 3787–3799.

Freitas, S., Dias, M., and Silva Dias, P. (2000). Modeling the convective transport of trace gases by deep and moist convection. *Hybrid Methods in Engineering* 2, 315–328.

Fried, A., Barth, M. C., Bela, M., Weibring, P., Richter, D., Walega, J., Li, Y., Pickering, K., Apel, E., Hornbrook, R., et al. (2016). Convective transport of formaldehyde to the upper troposphere and lower stratosphere and associated scavenging in thunderstorms over the central United States during the 2012 DC3 study. *J. Geophys. Res. Atmos*. *121*, 2015JD024477.

Grassian, V. H. (2005*), Environmental Catalysis*, CRC Press, Boca Raton, Fla.

Grell, G. A. (1993). Prognostic Evaluation of Assumptions Used by Cumulus Parameterizations. *Mon. Wea. Rev*. *121*, 764-787.

Grell, G. A., and Devenyi, D. (2002). A generalized approach to parameterizing convection combining ensemble and data assimilation techniques. *Geophys. Res. Lett.* 29, 2002GL015311.

Grell, G. A., Peckham, S. E., Schmitz, R., McKeen, S. A., Frost, G., Skamarock, W. C., and Eder, B. (2005). Fully coupled "online" chemistry within the WRF model. *Atmospheric Environment 39*, 6957–6975.

Grell, G. A., and Freitas, S. R. (2014). A scale and aerosol aware stochastic convective parameterization for weather and air quality modeling. *Atmos. Chem. Phys. 14*, 5233–5250.

Guenther, A., Karl, T., Harley, P., Wiedinmyer, C., Palmer, P. I., and Geron, C. (2006). Estimates of global terrestrial isoprene emissions using MEGAN (Model of

Emissions of Gases and Aerosols from Nature). *Atmos. Chem. Phys*. *6*, 3181–3210.

Halland, J. J., Fuelberg, H. E., Pickering, K. E., and Luo, M. (2009). Identifying convective transport of carbon monoxide by comparing remotely sensed observations from TES with cloud modeling simulations. *Atmos. Chem. Phys*. *9*, 4279–4294.

Hill, J. D., Pilkey, J., Uman, M. A., Jordan, D. M., Rison, W., Krehbiel, P.R., Biggerstaff, M. I., Hyland, P. and Blakeslee, R. (2013). Correlated lightning mapping array and radar observations of the initial stages of three sequentially triggered Florida lightning discharges. *J. Geophys. Res. Atmos.*, 118, 8460-8481, doi:10.1002/jgrd.50660.

Homeyer, C. R., Pan, L. L., Dorsi, S. W., Avallone, L. M., Weinheimer, A. J., O'Brien, A. S., DiGangi, J. P., Zondlo, M. A., Ryerson, T. B., Diskin, G. S., et al. (2014). Convective transport of water vapor into the lower stratosphere observed during double-tropopause events. *J. Geophys. Res. Atmos. 119*, 10,941-10,958.

Hong, S.-Y., and Lim, J.-O. J. (2006). The WRF single-moment microphysics scheme (WSM6), *J. Korean Meteorol. Soc*., 42, 129–151.

Hong, S.-Y., Noh, Y., and Dudhia, J. (2006). A New Vertical Diffusion Package with an Explicit Treatment of Entrainment Processes. *Mon. Wea. Rev*. *134*, 2318–2341.

Houze, R. A., Rutledge, S. A., Biggerstaff, M. I., and Smull, B. F. (1989). Interpretation of Doppler Weather Radar Displays of Midlatitude Mesoscale Convective Systems. *Bull. Amer. Meteor. Soc*., *70*, 608-619.

Huntrieser, H., U. Schumann, H. Schlager, H. Höller, A. Giez, H.-D. Betz, D. Brunner, C. Forster, O. Pinto Jr., and R. Calheiros (2008), Lightning activity in Brazilian thunderstorms during TROCCINOX: Implications for NO_X production, *Atmos. Chem. Phys*., 8, 921–953.

Huntrieser, H., et al. (2009), NO_X production by lightning in Hector: First airborne measurements during SCOUT-O_3/ACTIVE, *Atmos. Chem. Phys.,* 9, 8377–8412.

Huntrieser, H., H. Schlager,M. Lichtenstern, P. Stock, T. Hamburger, H. Höller, K. Schmidt, H.-D. Betz, A. Ulanovsky, and F. Ravengnani (2011), Mesoscale convective systems observed during AMMA and their impact on the NO_X and O_3 budget over West Africa, *Atmos. Chem. Phys*., 11, 2503–2536.

Huntrieser, H., Lichtenstern, M., Scheibe, M., Aufmhoff, H., Schlager, H., Pucik, T., Minikin, A., Weinzierl, B., Heimerl, K., Fütterer, D., et al. (2016). On the origin of pronounced O_3 gradients in the thunderstorm outflow region during DC3. *J. Geophys. Res. Atmos. 121*, 2015JD024279.

Iacono, M. J., Delamere, J. S., Mlawer, E. J., Shephard, M. W., Clough, S. A., and Collins, W. D. (2008). Radiative forcing by long-lived greenhouse gases: Calculations with the AER radiative transfer models. *J. Geophys. Res. 113*, D13103.

Intergovernmental Panel on Climate Change (2013), Climate Change 2013: The Physical Science Basis, *in Contribution of Working Group I to the Fifth Assessment Report of the Intergovernmental Panel on Climate Change*, edited by T. F. Stocker, et al., 1535 pp., Cambridge Univ. Press, Cambridge, U. K., and New York.

Iribarne, J. V., and Pyshnov, T. (1990). The effect of freezing on the composition of supercooled droplets—I. Retention of HCl, HNO_3, NH_3 and H_2O_2. *Atmospheric Environment. Part A. General Topics* 24, 383–387.

Iribarne, J. V., Pyshnov, T., and Naik, B. (1990). The effect of freezing on the composition of supercooled droplets—II. Retention of S (IV). Atmospheric Environment. *Part A. General Topics* 24, 389–398.

Janjić, Z.I. (1994). The Step-Mountain Eta Coordinate Model: Further Developments of the Convection, Viscous Sublayer, and Turbulence Closure Schemes. *Mon. Wea. Rev.* 122, 927–945.

Jensen, E.J., Pfister, L., Ueyama, R., Bergman, J.W., and Kinnison, D. (2015). Investigation of the transport processes controlling the geographic distribution of carbon monoxide at the tropical tropopause. *J. Geophys. Res. Atmos. 120*,

2014JD022661.

Jung, E., Shao, Y., and Sakai, T. (2005). A study on the effects of convective transport on regional-scale Asian dust storms in 2002. *J. Geophys. Res*. *110*, D20201.

Kain, J. S., & Fritsch, J. M. (1993) Convective Parameterization for Mesoscale Models: The Kain-Fritsch Scheme. In: Emanuel K.A., Raymond D.J. (eds) *The Representation of Cumulus Convection in Numerical Models.* Meteorological Monographs. American Meteorological Society, Boston, MA

Kain, J. S. (2004). The Kain–Fritsch Convective Parameterization: An Update. J. *Appl. Meteor*. 43, 170–181.

Kong, F. & Qin, Y. (1993). The vertical transport of air pollutants by convective clouds. Part I: A non-reactive cloud transport model. *Adv. Atmos. Sci*. 10, 415–427.

Kong, F. & Qin, Y. (1994a). The vertical transport of air pollutants by convective clouds Part II: Transport of soluble gases and sensitivity tests. *Adv. Atmos. Sci*. 11, 1–12.

Kong, F. & Qin, Y. (1994b). The vertical transport of air pollutants by convective clouds. Part III: Transport features of different cloud systems. *Adv. Atmos. Sci*. 11, 13–26.

Koren, V., Schaake, J., Mitchell, K., Duan, Q.-Y., Chen, F., and Baker, J. M. (1999). A parameterization of snowpack and frozen ground intended for NCEP weather and climate models. *J. Geophys. Res*. 104, 19569–19585.

Koshak, W. (2014), Global Lightning Nitrogen Oxides Production, *in The Lightning Flash, 2nd ed., edited by V. Cooray*, chap. 19, 928 pp.

Krishnamurti, T. N., Low-Nam, S., and Pasch, R. (1983). Cumulus Parameterization and Rainfall Rates II. *Mon. Wea. Rev.* 111, 815–828.

Leriche, M., Pinty, J.-P., Mari, C., and Gazen, D. (2013). A cloud chemistry module for the 3-D cloud-resolving mesoscale model Meso-NH with application to idealized cases, *Geosci. Model Dev*., 6(4), 1275–298, doi:10.5194/gmd-6-1275-

2013.

Levizzani, V., and Setvák, M. (1996). Multispectral, High-Resolution Satellite Observations of Plumes on Top of Convective Storms. *J. Atmos. Sci. 53*, 361–369.

Liaskos, C. E., Allen, D. J., and Pickering, K. E. (2015). Sensitivity of tropical tropospheric composition to lightning NOx production as determined by replay simulations with GEOS-5. *J. Geophys. Res. Atmos*. 120, 8512 – 8534.

Li, Y., Pickering, K. E., Allen, D. J., Barth, M. C., Bela, M. M., Cummings, K. A., Carey, L. D., et al. (2017). Evaluation of deep convective transport in storms from different convective regimes during the DC3 field campaign using WRF-Chem with lightning data assimilation. *J. Geophys. Res. Atmos*. 122, 2017JD026461.

Li, Y., K. E. Pickering, M. C. Barth, M. M. Bela, K. A. Cummings, D. J. Allen (2018), Evaluation of parameterized transport of trace gases in simulation of DC3 storms. *J. Geophys. Res. Atmos*. (Under review).

Li, Y., K. E. Pickering, M. C. Barth, M. M. Bela, K. A. Cummings, D. J. Allen (2018), Cloud parameterized wet scavenging of soluble species and downwind ozone production of the 29 May 2012 Kingfisher supercell during DC3. (In preparation).

Livesey, N. J., Logan, J. A., Santee, M. L., Waters, J. W., Doherty, R. M., Read, W. G., Froidevaux, L., and Jiang, J. H. (2013). Interrelated variations of O_3, CO and deep convection in the tropical/subtropical upper troposphere observed by the Aura Microwave Limb Sounder (MLS) during 2004–2011. *Atmos. Chem. Phys. 13*, 579–598.

Lyons, W. A., Calby, R. H., and Keen, C. S. (1986). The Impact of Mesoscale Convective Systems on Regional Visibility and Oxidant Distributions during Persistent Elevated Pollution Episodes. *J. Climate Appl. Meteor.* 25, 1518–1531.

Marchand, M. R., and Fuelberg, H. E. (2014). Assimilation of Lightning Data Using a Nudging Method Involving Low-Level Warming. *Mon. Wea. Rev. 142*, 4850–

4871.

Martini, M., Allen, D. J., Pickering, K. E., Stenchikov, G. L., Richter, A., Hyer, E. J., and Loughner, C. P. (2011). The impact of North American anthropogenic emissions and lightning on long‐range transport of trace gases and their export from the continent during summers 2002 and 2004. *Journal of Geophysical Research: Atmospheres* 116, D07305, doi:10.1029/2010JD014305.

Mecikalski, R. M., Bain, A. L., and Carey, L. D. (2015). Radar and Lightning Observations of Deep Moist Convection across Northern Alabama during DC3: 21 May 2012. *Mon. Wea. Rev*. *143*, 2774–2794.

Mishra, A.K., and Shibata, T. (2012). Climatological aspects of seasonal variation of aerosol vertical distribution over central Indo-Gangetic belt (IGB) inferred by the space-borne lidar CALIOP. *Atmos. Environ*. 46, 365–375.

Morrison, H., Thompson, G., and Tatarskii, V. (2009). Impact of Cloud Microphysics on the Development of Trailing Stratiform Precipitation in a Simulated Squall Line: Comparison of One- and Two-Moment Schemes. *Mon. Wea. Rev*. *137*, 991–1007.

Mullendore, G. L., Durran, D. R., and Holton, J. R. (2005). Cross-tropopause tracer transport in midlatitude convection. *J. Geophys. Res*. *110*, D06113.

Mullendore, G. L., Homann, A. J., Bevers, K., and Schumacher, C. (2009). Radar reflectivity as a proxy for convective mass transport. *J. Geophys. Res. 114*, D16103.

Nault B. A., Laughner J. L., Wooldridge P. J., Crounse J. D., Dibb J., Diskin G., Peischl J., Podolske J. R., Pollack I. B., Ryerson T. B., et al. (2017). Lightning NO_x emissions: reconciling measured and modeled estimates with updated NO_x chemistry. *Geophys. Res. Lett*. 44, 9479–9488.

Neu, J. L., and Prather, M. J. (2012). Toward a more physical representation of precipitation scavenging in global chemistry models: Cloud overlap and ice physics and their impact on tropospheric ozone, *Atmos. Chem. Phys*., 12(7),

3289–3310, doi:10.5194/acp-12-3289-2012.

Ott, L. E., K. E. Pickering, G. L. Stenchikov, H. Huntrieser, and U. Schumann (2007), Effects of lightning NOX production during the 21 July European Lightning Nitrogen Oxides Project storm studied with a three-dimensional cloud-scale chemical transport model, *J. Geophys. Res.*, 112, D05307, doi:10.1029/2006JD007365.

Ott, L. E., Bacmeister, J., Pawson, S., Pickering, K., Stenchikov, G., Suarez, M., Huntrieser, H., et al. (2009). Analysis of Convective Transport and Parameter Sensitivity in a Single Column Version of the Goddard Earth Observation System, Version 5, General Circulation Model. *J. Atmos. Sci*. 66, 627–646.

Ott, L. E., Pickering, K. E., Stenchikov, G. L., Allen, D. J., DeCaria, A. J., Ridley, B., Lin, R.-F., Lang, S., and Tao, W.-K. (2010), Production of lightning NOx and its vertical distribution calculated from three-dimensional cloud-scale chemical transport model simulations, *J. Geophys. Res.*, 115, D04301, doi:10.1029/2009JD011880.

Pan, L. L., Homeyer, C. R., Honomishl, S., Ridley, B., Weisman, M., Barth, M. C., Hair, J. W., et al. (2014), Thunderstorms enhance tropospheric ozone by wrapping and shedding stratospheric air, *Geophys. Res. Lett*., 41, 7785–7790, doi:10.1002/2014GL061921.

Park S., and Allen R. J. (2015). Understanding influences of convective transport and removal processes on aerosol vertical distribution. *Geophys. Res. Lett*., 42, 10,438-10,444.

Peckham, S., Grell, G. A., McKeen, S. A., Barth, M., Pfister, G., Wiedinmyer, C., Fast, J. D., et al. (2011). WRF-Chem Version 3.3 User's Guide. NOAA Technical Memo., 98 pp.

Petersen, W. A., et al. (2005). The UAH-NSSTC/WHNT ARMOR C-Band Dual-Polarimetric Radar; A Unique Collaboration in Research, Education and Technology Transfer, *32nd Conf. on Radar Meteorology*, Preprints, Albuquerque, New Mexico, Amer. Meteor. Soc.

Pickering, K. E., Dickerson, R. R., Huffman, G. J., Boatman, J. F., and Schanot, A. (1988). Trace gas transport in the vicinity of frontal convective clouds. *J. Geophys. Res. 93*, 759–773.

Pickering, K. E., Dickerson, R. R., Luke, W. T., and Nunnermacker, L. J. (1989). Clear-sky vertical profiles of trace gases as influenced by upstream convective activity. *J. Geophys. Res. 94*, 14879–14892.

Pickering, K. E., Thompson, A. M., Dickerson, R. R., Luke, W. T., McNamara, D. P., Greenberg, J. P., and Zimmerman, P. R. (1990). Model calculations of tropospheric ozone production potential following observed convective events, *J. Geophys. Res*., 95, 14,049–14,062.

Pickering, K. E., Thompson, A. M., Scala, J. R., Tao, W.-K., Simpson, J., and Garstang, M. (1991). Photochemical ozone production in tropical squall line convection during NASA Global Tropospheric Experiment/Amazon Boundary Layer Experiment 2A. *J. Geophys. Res. 96,* 3099–3114.

Pickering, K. E., Scala, J. R., Thompson, A. M., Tao, W.-K., and Simpson, J. (1992a). A regional estimate of convective transport of CO from biomass burning. *Geophys. Res. Lett*. *19*, 289–292.

Pickering, K. E., Thompson, A. M., Scala, J. R., Tao, W.-K., Dickerson, R. R., and Simpson, J. (1992b). Free tropospheric ozone production following entrainment of urban plumes into deep convection. *J. Geophys. Res. 97,* 17985–18000.

Pickering, K. E., Thompson, A. M., Scala, J. R., Tao, W.-K., and Simpson, J. (1992c). Ozone production potential following convective redistribution of biomass burning emissions. *J Atmos Chem 14*, 297–313.

Pickering, K. E., Thompson, A. M., Tao, W.-K., and Kucsera, T. L. (1993). "Upper tropospheric ozone production following mesoscale convec¬tion during STEP/EMEX.". *J. Geophys. Res.,* 98:8737-8749: 1993.

Pickering, K. E., Thompson, A. M., Wang, Y., Tao, W.-K., McNamara, D. P., Kirchhoff, V.W.J.H., Heikes, B. G., Sachse, G. W., Bradshaw, J. D., Gregory, G.

L., et al. (1996). Convective transport of biomass burning emissions over Brazil during TRACE A. *J. Geophys. Res. 101,* 23993–24012.

Pickering, K. E., Y. Wang, W.-K. Tao, C. Price, and J.-F. Müller (1998), Vertical distributions of lightning NOX for use in regional and global chemical transport models, J. Geophys. Res., 103(D23), 31,203–31,216, doi:10.1029/98JD02651.

Pickering, K. E., Thompson, A. M., Kim, H., DeCaria, A. J., Pfister, L., Kucsera, T. L., Witte, J. C., et al. (2001), Trace gas transport and scavenging in PEM-Tropics B South Pacific Convergence Zone convection, *J. Geophys. Res*., 106, 32,591–32,607.

Pickering, K. E., Bucsela, E., Allen, D., Ring, A., Holzworth, R., and Krotkov, N. (2016). Estimates of lightning NOx production based on OMI NO2 observations over the Gulf of Mexico. *Journal of Geophysical Research: Atmospheres* 121, 8668–8691.

Prather, M. J., and Jacob, D. J. (1997). A persistent imbalance in HO_x and NO_x photochemistry of the upper troposphere driven by deep tropical convection, *Geophys. Res. Lett.*, 24(24), 3189–3192, doi:10.1029/97GL03027.

Price, C., J. Penner, and M. Prather (1997), NO_X from lightning: 2. Constraints from the global atmospheric electric circuit, *J. Geophys. Res.*,102(D5), 5,943–5,951, doi:10.1029/96JD02551.

Price, C., and Rind, D. (2012). A simple lightning parameterization for calculating global lightning distributions. *Journal of Geophysical Research: Atmospheres* 97, 9919–9933.

Qiao, F., and Liang, X.-Z. (2015). Effects of cumulus parameterizations on predictions of summer flood in the Central United States. *Clim Dyn* 45, 727–744.

Qiao, F., and Liang, X.-Z. (2016). Effects of cumulus parameterization closures on simulations of summer precipitation over the United States coastal oceans. *J. Adv. Model. Earth Syst*. 8, 764–785.

Qiao, F., and Liang, X.-Z. (2017). Effects of cumulus parameterization closures on simulations of summer precipitation over the continental United States. *Clim Dyn* 49, 225–247.

Ridley, B., et al. (2004), Florida thunderstorms: A faucet of reactive nitrogen to the upper troposphere, *J. Geophys. Res.*, 109, D17305, doi:10.1029/2004JD004769.

Sakulyanontvittaya, T., Duhl, T., Wiedinmyer, C., Helmig, D., Matsunaga, S., Potosnak, M., Milford, J., and Guenther, A. (2008). Monoterpene and Sesquiterpene Emission Estimates for the United States. *Environ. Sci. Technol. 42*, 1623–1629.

Scala, J. R., Garstang, M., Tao, W., Pickering, K. E., Thompson, A. M., Simpson, J., Kirchhoff, V.W.J.H., Browell, E. V., Sachse, G. W., Torres, A. L., et al. (1990). Cloud draft structure and trace gas transport. *J. Geophys. Res. 95*, 17015–17030.

Setvák, M., and Doswell III, C. A. (1990). The AVHRR Channel 3 Cloud Top Reflectivity of Convective Storms. *Mon. Wea. Rev. 119*, 841–847.

Siu, L. W., Bowman, K. P., and Epifanio, C. C. (2015). Convective transport of trace species observed during the Stratosphere-Troposphere Analyses of Regional Transport 2008 experiment. *J. Geophys. Res. Atmos*. *120*, 2015JD023645.

Skamarock, W. C., Powers, J. G., Barth, M., Dye, J. E., Matejka, T., Bartels, D., Baumann, K., Stith, J., Parrish, D. D., and Hubler, G. (2000). Numerical simulations of the July 10 Stratospheric-Tropospheric Experiment: Radiation, Aerosols, and Ozone/Deep Convection Experiment convective system: Kinematics and transport. *J. Geophys. Res. 105*, 19973–19990.

Skamarock, W. C., and Klemp, J. B. (2008). A Time-split Nonhydrostatic Atmospheric Model for Weather Research and Forecasting Applications. *J. Comput. Phys. 227*, 3465–3485.

Snider Jefferson R., and Huang Jun (1998). Factors influencing the retention of hydrogen peroxide and molecular oxygen in rime ice. *J. Geophys. Res. Atmos.* 103, 1405–1415.

Solomon, S., Rosenlof, K. H., Portmann, R. W., Daniel, J. S., Davis, S. M., Sanford, T. J., and Plattner, G.-K. (2010). Contributions of Stratospheric Water Vapor to Decadal Changes in the Rate of Global Warming. *Science 327*, 1219–1223.

Stenchikov, G., Dickerson, R., Pickering, K., Ellis, W., Doddridge, B., Kondragunta, S., Poulida, O., Scala, J., and Tao, W.-K. (1996). Stratosphere-troposphere exchange in a midlatitude mesoscale convective complex: 2. Numerical simulations. *J. Geophys. Res. 101*, 6837–6851.

Stuart A. L., and Jacobson M. Z. (2004). Chemical retention during dry growth riming. *J. Geophys. Res. Atmos.* 109. D07305,doi:10.1029/2003JD004197.

Sukoriansky, S., Galperin, B., and Perov, V. (2005). "Application of a New Spectral Theory of Stably Stratified Turbulence to the Atmospheric Boundary Layer over Sea Ice." *Boundary-Layer Meteorol 117*, 231–257.

Tewari, M., Chen, F., Wang, W., Dudhia, J., LeMone, M. A., Mitchell, K., Ek, M., Gayno, G., Wegiel, J., and Cuenca, R. H. (2004). Implementation and verification of the unified NOAH land surface model in the WRF model. *20th conference on weather analysis and forecasting/16th conference on numerical weather prediction*, pp. 11–15.

Thompson, A. M., Pickering, K. E., Dickerson, R. R., Ellis, W. G., Jacob, D. J., Scala, J. R., Tao, W.-K., McNamara, D. P., and Simpson, J. (1994). Convective transport over the central United States and its role in regional CO and ozone budgets. *J. Geophys. Res. 99*, 18703–18711.

Tie, X., Madronich, S., Walters, S., Zhang, R., Rasch, P., and Collins, W. (2003). Effect of clouds on photolysis and oxidants in the troposphere. *J. Geophys. Res. 108*, 4642.

Tiedtke, M. (1989). A Comprehensive Mass Flux Scheme for Cumulus Parameterization in Large-Scale Models. *Mon. Wea. Rev. 117*, 1779–1800.

Travis, K.R., Jacob, D.J., Fisher, J.A., Kim, P.S., Marais, E.A., Zhu, L., Yu, K., Miller, C.C., Yantosca, R.M., Sulprizio, M.P., et al. (2016). Why do models overestimate surface ozone in the Southeast United States? *Atmos. Chem. Phys.* 16, 13561–

13577.

von Blohn, N., Diehl, K., Mitra, S. K., and Borrmann, S. (2011). Wind tunnel experiments on the retention of trace gases during riming: nitric acid, hydrochloric acid, and hydrogen peroxide. *Atmos. Chem. Phys.* 11, 11569–11579.

Wang, Y., Tao, W.-K., Pickering, K. E., Thompson, A. M., Kain, J. S., Adler, R. F., Simpson, J., Keehn, P. R., and Lai, G. S. (1996). Mesoscale model simulations of TRACE A and preliminary regional experiment for storm-scale operational and research meteorology convective systems and associated tracer transport. *J. Geophys. Res. 101*, 24013–24027.

Wang, Y., A. W. DeSilva, G. C. Goldenbaum, and R. R. Dickerson (1998), Nitric oxide production by simulated lightning: Dependence on current, energy, and pressure, *J. Geophys. Res*., 103(D15), 19,149–19,159, doi:10.1029/98JD01356.

Wiedinmyer, C., Akagi, S. K., Yokelson, R. J., Emmons, L. K., Al-Saadi, J. A., Orlando, J. J., and Soja, A. J. (2011). The Fire INventory from NCAR (FINN): a high resolution global model to estimate the emissions from open burning. *Geosci. Model Dev. 4*, 625–641.

Wong, J., Barth, M.C., and Noone, D. (2013). Evaluating a lightning parameterization based on cloud-top height for mesoscale numerical model simulations. *Geosci. Model Dev*. 6, 429–443.

Zhang, C., Wang, Y., & Hamilton, K. (2011). Improved Representation of Boundary Layer Clouds over the Southeast Pacific in ARW-WRF Using a Modified Tiedtke Cumulus Parameterization Scheme. *Mon. Wea. Rev*. 139, 3489–3513.